（千葉大学学位申請論文）

Evaluation of the Specific Absorption Rate inside Human Bodies at VHF and UHF Bands

VHF帯及びUHF帯における生体内SAR評価に関する研究

２００５年１月

千葉大学大学院自然科学研究科
人工システム科学専攻　電子・光システム講座
河　井　　寛　記

Abstract

This dissertation deals with the evaluation of the SAR inside the human body, which is close to the portable communication devices at VHF and UHF bands.

At first, I investigate the adaptation of the evaluation method of the local average SAR calculated by the measured SAR using the thermal technique. Measurement method based on the thermal technique can evaluate a superficial SAR as well as an internal SAR distribution of an arbitrary shaped media. In addition, the calibration of this method is not due to the frequency. However, these methods are not efficient to measure the local 10 g average SAR, because the methods are not able to obtain the three-dimensional SAR distribution. Therefore, the simple evaluation method of the estimating local average SAR, which is given by the distribution on the specific planes and axes, is proposed.

Next, the investigation of the effect of inaccurate dielectric constants of the biological tissue-equivalent phantom on the local SARs at VHF and UHF bands is proposed. In the evaluation of the SAR, the dielectric constants of the phantom are very important parameters. However, it is difficult to realize perfect agreement of dielectric constants (relative permittivity, conductivity) between the phantom and the human tissue because of various factors. In the measurement, differences of dielectric constants between the two cause an error on the estimated SAR. Hence, it is necessary to understand the effects of inaccurate dielectric constants of the phantom on the local average SARs in order to realize the precision evaluation.

Finally, evaluation of the SAR inside the simple abdomen model of the pregnant women close to the portable radio terminals at VHF band. To the author's knowledge, several papers on the evaluation of the EM exposure in the fetus have been published. However, in these papers, the structure of the pregnant women is inaccurate because the MRI tomograms of the pregnant women are hard to obtain. In addition, little is known about the dielectric constants of the amniotic fluid and fetus. Therefore, this dissertation proposes the modeling of the abdomen of pregnant women. Furthermore, the SAR in the proposed abdomen model is investigated.

Contents

Chapter 1 Introduction

1.1 Background

Recent years, radiofrequency devices, which are usually placed in the vicinity of the human body, are widely used. In addition, these devices are used in various situations, e.g., talk (cellular phones and portable radio terminals), data communication (wireless LAN, personal data assistant (PDA)), cooking (induction heating cookers), detection (hand-held metal detectors (HHMD)), etc. Especially, the number of subscribers for the cellular phones, PHS and automobile telephones is now about above 84,000,000 in Japan. Therefore, the evaluation of the interaction between electromagnetic (EM) waves and the human body, which is radiated by the mobile communication devices, is indispensable. Here, the interaction suggests the effect of the human body on the characteristics of the devices and the influence of the EM waves on the human body.

The effect of the human body on the characteristics of antennas of handheld devices has been widely investigated [1]–[4]. The devices close to the human body cause the variation in the input and radiation characteristics of antenna, e.g., input impedance, radiation pattern, radiation efficiency, etc. On the other hand, the influence of the EM waves on the human body is dependent on the frequency [5]. The EM waves mainly contribute the heat effect, which is generated by the absorption of the energy, above 100 kHz. The specific absorption rate (SAR) has been usually used for the primary dosimetric parameter of the EM waves exposure in the standards [6]–[13]. Here, the local 1 g or 10 g average SAR in optional tissue is usually used, when the human body close to the portable devices.

It is therefore necessary to evaluate the interaction between the EM waves and the human body to develop the devices. The interaction is generally estimated from numerical simulations and experimental evaluations. In these evaluations, the biological tissue-equivalent phantom, which realizes human tissues, is usually used in most of the cases [14]–[38]. Literature [39] details for the types, characteristics, use of the phantoms.

Until now, various investigations have been mainly made on the interaction between the cellular phones and the human body at UHF band. For example, the standard measurement method of the SAR, which is generated by the cellular phone, in the head model has been proposed [12]. Recently, the evaluation method of the SAR inside the body are discussed when the cellular phone is mounted on the body [13]. However, these previous investigations of the SAR estimation are limited. Therefore, the application of the measurement method, which is not due to the situation (frequency, human shape, devices, etc.), is very important.

On the other hand, pregnant women and her fetus may be exposed to the EM waves radiated from these devices, e.g., portable radio terminals, induction heating cookers, handheld metal detectors, etc. It is therefore necessary to evaluate the EM exposure of the fetus inside pregnant women.

This dissertation focuses on the evaluation the SAR inside the human body at VHF and UHF bands. From now on, the cellular phones at UHF band and the portable radio terminals at VHF band are used as the mobile communication devices.

1.2 Purpose of this study

Three major purposes to this dissertation are as follows.

1) Adaptation of the evaluation method of the local average SAR calculated by the measured SAR using the thermal technique:

Measurement method based on the thermal technique can evaluate a superficial SAR as well as an internal SAR distribution of an arbitrary shaped media. In addition, the calibration of this method is not due to the frequency. However, these methods are not efficient to measure the local 10 g average SAR, because the methods are not able to obtain the three dimensional SAR distribution. Therefore, the simple evaluation method of the estimating local average SAR, which is given by the distribution on the specific planes and axes, is proposed.

2) Investigations of the effect of inaccurate dielectric constants of the biological tissue-equivalent phantom on the local SARs at VHF and UHF bands:

In the evaluation of the SAR, the dielectric constants of the phantom are very important parameters. However, it is difficult to realize perfect agreement of dielectric constants (relative permittivity, conductivity) between the phantom and the human tissue because of various factors; e.g., fabrication error, evaporation as times go by, etc. In the measurement, differences of electric constants between the two cause an error on the estimated SAR. Hence, it is necessary to understand the effects of inaccurate dielectric constants of the phantom on the local average SARs in order to realize the precision evaluation. In this dissertation, the effect of the inaccurate dielectric constants on the local SARs is investigated at VHF and UHF bands. In addition, the relationship between the inaccuracy of the relative permittivity or the conductivity and the local SARs is also cleared.

3) Evaluation of the SAR inside the simple abdomen model of the pregnant women close to the portable radio terminals at VHF band:

To the author's knowledge, several papers on the evaluation of the EM exposure in the fetus have been published. However, in these papers, the structure of the pregnant women is inaccurate because the magnetic resonance imaging (MRI) tomograms of the pregnant women are hard to obtain. In addition, little is known about the dielectric constants of the amniotic fluid and fetus. Therefore, this dissertation proposes the modeling of the abdomen of pregnant women. Furthermore, the SAR in the proposed abdomen model is investigated.

1.3 Contents

This dissertation deals with the evaluation of the SAR inside the human bodies which is close to the portable communication devices at VHF and UHF bands. Figure 1.1 shows the constructions of this dissertation.

In Chapter 2, the definition, limits of guideline, and measurement method of the SAR are introduced. This Chapter also explains the problems of the measurement method of the SAR.

In Chapter 3, the simple evaluation method of the estimating local average SAR, which is given by the distribution on the specific planes and axes using the thermal measurement, is introduced. At first, the limit of simplification is investigated when four types of antennas are close to the COST244 cubic and spherical head model at 900 MHz and 2 GHz. In addition, the effect of the distance and frequency on the average SAR using the proposed method is investigated. Moreover, we evaluate the average SAR by use of the proposed method in the realistic head model.

In Chapter 4, I investigate the effect of the inaccurate dielectric constants of the biological tissue-equivalent phantom on the local SAR in a human model when the dielectric constants are changed at 150 MHz, 900 MHz, 2 GHz, and 3 GHz. First, the peak SAR, local 1 g and 10 g average SARs in the human model are calculated when the relative permittivity or conductivity are varied from criteria to $\pm$ 20%. Next, the variation in the SAR distribution inside the model, which is caused by the inaccuracy of the relative permittivity or conductivity, is evaluated to try to find the cause of the error of the local average SARs. In addition, the relationship between the variation in the relative permittivity or conductivity and the local SARs is investigated. Moreover, the effect of the shape on the variation in the local SAR is investigated when the dielectric constants are varied at 2 GHz. Furthermore,

the corrective method of the variation in the SAR, which is caused by the inaccurate dielectric constants, is proposed.

In Chapter 5, the modeling of the abdomen of pregnant women is proposed. At first, the dielectric constants of the amniotic fluid and fetus of the rabbit are measured, because the electrical properties of mammals are almost equal to those of the human as well known. Next, a simple abdomen model of the pregnant women, which is composed by three types of tissues, based on measurements of MRI tomograms is introduced. Finally, an simple abdomen solid phantom of the pregnant women is presented.

In Chapter 6, the SAR inside the proposed simple abdomen model of the pregnant women, which is close to the portable radio terminals, is investigated at 150 MHz. At first, the SAR distribution and average value in the abdomen model is calculated. Next, the thermal error in the abdomen model and the exposure condition of the measurement is solved by the thermal analysis. Moreover, the temperature distribution in the abdomen phantom is measured and compared with the calculated result.

Finally conclusions of this dissertation are presented in Chapter 7.

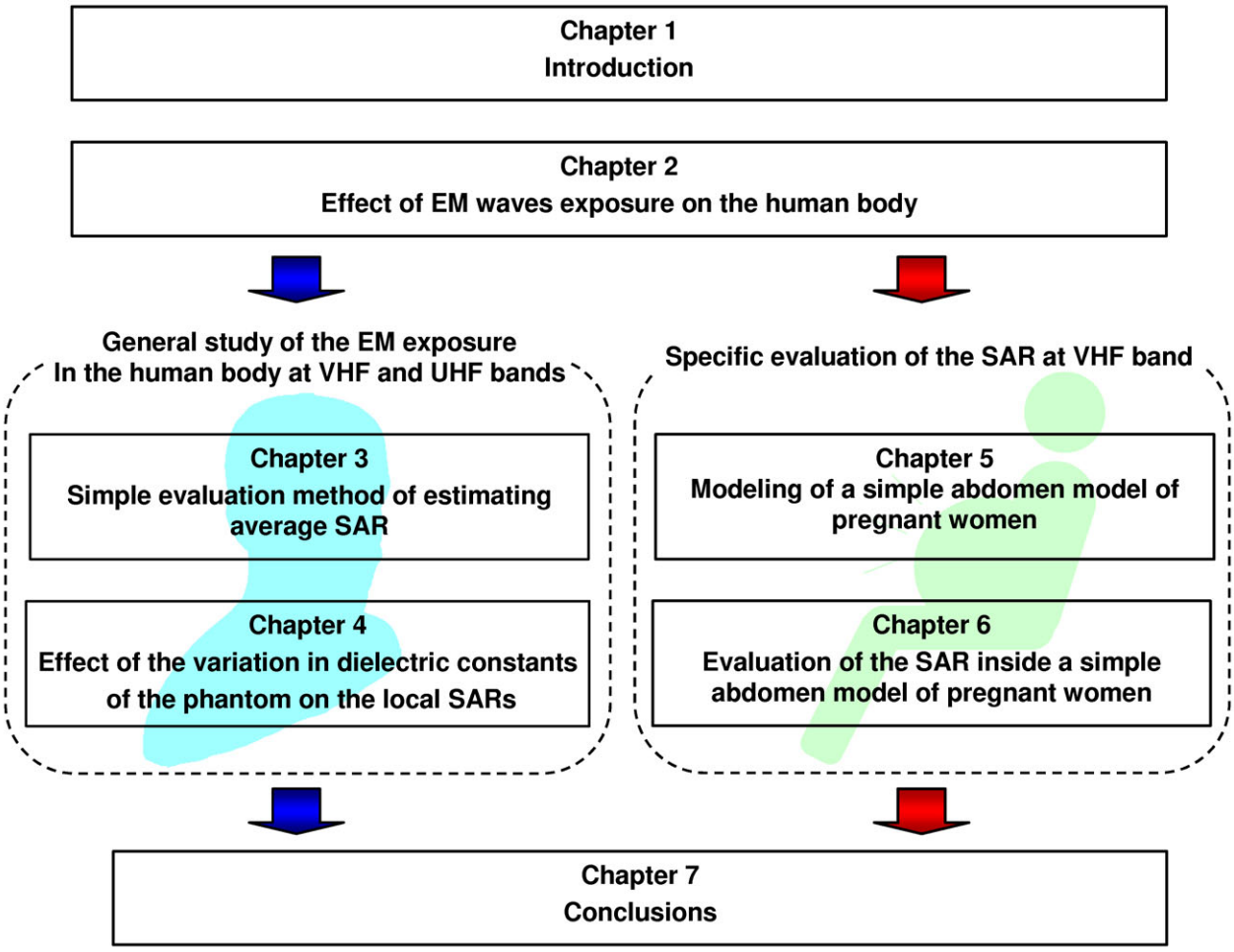

Fig. 1.1 Construction of this dissertation.

Chapter 2 Effect of EM waves exposure on the human body

2.1 Introduction

The effect of the EM waves, which is radiated from radio frequency (RF) devices, on the human body is dependent on the frequency as well known [5]. The effect is divided broadly into two categories which are the stimulus or heat effect. Figure 2.1 describes the threshold of the effect of the E-field on the human body. As shown in Fig. 2.1, the threshold of the stimulus effect is lower than that of the heat effect below 10 kHz because the increase in the capacitance of the cell membrane is proportional to the increase in the frequency above 1 kHz. Therefore, generation of the stimulus effect by the E-field is easier than that of the heat one below 10 kHz. Here, the stimulus effect, which is caused by the induced current, mainly generates around the skin. On the other hand, the threshold of the heat effect is larger than that of the stimulus one above 100 kHz. Therefore, generation of the heat effect by the E-field is easier than that of the stimulus one above 100 kHz. In addition, the boundary of the effect is at 10 to 100 kHz.

In this dissertation, I only evaluate the heat effect inside the human body because the frequency of the portable devices is at VHF (30–300 MHz) and UHF (300 MHz to 3 GHz) bands. The SAR has been usually used for the primary dosimetric parameter of the heat effect, which is caused by the EM waves exposure, in the standards [6]–[13].

This Chapter presents the limits and measurement method of the SAR. First, in Section

2.2, the limits of the SAR are introduced. Moreover, Section 2.3 deals the measurement methods of the SAR. In addition, the merits and demerits of the measurement methods are also proposed.

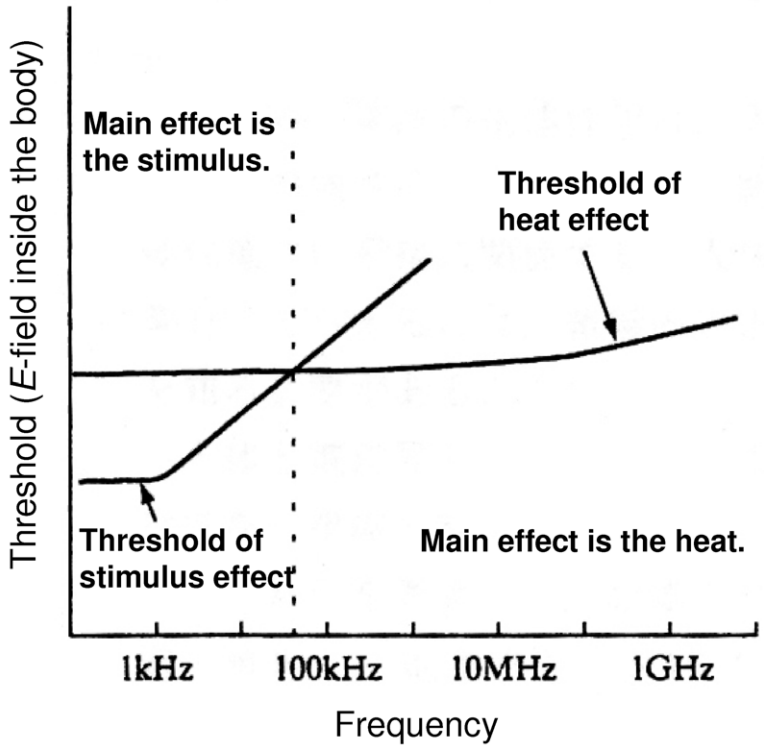

Fig. 2.1 Threshold of the effect of the E-field on the human body [5].

2.2 Limits of the SAR

The current basic safety limits applicable to the wireless device are defined in terms of the SAR. However, the average volume of the SAR is due to the Country. In United States, the 1 g average SAR is used as the safety limit of the EM exposure of the cellular phones [8]. On the other hand, EU and Japan apply the 10 g average SAR [7], [11]. In the evaluation of the SAR inside the human head close to the cellar phone, almost same measurement method using the E-field probe and the liquid phantom is adopted [9], [12].

For example, in the guideline of Japan [11], there exist three different limits defined by; 1) a whole-body average SAR; 2) a local peak SAR; and 3) a contact current at 100 kHz to 100 MHz. 1) and 2) must be averaged over a defined period of time (six minutes). In wireless devices above 300 MHz, the absorption affects only part of the body close to the device. Hence, the most critical value is the local peak SAR limit. Table 2.1 describes the guidelines values of a voluntary system of local SAR in Japan [11]. Here, the control environment means the occupational surrounding. In this dissertation, the occupational limit (10 W/kg, 10 g average) is used to the pregnant women close to the VHF band portable radio terminals. On the other hand, the nonoccupational limit (2 W/kg, 10 g average) is applied to the fetus because the noncontrol limit is severer than the control limit.

Table 2.1 Guidelines values of a voluntary system of local SAR in Japan [11]

Type of limits	Control environment	Uncontrol environment
Whole-body average SAR	0.4 W/kg	0.08 W/kg
Local SAR	In the optional tissue of 10 g 10 W/kg 20 W/kg (arms and legs)	In the optional tissue of 10 g 2 W/kg 4 W/kg (arms and legs)
Contact current	Nonprotection of the contact hazard 100 mA at 100 kHz to 100 MHz	Protection of the contact hazard 45 mA at 100 kHz to 100 MHz

2.3 Evaluation method of the SAR

The experimental evaluation methods of the SAR are divided broadly into two categories, which are based on the E-field [25] or thermal measurement [26]–[30]. The evaluation method of the SAR based on the E-field measurement is called the E-field probe method. In this method, the E-field probe and the liquid phantom is usually used. This method is generally applied the standard measurement [9], [12]. The other evaluation method, which uses the E-field probe and the solid (dry) phantom [32], is also proposed [40]. On the other hand, the evaluation method of the SAR based on the thermal measurement, which uses an infrared camera and the solid (gel) phantoms, is called the thermograhphic method. The other evaluation method, which uses the optical fiber probe and the solid phantom, is also proposed [30]

Table 2.2 shows the comparison of characteristics of the two measurement methods. As shown in Table 2.2, each of these methods has its merits and demerits. Therefore, the use of these method is due to the aim, devices, human models, etc.

This Section introduces the E-field probe method and the thermographic method.

Table 2.2 Comparison of the SAR measurement methods

Method	E-field probe method	Thermographic method
Phantom	Liquid	Solid (gel)
Merits	1. Direct measurement of SAR available 2. Actual devices can be evaluated	1. Surface SAR measurable 2. Multi-layered models feasible 3. Calibration is not due to frequency
Demerits	1. Surface SAR not measurable 2. Difficult to measure SAR for complicated objects 3. Calibration is due to frequency	1. Actual devices can not be evaluated because high power is needed 2. Difficult to evaluate average SAR

2.3.1 E-field probe method

Definition of the SAR by E-field measurement

The E-field probe method is generally used for the SAR estimation in the standards [6]–[12]. This method uses an E-field probe and a liquid phantom [24], [25]. In this method, a package of the measurement system is usually used [41]. The SAR inside the phantom by this method is given by

$$\mathrm{SAR} = \frac{\sigma}{\rho} E^2 \quad [\mathrm{W/kg}] \tag{2.1}$$

where E is the amplitude of the electric field (rms value) [V/m], σ is the conductivity of the tissue [S/m], and ρ is the density of the tissue [kg/m^3].

Measurement system

In this method, the SAR is evaluated by the measurement of the E-field distribution inside the liquid phantom, which is composed by a lossy liquid and a shell, using the isotropic E-field probe. Figure 2.2 shows the measurement system of the E-field probe method. Conditions of parts are as follows:

1) Phantom shell: The shell realizes the right or left half of the human head. The conditions of the shell are as follows: $\varepsilon_r \leq 5$, $\tan\delta \leq 0.05$, thickness = 2 mm. This phantom shell for the standard measurement using the cellular phones, which realizes the 90% of average measurements of adult men in USA, which is called the SAM (specific anthropomorphic mannequin) phantom. The phantom shell is generally used in the worldwide (e.g., [12]). Recently, standardization of a flat abdomen phantom is discussing [13].

2) Liquid phantom: The brain- or muscle-equivalent liquid is usually used. The ingredients of the liquid phantoms are depend on the frequency. The agreement between the phantom and the reference value is less than 5% is necessary.

3) Dosimetric E-field probe: Figure 2.3 shows the structure of the E-field probe. The probe is composed by a three axes isotropic minute electrical dipole antenna (length $\leq$ 5 mm), a detective circuit, and a transmission circuit. The application frequency of the probe is 10 MHz to 3 GHz. In addition, the dynamic range of the probe is 5 mW/kg to 100 W/kg ($\pm$0.2 dB). Moreover, the probe is not due to the direction of the incident wave and polarization. In literature [12], a requisite performances of the E-field probe are as follows: the minimum limit of the detective SAR $\leq$ 0.02 W/kg, the maximum limit of the detective SAR $\geq$ 100 W/kg, the linearity of the SAR is 0.02 to 100 W/kg ($\leq \pm$0.5 dB), the isotropy $\leq \pm$1 dB, the sensitivity, the linearity, and the isotropy is evaluated in the tissue-equivalent liquid phantom at measurement frequency, the element length of the minute dipole antenna of the E-field sensor $\leq$ 5 mm, the measurements of the protecting cover of the censer $\leq$ 8 mm.

4) Field probe positioner (Robot): In order to evaluate the SAR, it is indispensable to realize that the positioning accuracy of the robot is almost equal to 0.02 mm, because the E-field around the surface is evaluated by the extrapolation.

5) Device holder: The material of the holder does not affects the radiated EM field. In addition, the holder realizes the precision positioning. The requisite performances of the holder are as follows: the error of the inclination $\leq \pm 1^{\circ}$, $\tan\delta \leq 0.05$, $\varepsilon_r \leq 5$.

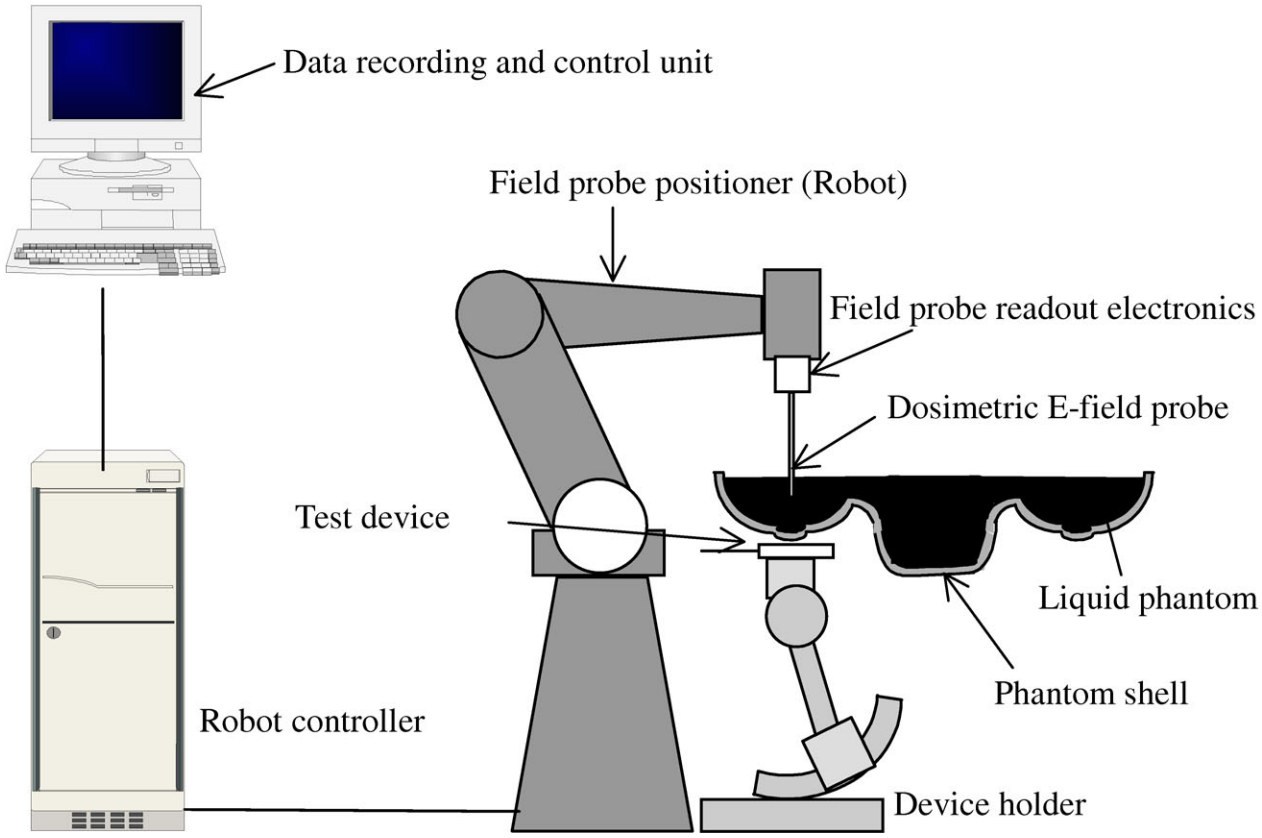

Fig. 2.2 SAR measurement system by the E-field probe method.

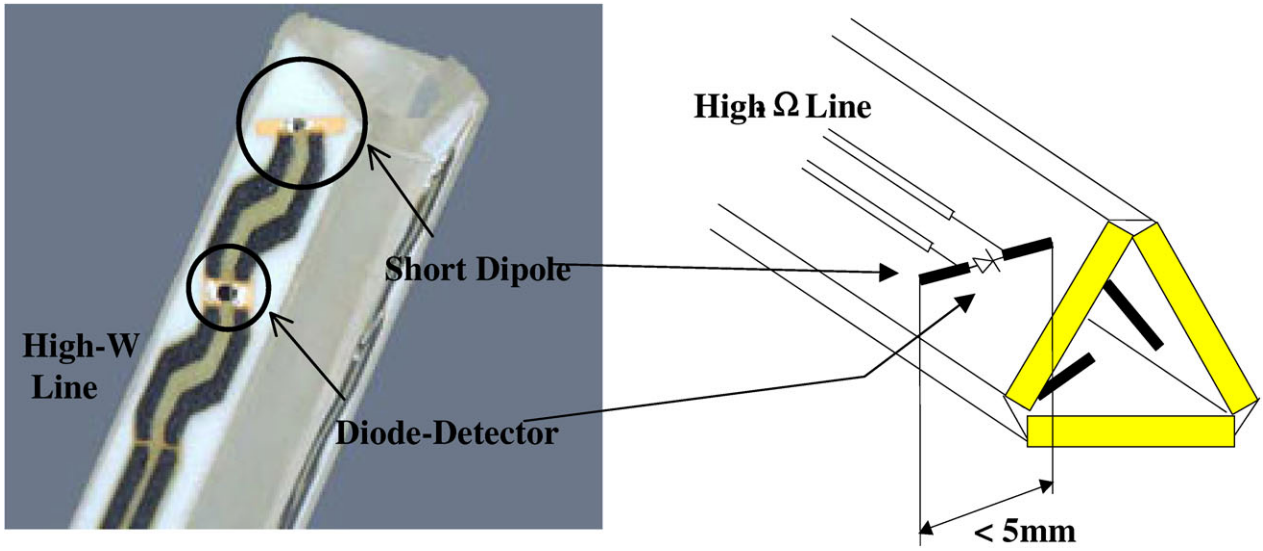

Fig. 2.3 E-field probe.

Flowchart of the E-field probe method

Fig. 2.4 shows the flowchart of the evaluation of the SAR inside the head phantom, which is close to cellular phones, by the E-field probe method [10], [12].

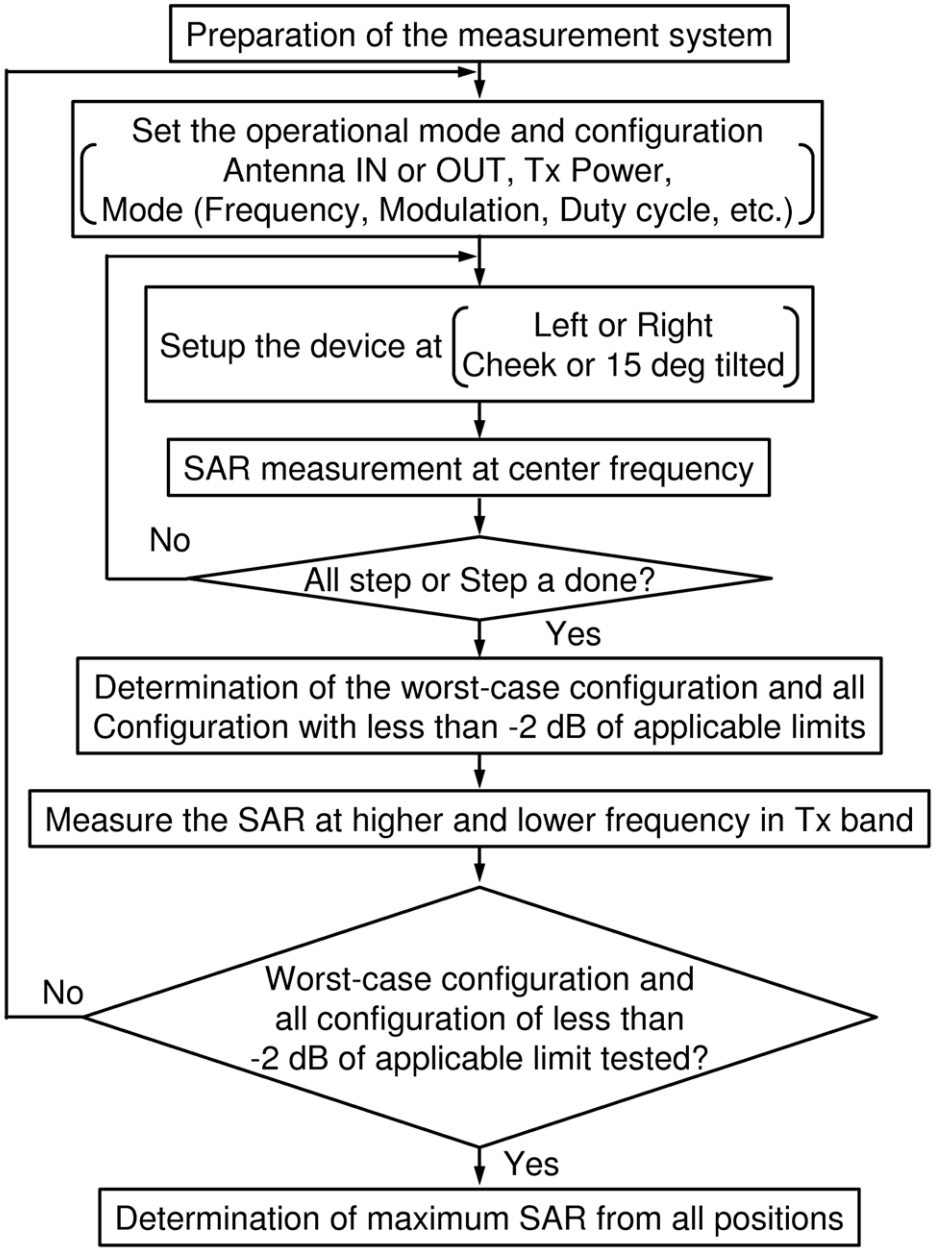

Fig. 2.4 Flowchart of the SAR measurement by the E-field probe method.

Error and the calibration method of E-field probe method

1) Calibration of the SAR: It is necessary to calibrate the E-field probe to realize the SAR estimation. The E-field probe is generally calibrated by: 1) the normal E-field in the free space; 2) the normal E-field in the liquid; 3) a waveguide; 4) a temperature probe. 3) is usually used. In addition, the calibration of the whole system is indispensable. Here, the system is normally calibrated by use of a known SAR close to a half-wave dipole antenna.

2) Measurement error: The measurement error is caused by various factors: e.g., the characteristics of liquid (the relative permittivity, the conductivity, and the temperature), the error of the system, etc. The error by the characteristics of the liquid is able to reduced of a few percent by the precision measurement of the dielectric constants of the liquid. However, the dielectric constants of the liquid is varied by the evaporation and the precipitation (sugar, salt) in the long time measurement. Therefore, it is necessary to periodically measure the dielectric constants of the liquid. The effect of the variation in the dielectric constants on the SAR is shown in Chap 4. In addition, the variation in the temperature of the liquid cases an error. Hence, it is indispensable to control the temperature at 18 °C to 25 °C ($\leq$ 2 °C). The inaccuracy of this method are as follows: the E-field probe (calibration, isotropy, sensitivity), the parameters of the phantom (dielectric constants, temperature) and the shell, the positioning of the holder, the management of the data (extrapolation, integral calculus, averaging), etc. Therefore, the maximum error in the measurement system is almost equal to 30% [10].

2.3.2 Thermographic method

The thermographic method is one of the evaluation methods for the SAR based on the thermal measurement [26]–[28]. The EM waves insde body generates the heat effect above 100 kHz as shown in Section 2.1. Here, if the heat distribution in the tissue is negligibly small, the SAR is proportional to the temperature rise inside the tissue. Therefore, in the thermographic method, the SAR is given by the temperature measurement inside the phantom. This method can measure the SAR distribution on the surface of the phantom. In addition, this method can also measure the complicating shape, because the infrared camera realize the noncontact measurement.

Definition of the SAR by thermal measurement

In the thermographic method, the SAR is given by thermal measurement using an infrared camera and a tissue-equivalent solid phantom. First, the phantom is exposed to the EM waves radiated from the antenna. Then, the temperature-rise in the phantom is observed by use of the infrared camera after the exposure. Here, the exposure time must be as short as possible within a range that makes the heat distribution observable, to minimize the heat diffusion. If the heat diffusion and exposure time are negligibly small, the SAR at an arbitrary point is given directly by

$$\mathrm{SAR} = c\frac{\Delta T}{\Delta t} \qquad [\mathrm{W/kg}] \tag{2.2}$$

where c is specific heat of the phantom [J/kg $\cdot$ K], Δt is the exposure time [s], and ΔT is the temperature rise at the point [K].

In the thermographic method, it is necessary to generate the temperature-rise inside the phantom by the short time exposure. Therefore, the several tens of watts output power of the antenna, which is larger than that of real devices, is indispensable. The SAR measurement

using the thermographic method is generally evaluated in a radio anechoic chamber. Figure 2.5 shows the measurement system of the thermographic method.

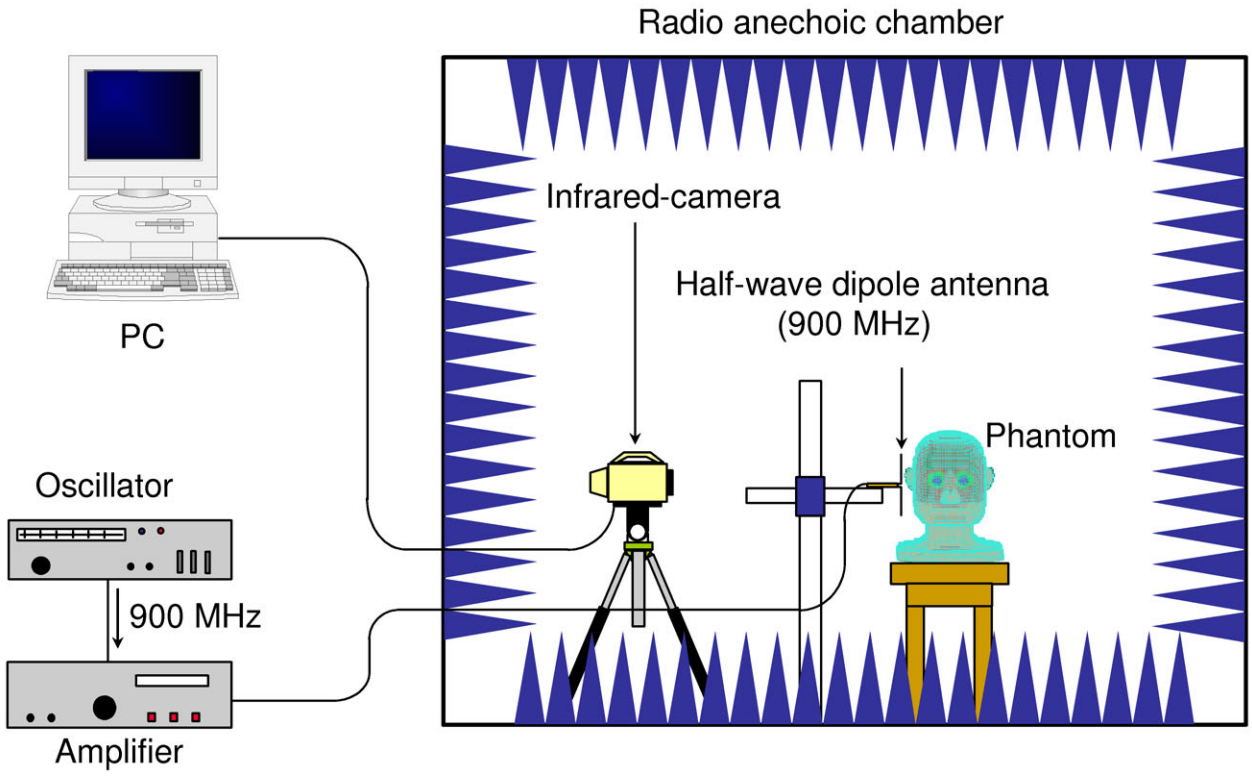

Fig. 2.5 SAR measurement system by the thermographic method.

Measurement system

1) Antenna: In the thermographic method, it is necessary to generate the sufficient temperature rise (above several K) inside the phantom to evaluate the precision SAR distribution. Therefore, the necessity of the exposure condition is due to the thermal characteristics of the phantom. For example, 100 W output of the antenna is necessary to evaluate the SAR using the dry phantom. On the other hand, the maximum output power of real cellular phone is 300 mW. In addition, the maximum output of the portable radio terminals at 150 MHz is 5 W. Therefore, it is difficult to evaluate the SAR by use of the thermographic method close to the real devices. In this method, the requirement of the antenna is as follows: the structure and electrical characteristics is almost equal to the real devices, the endurance of the output power is above 100 W, the heat generation of the antenna does not cause the variation in the temperature distribution.

2) Solid phantom: The solid or gel phantom, which is realized the structure and shape of the human body, is generally used. It is desirable to be the divisible phantom to measure the internal SAR distribution. In addition, the low thermal conductivity is also desirable.

3) Infrared camera: The infrared camera uses the temperature measurement. The measurement of the emittance of the phantom is necessary to evaluate the temperature in the phantom using the infrared camera.

Flowchart of the thermographic method

Figure 2.6 shows the flowchart of the thermographic method.

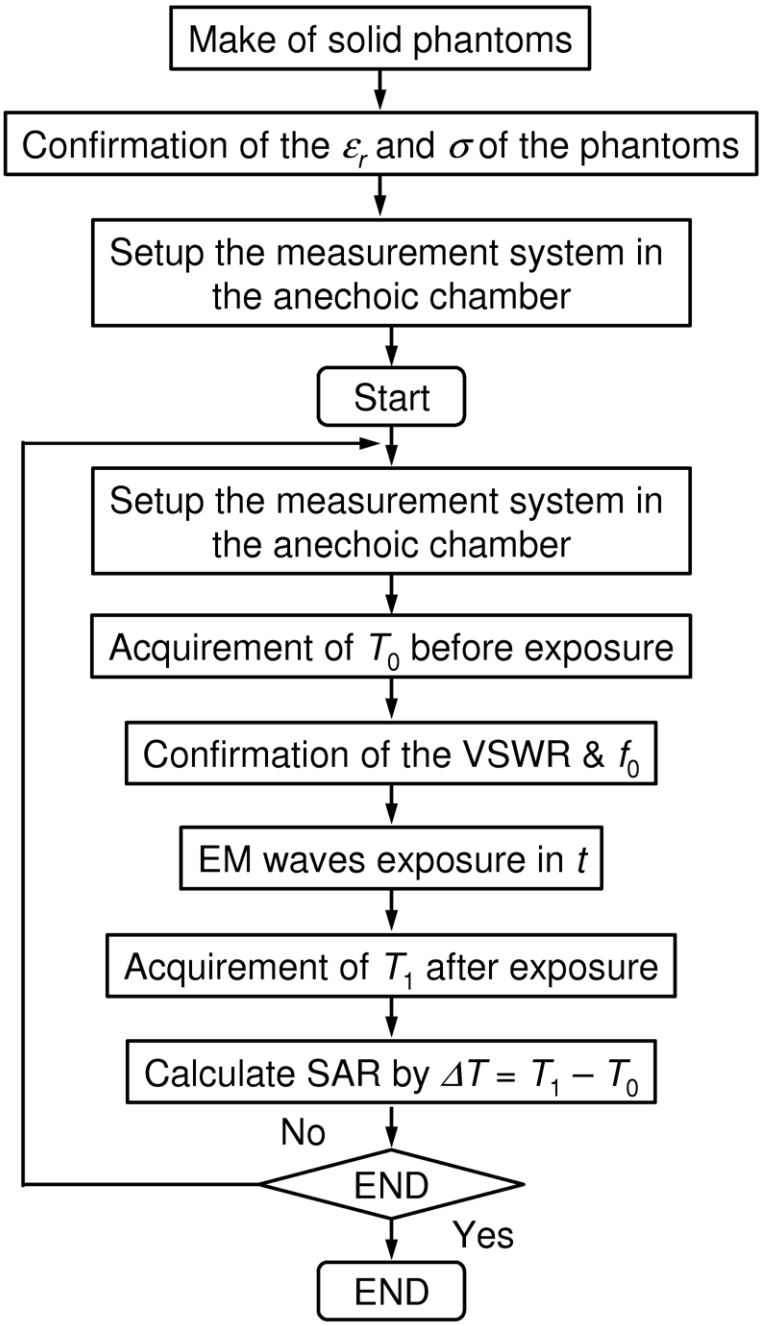

Fig. 2.6 Flowchart of the SAR measurement by the thermographic method.

Measurement error of the thermographic method

1) Error of the characteristics of the antenna: The difference of the structure between the measured antenna and the real devices causes the variation in the near-field distribution of the EM field around the phantom. On the other hand, the evaluation of the SAR using the mismatch antenna is difficult.

2) Thermal error: The thermal error is mainly caused by the thermal conduction inside the phantom and the heat transfer on the phantom surface [37], [36]. The variation in the thermal conduction is able to reduce of the several percents by use of the phantom which has high specific heat and low thermal conductivity. On the other hand, in order to reduce the heat transfer, the measurement room, which keeps the constant temperature, is important. In addition, in order to reduce these thermal errors, the short time exposure is important. However, the short time exposure is difficult at VHF band [35], [36]. In these cases, the thermal analysis inside the phantom is indispensable. The thermal analysis will be examined in Chapter 6.

3) Error by the emittance: In thermometry that uses infrared camera, the emittance of the phantom is an important parameter. The emittance of a surface is defined as a ratio of the radiation flux per unit area of the emitter to that of a blackbody radiator at the same temperature and under the same conditions (Expression 2.3). Determination of surface temperature as well as temperature variations over the surface depend directly upon the surface emittance [42].

$$U_b : U_m = 1 : X \tag{2.3}$$

Where U_b and U_m are the radiation flux per unit area of the emitter to that of a perfect blackbody radiator and object at the same temperature, respectively. In addition, X

means the emittance of the object. For instance, the temperature of the phantom is lower than the true value when the emittance setting of infrared camera is higher than the true. Therefore, the evaluation of the emittance is necessary.

2.4 Conclusion

This Chapter presented the limits and measurement method of the SAR. First, In Section 2.2, the limits of the SAR are introduced. Moreover, in Section 2.3 dealt the measurement methods of the SAR. In addition, the merits and demerits of the methods were also proposed. As a demerits of the thermal technique, the difficulty of the evaluation of the local average SARs were suggested. I will discuss a solution of this problem in the next Chapter. Furthermore, the measurement error, which is caused by the inaccurate dielectric constants of the phantom, will be examined in Chapter 4.

Chapter 3 Simple evaluation method of estimating average SAR

3.1 Introduction

The local 1 g or 10 g average SAR has been used for the primary dosimetric parameter of the EM waves' exposure [6]–[12]. These SARs are generally estimated from numerical simulation [14], [24] and experimental evaluation [25]–[30]. The experimental evaluation is based on the E-field [25] and thermal measurement [26]–[30]. The thermal technique used the solid phantoms and an infrared camera (thermografic method [26], [28]) or an optical-fiber thermometer [29], [30]. These methods can measure a superficial SAR, as well as an internal SAR distribution of an arbitrary shaped media. However, these methods are not efficient to measure the local 10 g average SAR because the methods are not able to obtain the three-dimensional SAR distribution. Therefore, a simple and precision evaluation method of estimating local average SAR, which is based on the distribution of the planes and axes, is needed.

The aim of this Chapter is to realize the estimation of the local average SAR calculated by the measured SAR using the thermal technique and to investigate the limit of the simplification of the measurement point for averaging.

In this Chapter, the simple evaluation method of the estimating local average SAR, which is given by the distribution on the specific planes and axes, is introduced. First, in Sections 3.2 and 3.3, the limit of simplification is investigated when four types of antennas, which are a half-wave dipole antenna, a monopole antenna mounted on a metal box, a planar

inverted F antenna (PIFA), and a half-wave dipole antenna with a planar reflector, are close to the COST244 cubic and spherical head model at 900 MHz and 2 GHz. In Section 3.4, the effect of the distance and frequency on the average SAR using the proposed method is investigated. In addition, I evaluate the average SAR by use of the proposed method in the realistic head model.

In this Chapter, the criteria of precision evaluation, which is agreement between the average SAR by use of the proposed method and that using the three dimensional SAR distribution, is within $\pm$ 10%. In addition, the average SAR in the heterogeneous model is not investigated because the standard measurement [12] uses the homogeneous phantom.

3.2 Models and method

3.2.1 Models

The SAR distribution in the head model is strongly due to the configuration of the devices as well known. However, the numerical simulation cannot take all the cases of the complex environment of mobile equipment in use into account. Therefore, four types of antennas are used for calculation in order to investigate the effect of the SAR distribution on the calculated average SAR by proposed method.

Figures 3.1 (a) to (d) shows the configurations of four types of antennas, which are replaced as the cellular phones. The first is a half-wave dipole antenna, as shown in Fig. 3.1 (a). The second is a monopole antenna mounted on a metal box [24], as given by Fig. 3.1 (b). The third is a PIFA, as shown in Fig. 3.1 (c). The parameters of the PIFA at 900 MHz are $L = 60$ mm and $W = 20$ mm, and those at 2 GHz are $L = 20$ mm and $W = 10$ mm. The fourth is a half-wave dipole antenna with a planar reflector, as given by Fig. 3.1 (d). This antenna can divide the SAR distribution when the axial length of the refractor is adjusted [31].

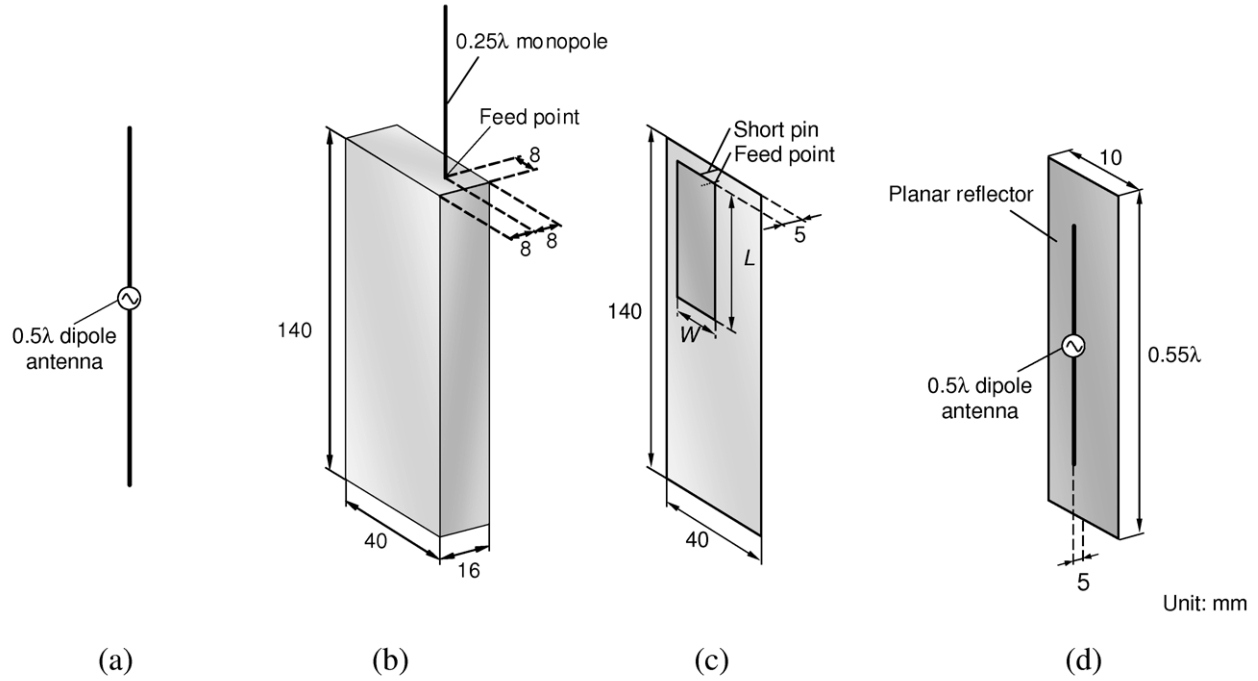

Fig. 3.1 Configurations of antennas. (a) Half-wave dipole antenna. (b) Quarter-wave monopole mounted on a metal box. (c) PIFA ($L = 60$ mm, $W = 20$ mm at 900 MHz, $L = 24$ mm, $W = 10$ mm at 2 GHz). (d) Half-wave dipole antenna with a planar reflector.

Figures 3.2 (a) and (b) show the basic model for calculations. Figure 3.2 (a) represents the half-wave dipole antenna and a COST244 cubic head model [38]. The dimension of the cube is 200 mm in a side. On the other hand, Fig. 3.2 (b) describes the antenna and a COST244 spherical model. The radius of the sphere is 100 mm. The characteristics of the head models are as follows. The electrical properties at 900 MHz are the relative permittivity $\varepsilon_r = 41.5$, the conductivity $\sigma = 0.97$ S/m, and those at 2 GHz are $\varepsilon_r = 40.0$, $\sigma = 1.40$ S/m, and the density $\rho = 1{,}000$ kg/m^3 [12]. In addition, the distance between the feed point of the antenna and the phantom surface is d [mm]. In this Chapter, the local 10 g average SAR in the cubic model is calculated from the SAR in the cube with a volume of 21.56 $\times$ 21.56 $\times$ 21.56 mm^3 (10.02 g).

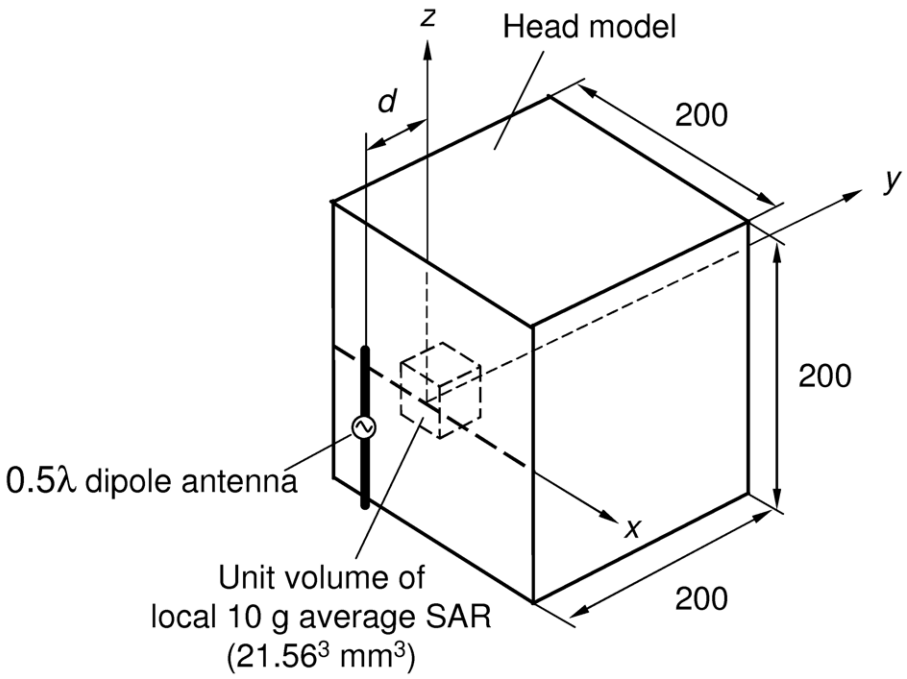

(a) Cubic model

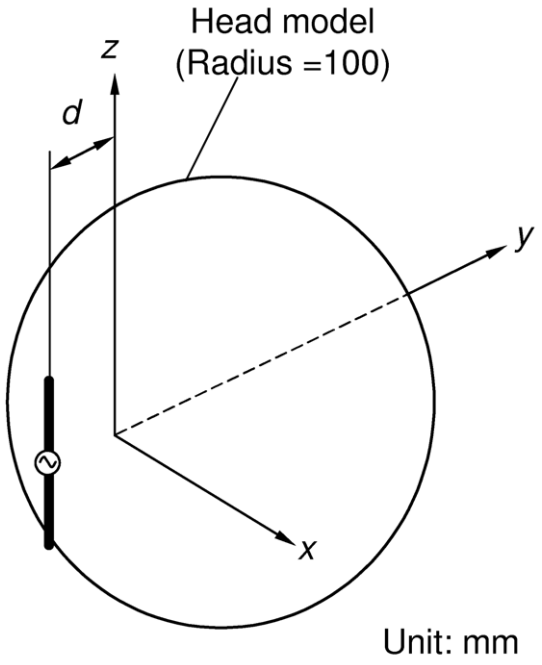

(b) Spherical model

Fig. 3.2 Models for calculation.

3.2.2 Simple evaluation method

Figure 3.3 describes the unit volume of the local average SAR in the $x-y$ plane ($y-z$ plane) of the spherical model. In this Chapter, x and z axes, which are along the surface of the spherical model, are used, as shown in Fig. 3.3, when the average SAR in the spherical model is evaluated. Here, the origin is the point of the peak SAR on the phantom surface.

The local average SAR is generally calculated from three dimensional SAR distribution of in the unit volume, as shown in Figs. 3.2 (a) and 3.3. In this Chapter, three-dimensional distribution in the average area is replaced as follows: the SAR distribution on two planes [see Fig. 3.4 (a)]; the specific plane [see Fig. 3.4 (b)]; two or three axes [see Fig. 3.4 (c)]; the specific axis [see Fig. 3.4 (d)]. Here, in Figs. 3.4 (a) and (b), the thermographtic method is assumed. On the other hand, in Figs. 3.4 (c) and (d), the optical-fiber probe measurement is assumed. Here, for example, the calculation method of the average SAR using the SAR distribution on the two planes measured by the thermographic method is as follows:

1) measurement of the SAR distribution in the $x-z$ plane and $y-z$ plane ($x-y$ plane);

2) search of the peak point of the SAR (determination of the origin and average area);

3) calculation of the SAR_{x-z} and SAR_{y};

4) calculation of the average SAR in the unit volume that is equal to SAR_{x-z} times SAR_{y}, which is normalized to the peak SAR

where SAR_{x-z} is the average SAR of the $x-z$ plane [W/kg], SAR_{y} is the average SAR of the y axis on the $y-z$ plane ($x-y$ plane) [W/kg]. Similarly, the average SAR using the data on the axes is calculated by the measured SAR by the optical fiber probe measurement.

Moreover, in this Chapter, the calculated local average SAR using the SAR distribution on the $x-z$ plane or the $x-z$ axes, and that using the distribution on the x or z axis is

omitted because the difference between these averaged values and the reference is larger than 10% to 210% in each model. Furthermore, the results of 1 g average SAR are also omitted, because the error of 1 g average SAR is less than that of 10 g.

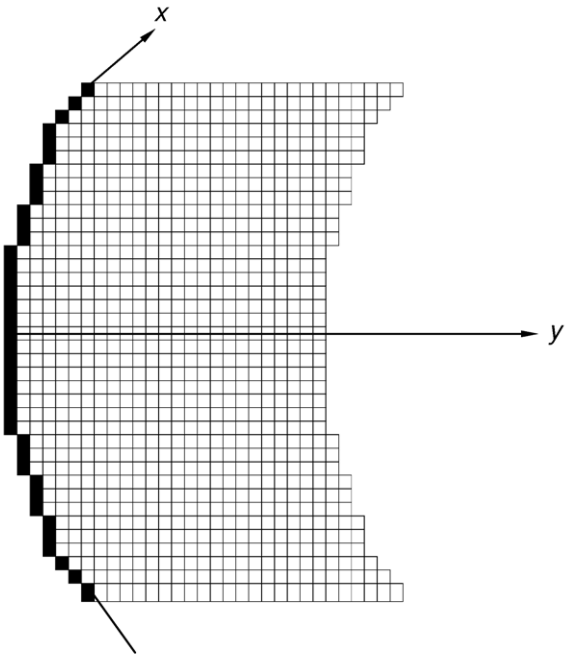

Fig. 3.3 Calculation area of local average SAR in the spherical model ($x-y$ plane or $y-z$ plane).

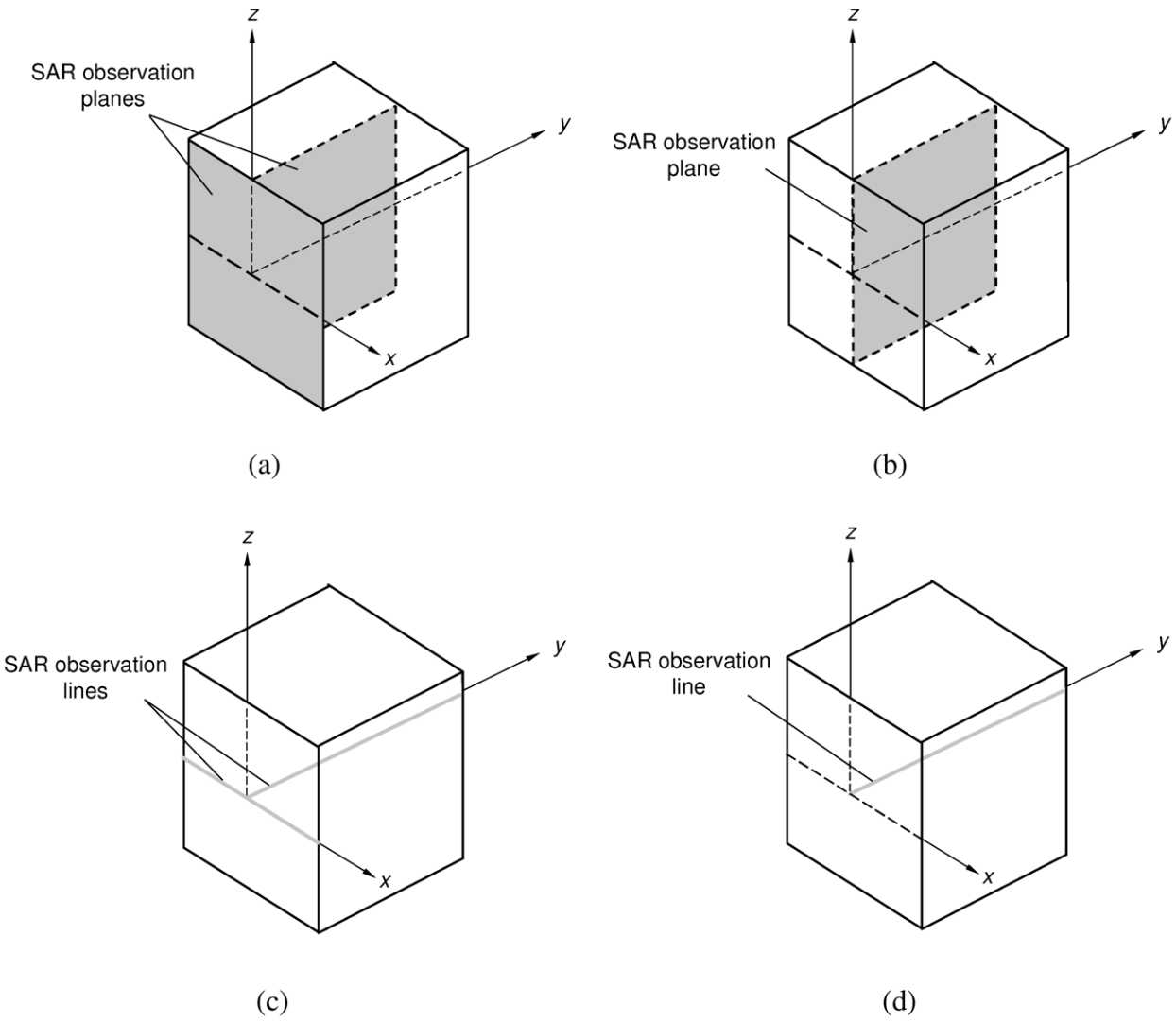

Fig. 3.4 SAR observation planes or axes in the unit volume of the average SAR. (a) Two plane. (b) Specific plane. (c) Axes. (d) Specific axis.

3.2.3 Numerical technique

The finite-difference time-domain (FDTD) [43], [44] software (SEMCAD ver. 1.6, by Schmid & Partner Engineering AG, Zürich, Swizerland [45]) is used for the SAR calculating in the head models. The parameters of the FDTD calculation employed in this Chapter are as follows: the averaging area of the local 10 g average SAR ($32 \times 25 \times 32$ mm^3) were computed with every 0.77 mm step, the cell size of other region is 1 mm, the absorbing boundary condition is the perfectly matched layer (PML) (eight layers), and the calculation time is ten periods at each frequency to get converged results.

Table 3.1 describes the local 10 g average SAR in the head models at each frequency when the antennas are placed on $d = 15$ mm. In this Chapter, the SAR is normalized to 1 W output. Here, the local 10 g average SAR is averaged on all SAR data (28^3 points) in the unit volume as shown in Figs. 3.2 (a) and 3.3. From now on, these SARs are used as the reference value, to confirm the validity of proposed method.

Table 3.1 Reference values of the local 10 g average SAR [W/kg] in the canonical head models (d =15 mm)

Antenna type		900 MHz	2 GHz
Dipole	cube	6.76	11.2
	sphere	6.31	10.3
Monopole	cube	3.93	7.73
	sphere	2.57	6.51
PIFA	cube	4.16	1.76
	sphere	1.42	1.70
Dipole with reflector	cube	1.62	1.24
	sphere	1.21	2.22

3.3 Results and discussions

3.3.1 Results of cubic model

Figures 3.5 (a)–(d) illustrate the SAR distributions on the $x - z$ plane ($y = 0$) of the cubic phantom at 900 MHz. Here, each distribution is normalized to its maximum value for each respective model. The SAR distribution in the average area using the 0.47 λ dipole antenna resembles that of the cylindrical wave, as shown in Fig. 3.5 (a). Figure 3.5 (b) shows the distribution, which has two peak points, using the monopole antenna. From Fig. 3.5 (c), the distribution in the average area using the PIFA is quite similar to that using the plane wave. Finally, in the case of the dipole antenna with the planar reflector, the peak SAR on the phantom surface is divided into three points as shown in Fig 3.5 (d). It should be noted that the angle of incidence wave in Fig. 3.5 (d) is different that in Figs. 3.5 (a)–(c).

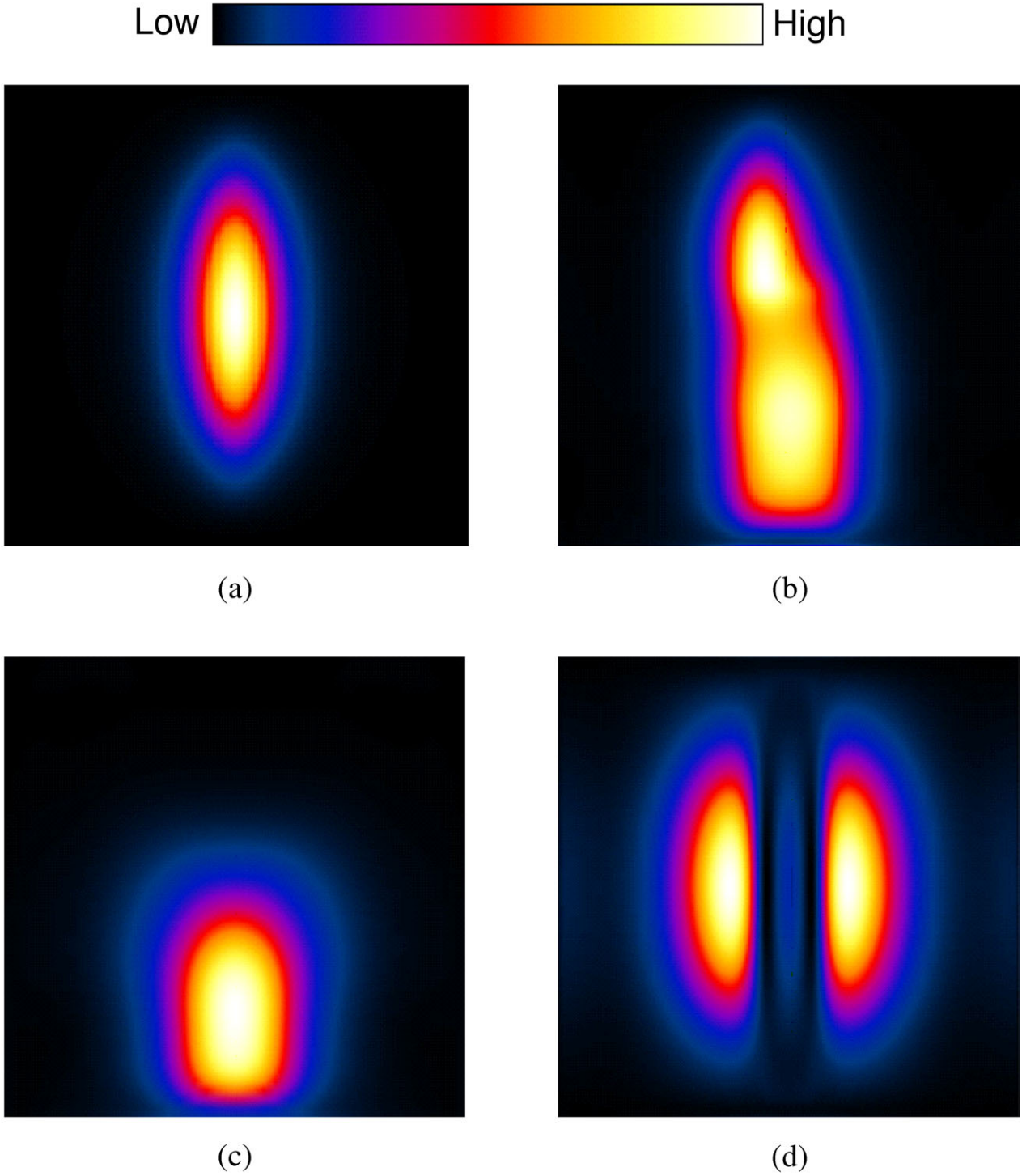

Fig. 3.5 SAR distributions on the $x-z$ plane ($y=0$) at 900 MHz. (a) Half-wave dipole antenna. (b) Quarter-wave monopole mounted on a metal box. (c) PIFA. (d) Half-wave dipole antenna with a planar reflector.

Figures 3.6 (a) and (b) show the calculated results of the local 10 g average SAR in the cubic model using the SAR distribution on the planes at 900 MHz and 2 GHz. From now on, the SARs are normalized to the reference value, as given by Table 3.1.

From Fig. 3.6 (a), the difference of the 10 g average SAR between the calculated by proposed method and the reference is within –4% to +6%, except the result by use of the SAR on the $y-z$ plane because the variation in the SAR of the x direction is larger than that in the another axis. In addition, the average SAR on the $x-y$ plane is in very good agreement with the reference because the SAR on the z direction is hardly due to the x and y. On the other hand, as shown in Fig. 3.6 (b), the difference between the two methods is within –8% to +8% except the result by use of the data on the $y-z$ plane and the $y-z$ plane times x axis at 2 GHz.

From Figs. 3.6 (a) and (b), the difference at 2 GHz is larger than that at 900 MHz because the SAR distribution on the surface is corrected the point of the peak SAR, which is caused by the shortening of the antenna element. These differences are mainly caused by the variation in the attenuation of the SAR of the y direction when x is changed because the angle of incident wave is due to x. Consequently, the average SAR in the cubic model can evaluate using the distribution on the $x-y$ plane or two planes within $\pm$ 10% of the deviation at 900 MHz and 2 GHz.

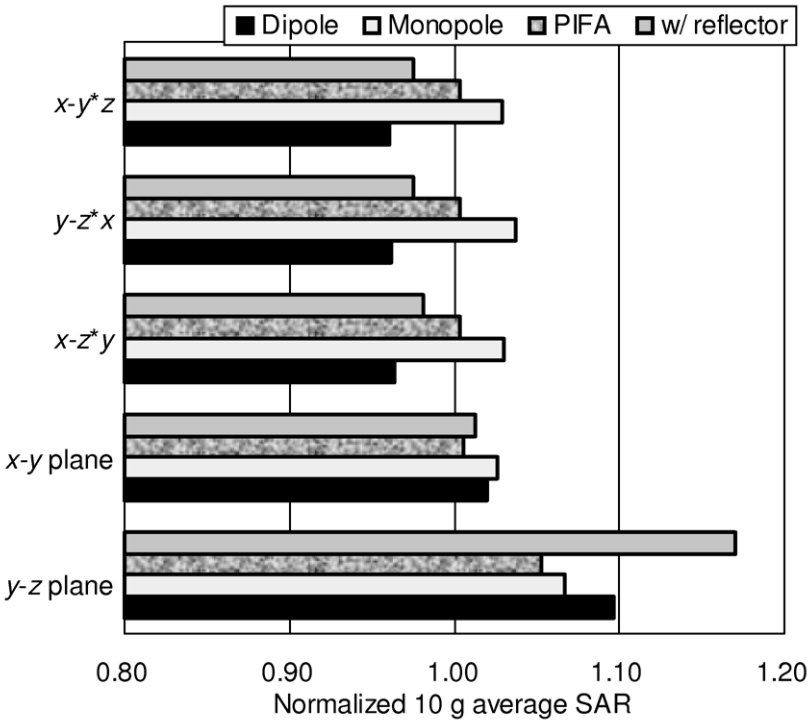

(a) 900 MHz

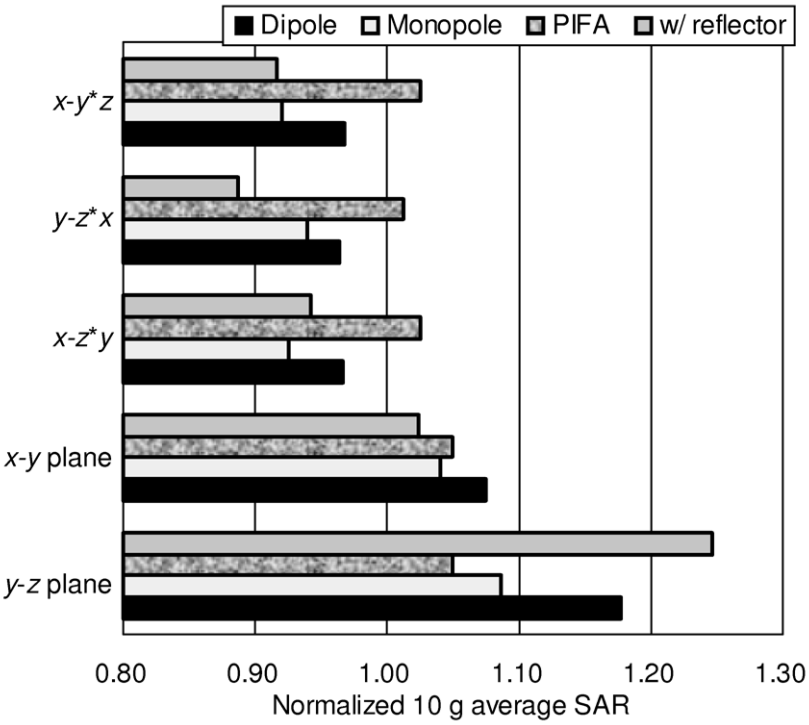

(b) 2 GHz

Fig. 3.6 Normalized local 10 g average SAR using the SAR distribution on the planes in the cubic model ($d = 15$ mm).

Figures 3.7 (a) and (b) show the calculated results of the local 10 g average SAR in the cubic model using the distribution on the axes at 900 MHz and 2 GHz. It is confirmed that the results using the $x-y-z$ axes, and the $x-y$ axes is in agreement with the reference within –4% to +4% at 900 MHz, as shown in Fig. 3.7 (a). In addition, the result suggests that the evaluation of the 10 g average SAR using the data on the specific axis is difficult. On the other hand, the difference of the average SAR is within –9% to +5% at 2 GHz when the data on the $x-y-z$ axes and $x-y$ axes are used for averaging, as shown in Fig. 3.7 (b). Therefore, the local 10 g average SAR in the cubic model can evaluate using the distribution on the $x-y-z$ axes or the $x-y$ axes at both frequencies.

From these results, the SAR distribution in the horizontal plane or axes to evaluate the local 10 g average SAR is necessary because the variation in the data of the horizontal direction is larger than that of the vertical one.

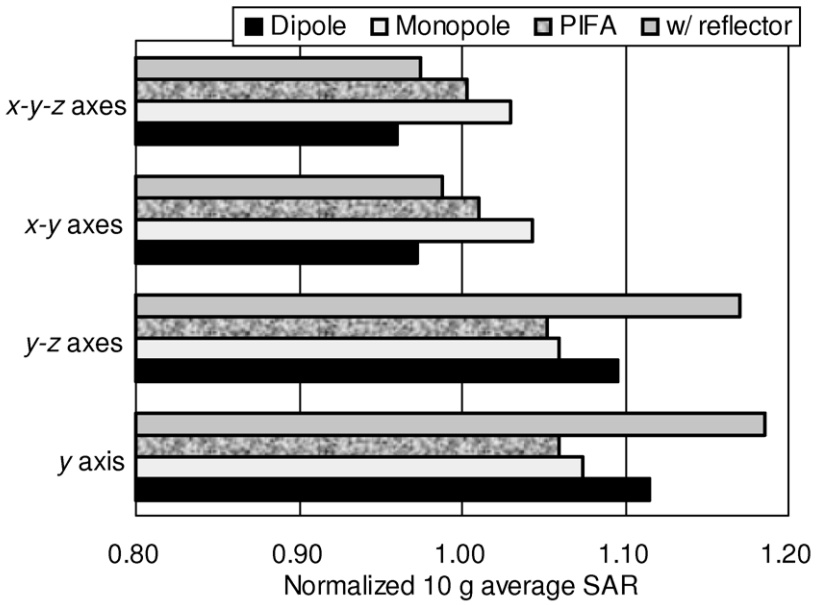

(a) 900 MHz

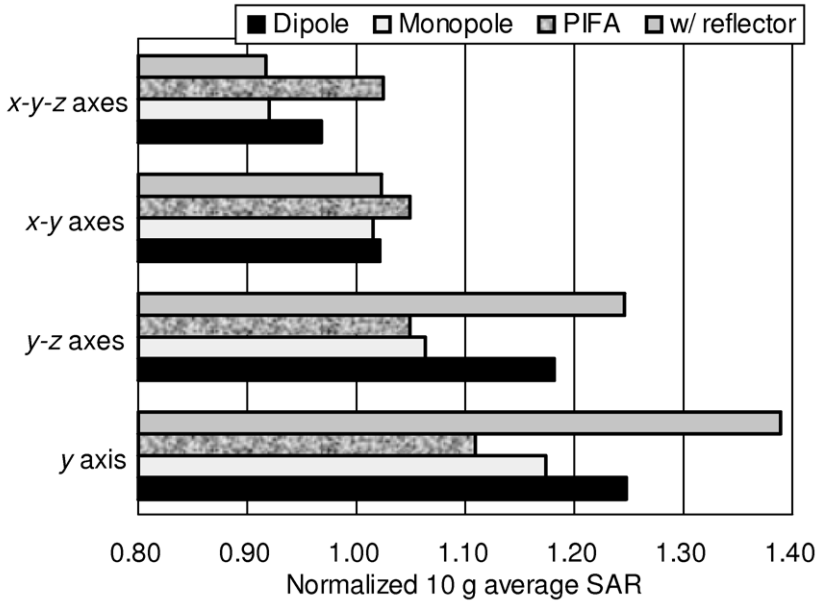

(b) 2 GHz

Fig. 3.7 Normalized local 10 g average SAR using the SAR distribution on the axes in the cubic model ($d = 15$ mm).

3.3.2 Results of the spherical model

Figures 3.8 (a) and (b) show the calculated results of the local 10 g average SAR in the spherical model using the SAR distribution on the planes at 900 MHz and 2 GHz. Here, the average SAR using the data on the $x - z$ plane is omitted because it is difficult to measure the SAR on this plane in the spherical model using the thermographic method. As shown in Fig. 3.8 (a), it has been confirmed that the 10 g average SAR using the data in the planes is in agreement with the reference within –12% to +11% at 900 MHz. On the other hand, Fig. 3.8 (b) indicates that the difference of the average SAR between the two methods is within –9% to +12% at 2 GHz, except for the result by use of the data on the $y - z$ plane. From these results, the differences of the 10 g average SAR in the spherical model is within $\pm$ 12% at 900 MHz and 2 GHz when the SAR distribution on the two planes or the $x - y$ plane is used.

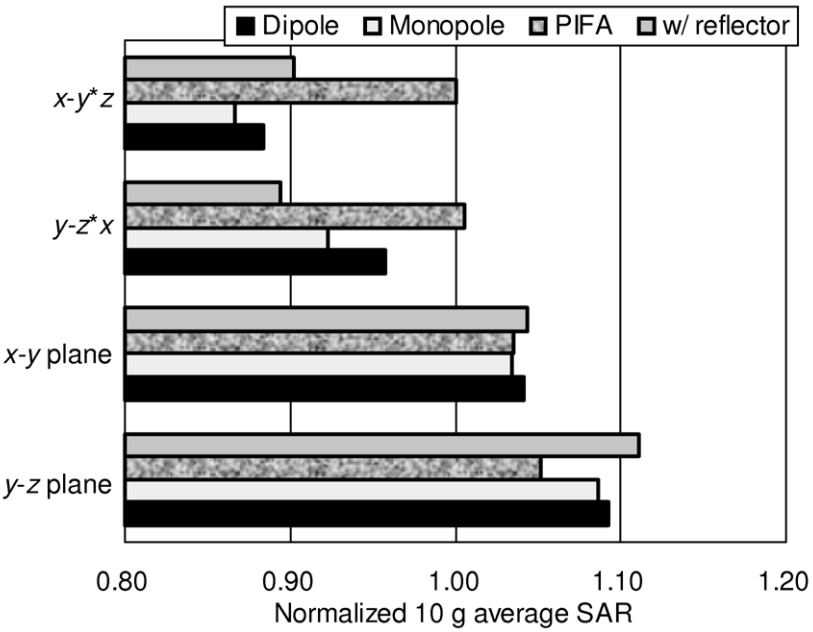

(a) 900 MHz

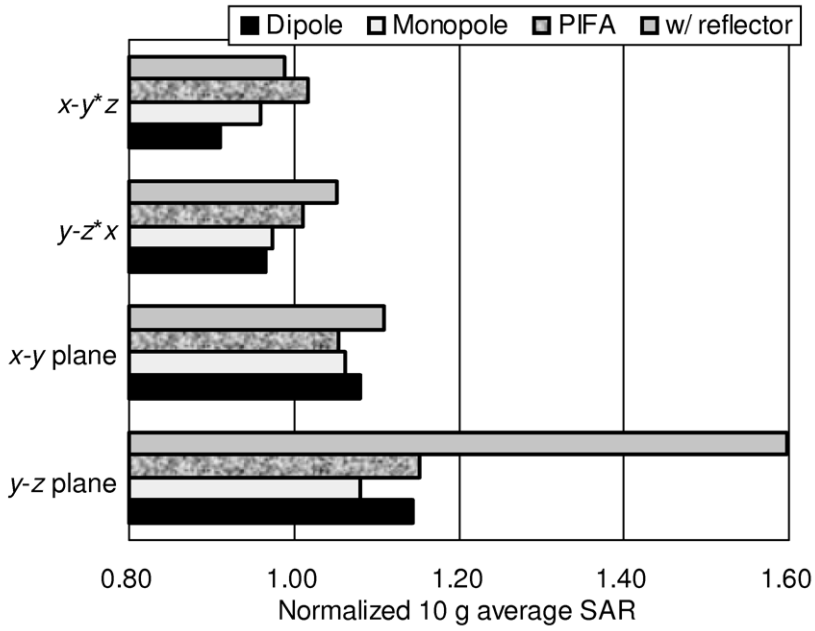

(b) 2 GHz

Fig. 3.8 Normalized local 10 g average SAR using the SAR distribution on the planes in the spherical model ($d = 15$ mm).

Figures 3.9 (a) and (b) show the calculated results of the local 10 g average SAR in the spherical model using the SAR distribution on the average SAR of the axes. From Fig 3.9 (a), it has been confirmed that the 10 g average SAR, which is calculated using the data on the $x-y-z$ axes or $x-y$ axes, is in agreement with the reference within –13% to +3% at 900 MHz. On the other hand, Fig. 3.9 (b) indicates that the average SAR, which is based on the data in the $x-y-z$ axes or $x-y$ axes, is within –7% to +17% at 2 GHz.

As shown in Figs. 3.6 to 3.9, the differences of the SAR between the two methods in the spherical model are larger than those in the cubic model because a curvature of the spherical model causes the variation in the SAR on the y or z direction. In addition, the large difference is obtained when the dipole antenna with the planar reflector is close to the spherical model at both frequencies because the peak SAR is arisen on the large curvature of the phantom surface. Hence, it is difficult to evaluate the local 10 g average SAR, which is the deviation from the reference within $\pm$ 10%, when the peak SAR arises on the large curvature position in the model.

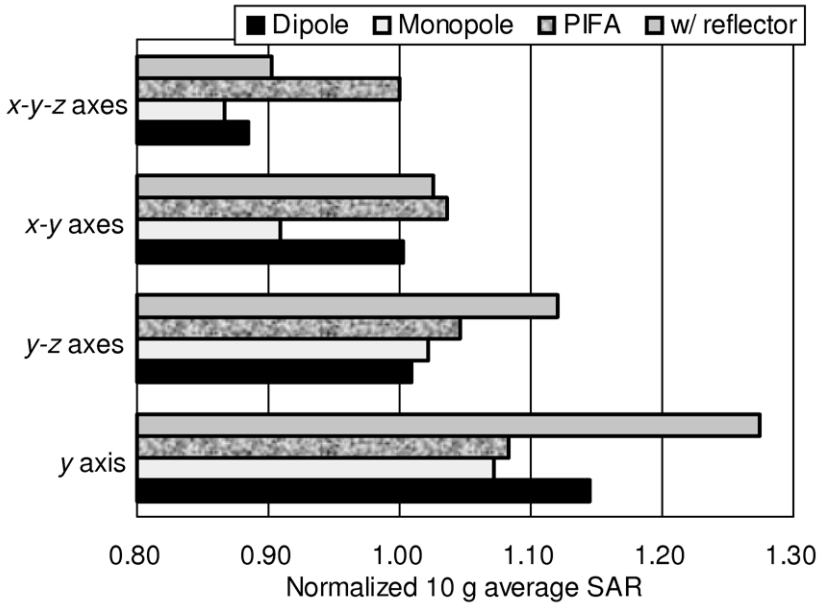

(a) 900 MHz

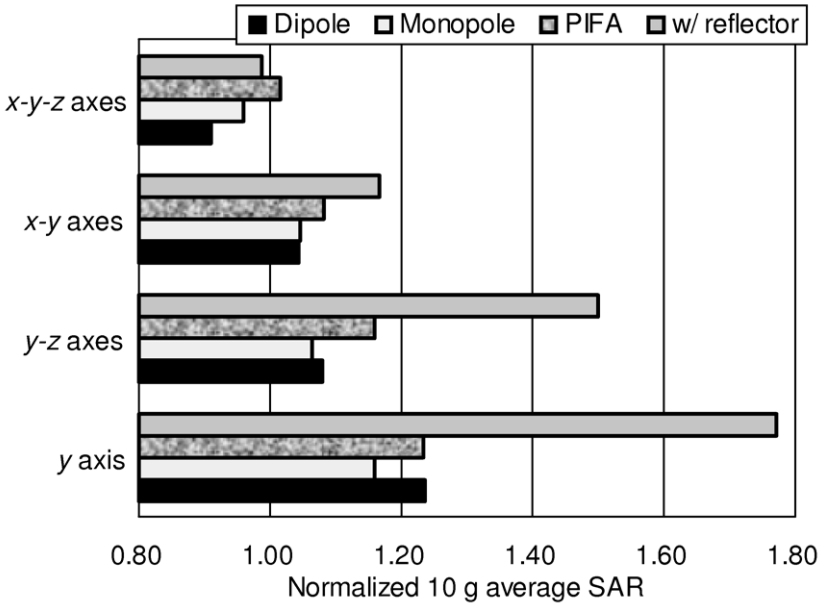

(b) 2 GHz

Fig. 3.9 Normalized local 10 g average SAR using the SAR distribution on the axes in the spherical model ($d = 15$ mm).

3.4 Investigation of application

3.4.1 Distance between antennas and phantoms

In Section 3.3, it was shown that the local average SAR by use of the proposed method when the distance between the feed point of the antennas and the models d is constantly 15 mm. However, d is dependent on the antennas, the situation, etc. Therefore, here I show the dependence of the validity of the proposed method on d. Here, the half-wave dipole antenna and the cubic model, as shown in Fig. 3.2 (a), are used for the investigation. In addition, the frequency is fixed, for instance at 900 MHz.

Table 3.2 describes the reference value of the local 10 g average SAR when d is varied. These SARs are calculated by same method in Section 3.2.3. Here, the SARs are normalized to these values. Figure 3.10 represents the local 10 g average SAR in the cubic model when the d is varied from 5 to 25 mm. As shown in Fig. 3.10, the difference between the SAR evaluated by the proposed method and the reference value are within $\pm$ 10% when d is larger than 10 mm. On the other hand, the differences are larger than –10% except the result using the data on the $x-y$ plane because the high SAR are corrected on neighborhood of feed point. In addition, the increase in the difference of the result by use of data on the $x-y$ plane is also obtained because the variation in the SAR distribution on z direction is increased. Moreover, it is confirmed that the SAR vs. frequency based on the $x-y$ axes is differed from that based on the $x-y$ plane below 15 mm because the attenuation in the phantom is dependent on the d at 900 MHz. From these results, the deviation of the local 10 g average SAR using the proposed method is within $\pm$ 10% when d is larger than 10 mm at 900 MHz.

Table 3.2 Reference value of the local 10 g average SAR in the cubic model by use of the half-wave dipole antenna at 900 MHz when d is varied from 5 mm to 25 mm

d [mm]	SAR_{10g} [W/kg]
5	9.38
10	8.33
15	6.76
20	5.34
25	4.08

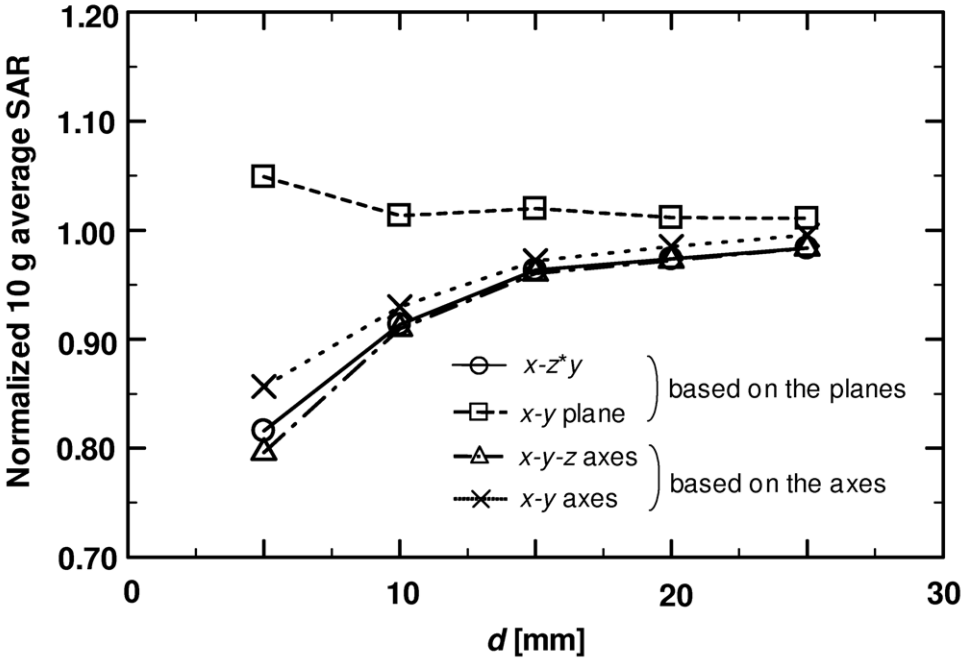

Fig. 3.10 Normalized 10 g average SAR vs. d.

3.4.2 Dependence of frequency

This Section shows the local 10 g average SAR evaluated by the proposed method when the frequency is varied. Here, the half-wave dipole antenna and the cubic model are used for the investigation. The axial length of the antenna is adjusted to 0.5 λ at each frequency. In addition, the d is 15 mm.

Table 3.3 describes the electric constants of the head model [12] and reference value of the local 10 g average SAR at each frequency. From now on, the average SARs are normalized to these values. Figure 3.11 represents the local 10 g average SAR in the cubic model using the simple method at 300 MHz, 900 MHz, 1.5 GHz, 2 GHz, 2.45 GHz, and 3 GHz. As shown in Fig. 3.11, the difference of the local 10 g average SAR is within $\pm$ 10% at each frequency. However, the difference is increased above 2 GHz when the results are evaluated using the data on the $x-y$ plane and $x-y$ axes because the incident wave from the 0.5 λ dipole antenna on the average area resembles the spherical wave above 2 GHz. Therefore, the SAR in the z direction is necessary to more accurate evaluate the local 10 g average SAR above 2 GHz. From these results, it has been confirmed that this method can apply the local average SAR estimation in the cubic model at 300 MHz to 3 GHz.

Table 3.3 Dielectric constants of the cubic model and the reference value of the local average SAR when the frequency is varied (d =15 mm)

f [MHz]	ε_r	σ [S/m]	$\mathrm{SAR}_{10\,\mathrm{g}}$ [W/kg]
300	45.3	0.87	1.61
900	41.5	0.97	6.76
1500	40.5	1.20	10.5
2000	40.0	1.40	11.2
2450	39.2	1.80	11.1
3000	38.5	2.40	9.99

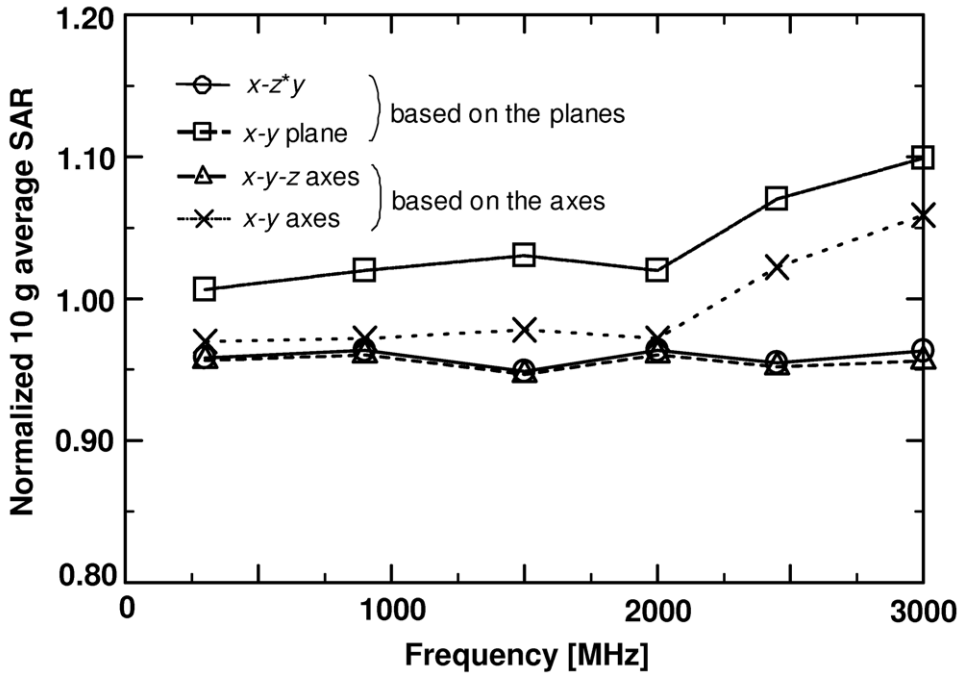

Fig. 3.11 Normalized 10 g average SAR vs. frequency (d =15 mm).

Realistic head model

This Section introduces the local 10 g average SAR in the realistic model, which is included in SEMCAD, evaluated by the proposed method. Here, the half-wave dipole antenna and the antenna with the planar reflector at 2 GHz are used because the deviations from the reference in these cases are the worst, as expressed by Section 3.3. The distance between the antenna and the left ear hole of the head model is 15 mm, as shown in Fig. 3.12. In addition, the dielectric constants of the head model at 2 GHz are as shown in Table 3.3. Moreover, the dielectric constants of the shell of the head model are $\varepsilon_r = 4.5$ and $\sigma = 0$. Furthermore, the references of the local 10 g average SAR are 7.43 W/kg (half-wave dipole antenna) and 0.51 W/kg (half-wave dipole antenna with the planar reflector). From now on, the SARs are normalized to these values.

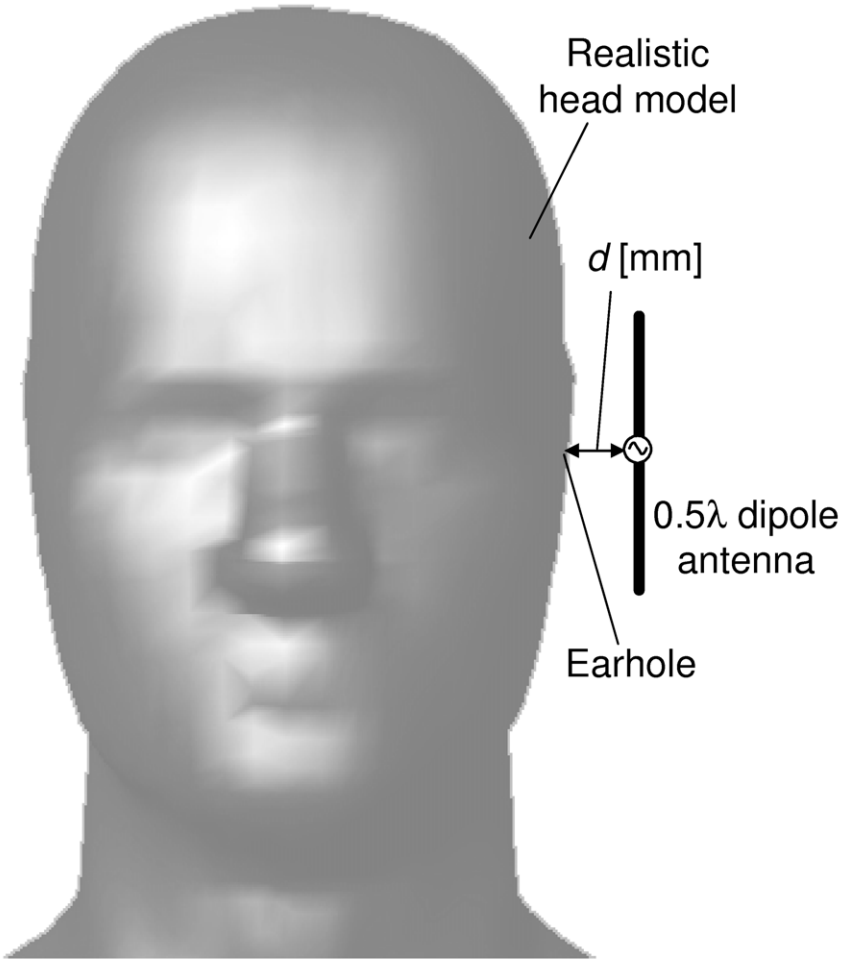

Fig. 3.12 Realistic head model.

Figure 3.13 illustrates the normalized 10 g average SAR, which is evaluated by the proposed method, in the realistic head model at 2 GHz. Here, the average SAR using the data on the $x-z$ plane is omitted in the same way as discussed in Section 3.3.2. As shown in Fig. 3.13, it is confirmed that the average SAR using the data in the specific planes and axes is in agreement with the reference within –15% to +2%. In addition, the results resemble those of the spherical model because the peak SAR on the $y-z$ plane arises on the curvature position in the model. Consequently, I have confirmed that the proposed method can evaluate the average SAR in the realistic head model within ± 15% of the deviation from the reference.

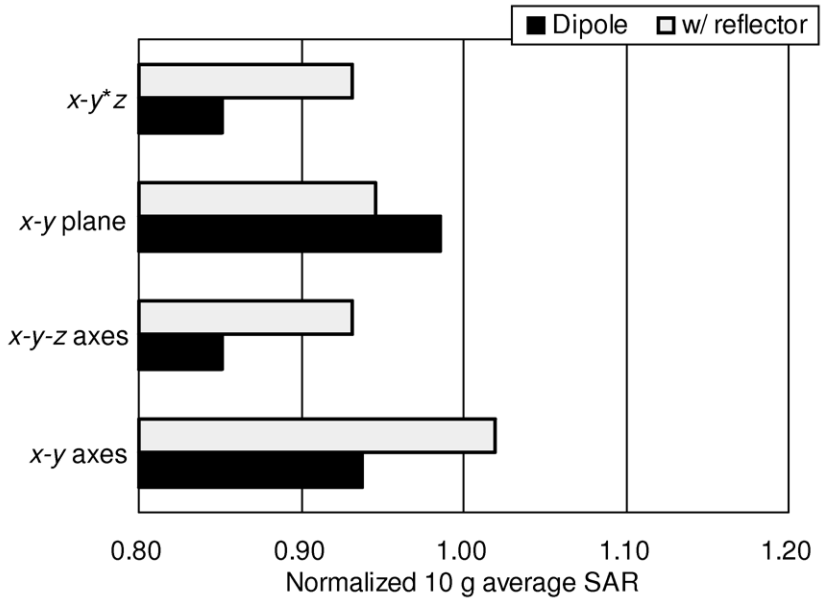

Fig. 3.13 Normalized 10 g average SAR in the realistic head model at 2 GHz (d =15 mm).

3.5 Conclusions

This Chapter proposed the simple evaluation method of the estimating local 10 g average SAR, which is based on the SAR distribution in the specific plane or axes by use of the thermal technique.

First, the limit of simplification was investigated when the four types of the antenna, which is the half-wave dipole antenna, monopole antenna mounted on the metal box, PIFA, and half-wave dipole antenna with the planar reflector, were close to the COST244 cubic and spherical head model at 900 MHz and 2 GHz. As a result, it had been confirmed that the SAR distribution in the horizontal plane or axes is necessary to evaluate the local 10 g average SAR because the variation in the horizontal direction is larger than that in the vertical one using the antennas. In addition, the proposed method was almost able to evaluate the local 10 g average SAR, which is the deviation within ± 10%, in the cubic model at 900 MHz and 2 GHz. Moreover, the difference between the two methods in the spherical model was within –12% to +17% at both frequencies.

Next, the effect of the distance between the antenna and the head model on the averaged SAR using this method was evaluated at 900 MHz to investigate the application of this method. The results indicated the deviation of the local 10 g average SAR was within ± 10% when the distance between the two is larger than 10 mm. Third, the dependence of the proposed method on the frequency was investigated at 300 MHz to 3 GHz. It was found from the result that the proposed method can be applied to the local average SAR estimation in the cubic model at 300 MHz to 3 GHz.

Finally, I evaluated the average SAR in the realistic head model at 2 GHz. The result reached that the proposed method also evaluates the average SAR in the realistic head model within ± 15% of the deviation. From these investigations, I may conclude the proposed

method can evaluate the local 10 g average SAR using the distribution on the optimum planes and axes within ± 10% of the deviation at 300 MHz to 3 GHz, except in special cases.

In the near future, confirmation of the validity of this method using the thermographic method in various cases will be done.

Chapter 4 Effect of the variation in dielectric constants of the phantom on the local SARs

4.1 Introduction

Many studies have been conducted on the estimation of potential health effects caused by the microwaves radiated from mobile communication devices. The primary dosimetric parameter for the evaluation of EM waves exposure is the SAR above 100 kHz. Many countries are adopting or expected to adopt the guidelines, which define the basic limit for local exposure to be the SAR averaged over a volume of 1 g or 10 g. The SAR is generally estimated from numerical simulation and experimental evaluation. In the experimental evaluation methods, the biological tissue-equivalent phantom is usually used to realize the human tissue in most of the cases, as expressed by Section 2.3.

However, it is difficult to realize perfect agreement of dielectric constants (relative permittivity, conductivity) between the phantom and the human tissue because of various factors; e.g., fabrication error, evaporation as times go by, etc. In the measurement, differences of dielectric constants between the two cause an error on the estimated SAR. Hence, it is necessary to understand the effects of inaccurate dielectric constants of the phantom on the local averaged SARs in order to realize the precision evaluation.

To the author's knowledge, several papers on the effect of the inaccurate dielectric constants on the SAR have been published. However, these papers proposed only the special

cases; e.g., variation in the dielectric constants at half of twice [46], ± 15% change in the constants [47]. On the other hand, the input impedance of the antenna is hardly due to the inaccurate dielectric constants as well known [3].

This Chapter proposes the effect of the inaccurate dielectric constants of the biological tissue-equivalent phantom on the local SARs in a human model when the dielectric constants are changed at 150 MHz, 900 MHz, 2 GHz, and 3 GHz. First, in Sections 4.2 and 4.3, the peak SAR, local 1 g and 10 g average SARs in the human model are calculated when the relative permittivity and conductivity are varied from criteria to ± 20%. Next, in Section 4.4, the variation in the SAR distribution inside the model, which is caused by the inaccuracy of the relative permittivity or conductivity, is evaluated to find the cause of the error of the local average SARs. In Section 4.5, the relationship between the variation in the relative permittivity or conductivity and the local SARs is investigated. Moreover, the effect of the shape on the variation in the local SAR is investigated when the dielectric constants are varied at 2 GHz. Finally, in Section 4.7, the corrective method of the variation in the SAR, which is caused by the inaccurate dielectric constants, is proposed.

In this dissertation, the local peak SAR is defined as the peak value of the SAR in the optional point (cell) of the tissue.

4.2 Models and method

4.2.1 Models

Figures 4.1 (a) and (b) show the basic model for calculations at 150 MHz and 900 MHz to 3 GHz. Figure 4.1 (a) represents a half-wave dipole antenna and a cylindroid human model [35]. The dimension of the cylindroid model is a major axis of 280 mm, a minor axis of 200 mm, and the height of 1300 mm. On the other hand, Fig. 4.1 (b) describes the antenna and a COST244 cubic human head model [38]. The dimension of the cube is 200 mm in a side. In addition, the distance between the feed point of the antenna and the phantom surface is 40 mm at 150 MHz and 15 mm at 900 MHz to 3 GHz in order to realize the actual situation.

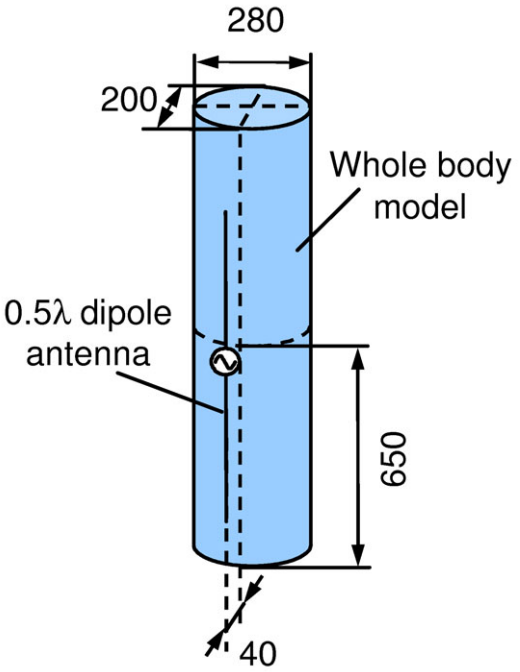

(a) 150 MHz

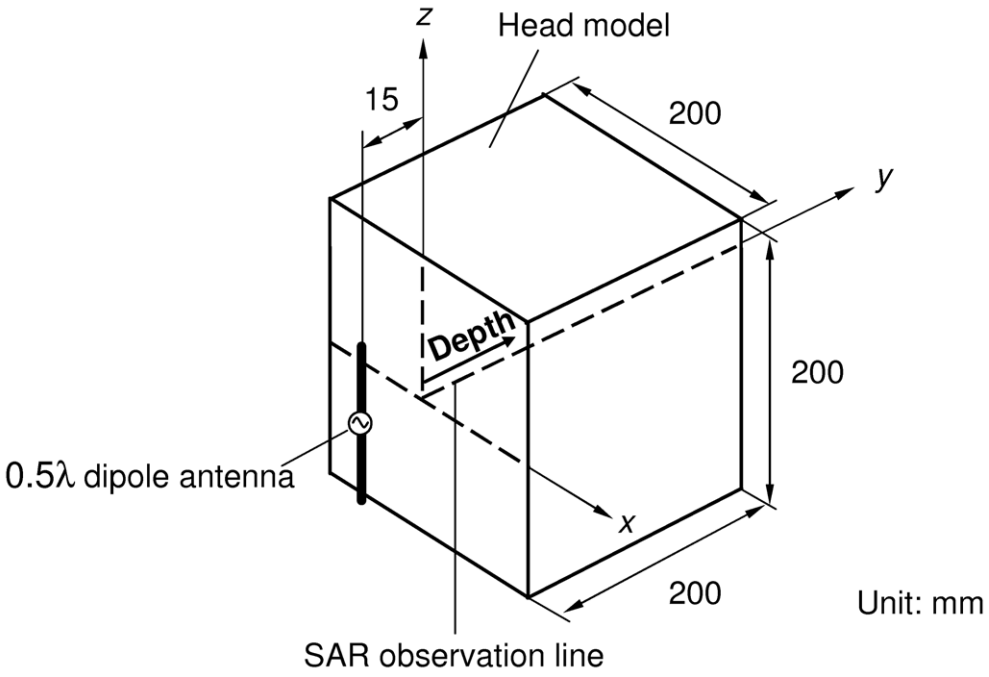

(b) 900 MHz to 3 GHz

Fig. 4.1 Models for calculations.

4.2.2 Numerical technique

The FDTD software (SEMCAD ver. 1.8) is used for the SAR calculating in the models. The parameters of the FDTD calculation employed in this Chapter are as follows: the cell size of antenna and phantom is 2.5 mm (150 MHz) or 1 mm (900 MHz–3 GHz); the absorbing boundary condition is the PML (eight layers); the calculation time is seven (150 MHz) or ten (900 MHz–3 GHz) periods to get converged results.

Table 4.1 describes the dielectric constants of the model and reference value of the local SARs at each frequency. Here, the dielectric constants at 150 MHz are the average value in the whole-body tissues (two third of muscle) [22], [52]. On the other hand, dielectric constants at 900 MHz to 3 GHz are used as values of the head [12]. From now on, ε_{r0} and σ_0 are used as reference values for the inaccuracy of dielectric constants. In addition, the local SARs are normalized to these values. Moreover, these values are normalized to the 1 W output of the antenna. Moreover, the density of the tissues $\rho = 1{,}000$ kg/m^3 at 150 MHz to 3 GHz.

Table 4.1 Dielectric constants of the model and criteria of local SARs

f [MHz]	ε_{r0}	σ_0 [S/m]	peak SAR [W/kg]	$SAR_{1\,g}$ [W/kg]	$SAR_{10\,g}$ [W/kg]
150	42.1	0.51	0.46	0.39	0.33
900	41.5	0.97	15.5	10.1	6.40
2000	40.0	1.40	33.3	19.5	10.6
3000	38.5	2.40	43.3	19.8	8.71

4.3 Dependence of the local SAR on the dielectric constants of the phantom

4.3.1 Effect of the variation in the relative permittivity or the conductivity

This Section suggests the variation in the local SARs when the only relative permittivity ε_r or conductivity σ is changed in order to confirm the effect of the ε_r or σ on the SARs.

Figure 4.2 shows the calculated result of the normalized local peak SAR when the normalized dielectric constant of the model in Fig. 4.1, $\varepsilon_r/\varepsilon_{r0}$ or σ/σ_0, is varied from 0.8 to 1.2 under the condition that the other is the unity at 150 MHz to 3 GHz. From now on, the local peak SARs were normalized to the referenced values in Table 4.1.

From this figure, the increase in the local peak SAR is proportional to the decrease in the $\varepsilon_r/\varepsilon_{r0}$. The reason of this result will be examined in Section 4.5. In addition, the increase in the local peak SAR is proportional to the increase in the σ/σ_0. Moreover, it is confirmed that the effect of the inaccurate conductivity on the local peak SAR is larger than that of the inaccurate relative permittivity.

As shown in Figure 4.2, the effect of the variation in the $\varepsilon_r/\varepsilon_{r0}$ on the peak SAR is proportional to the increase in the frequency. In addition, the effect of the change in the σ/σ_0 on the peak SAR is hardly due to the frequency. The reason of this result will be also examined in Section 4.5.

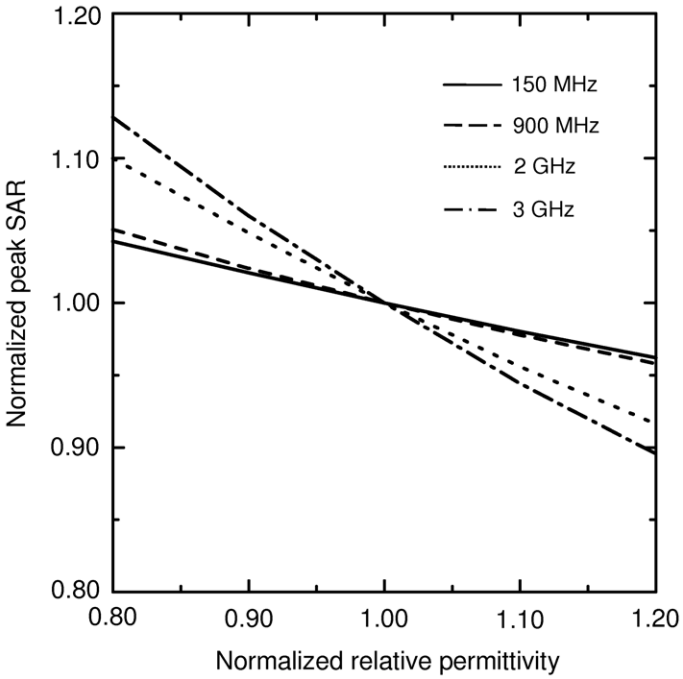

(a) Only ε_r is varied

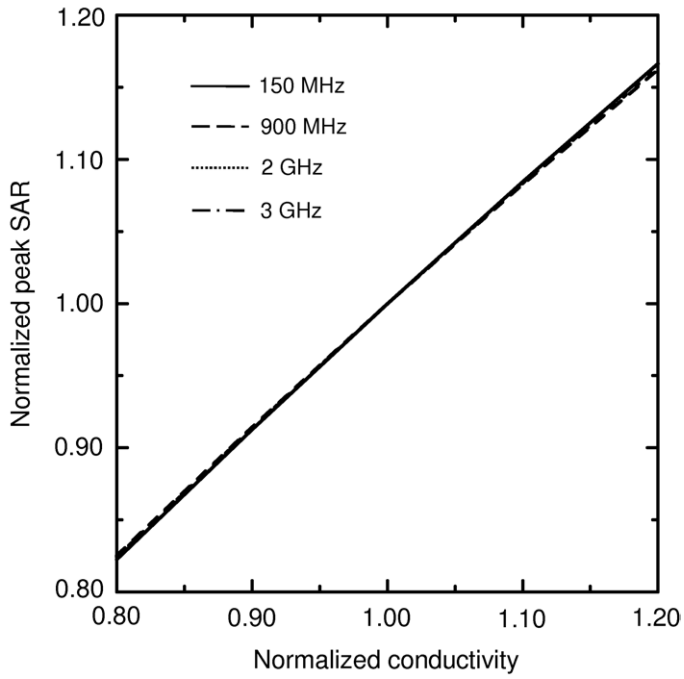

(b) Only σ is varied

Fig. 4.2 Effect of the inaccurate relative permittivity or conductivity on the peak SAR.

Figure 4.3 shows the calculated result of the normalized local 1 g average SAR when the $\varepsilon_r/\varepsilon_{r0}$ or σ/σ_0 is varied from 0.8 to 1.2 under the condition that the other is the unity at 150 MHz to 3 GHz. These 1 g average SARs were normalized to the referenced values in Table 4.1.

From this figure, the increase in the local 1 g average SAR is proportional to the decrease in the $\varepsilon_r/\varepsilon_{r0}$. In addition, the increase in the local 1 g average SAR is proportional to the increase in the σ/σ_0. Moreover, it is confirmed that the effect of the inaccurate conductivity on the local 1 g average SAR is also larger than that of the inaccurate relative permittivity.

As shown in Figure 4.3, the effect of the variation in the $\varepsilon_r/\varepsilon_{r0}$ or σ/σ_0 on the 1 g average SAR is due to the frequency. Especially, the effect of the $\varepsilon_r/\varepsilon_{r0}$ on the 1 g average SAR at 150 MHz is larger than that at 900 MHz as shown in Fig. 4.3 (a) because the average value is dependent on the variation in the internal SAR distribution. The variation in the internal SAR distribution will be examined in Section 4.4.

From Figs. 4.2 and 4.3, the effect of the inaccurate dielectric constants on the 1 g average SAR is smaller than that on the peak SAR because the SAR is due to the average volume.

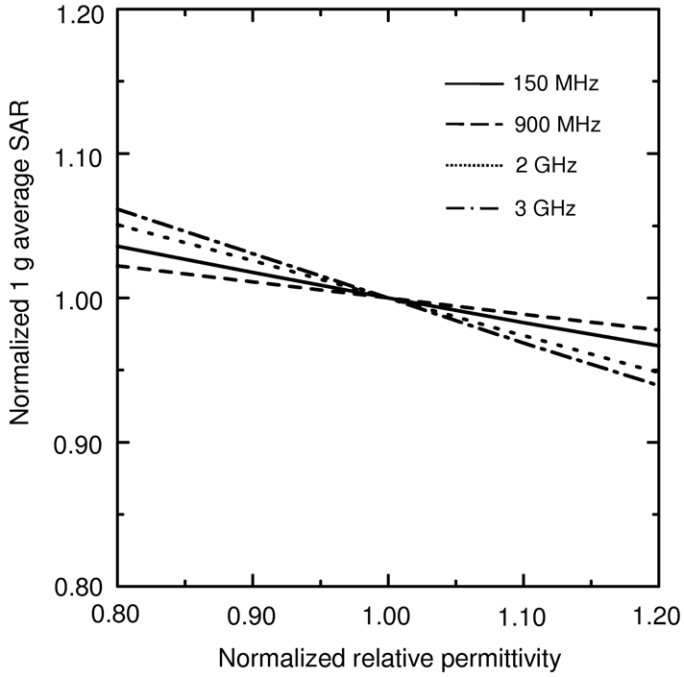

(a) Only ε_r is varied

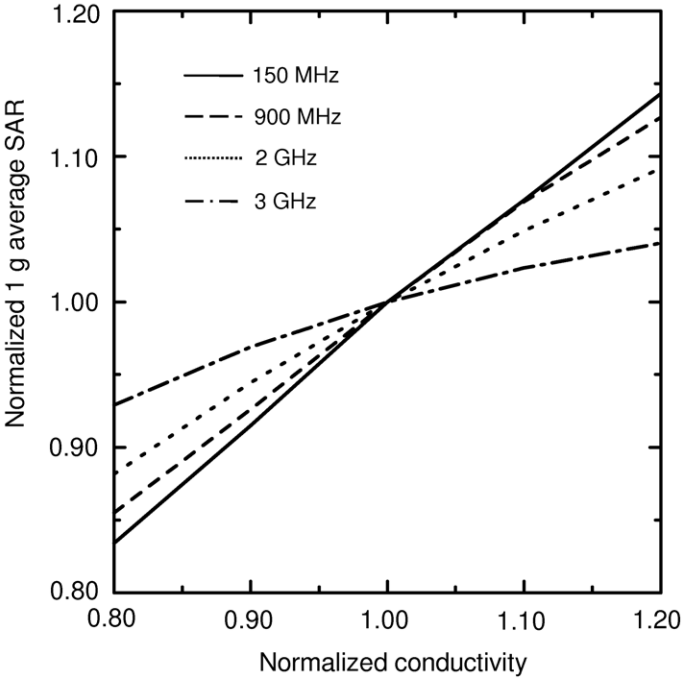

(b) Only σ is varied

Fig. 4.3 Effect of the inaccurate relative permittivity or conductivity on the 1 g average SAR.

Figure 4.4 illustrates the calculated result of the normalized local 10 g average SAR when the $\varepsilon_r/\varepsilon_{r0}$ or σ/σ_0 is varied from 0.8 to 1.2 under the condition that the other is the unity at 150 MHz to 3 GHz. These 10 g average SARs were normalized to the referenced values in Table 4.1.

As shown in Figure 4.4, the increase in the local 10 g average SAR is proportional to the decrease in the $\varepsilon_r/\varepsilon_{r0}$ at 150 MHz, 2 GHz, and 3 GHz. In addition, the increase in the local 10 g average SAR is proportional to the increase in the σ/σ_0 at 150 MHz to 2 GHz. Moreover, it is confirmed that the effect of the inaccurate conductivity on the 10 g average SAR is larger than that of the inaccurate relative permittivity at 150 MHz to 2 GHz. Furthermore, the influence of the variation in the $\varepsilon_r/\varepsilon_{r0}$ is larger than that of the σ/σ_0 at 3 GHz.

From this figure, the effect of the variation in the $\varepsilon_r/\varepsilon_{r0}$ or σ/σ_0 on the 10 g average SAR is due to the frequency. Especially, the 10 g average SAR is not due to the variation in the $\varepsilon_r/\varepsilon_{r0}$ at 900 MHz and σ/σ_0 at 3 GHz. In addition, the increase in the effect of the $\varepsilon_r/\varepsilon_{r0}$ is due to the increase in the frequency above 900 MHz. On the other hand, the decrease in the effect of σ/σ_0 on the SAR is dependent on the increase in the frequency. The reason of these results will be examined in Section 4.4.

From Figs. 4.3 and 4.4, the effect of the inaccurate dielectric constants on the 10 g average SAR is smaller than that on the 1 g average SAR because the SAR is due to the average volume. Therefore, it is necessary to evaluate the variation in the internal SAR distribution to clear the effect of the inaccurate dielectric constants on the average SARs. I will discuss the effect of the inaccurate dielectric constants on the internal SAR distributions in the following Section.

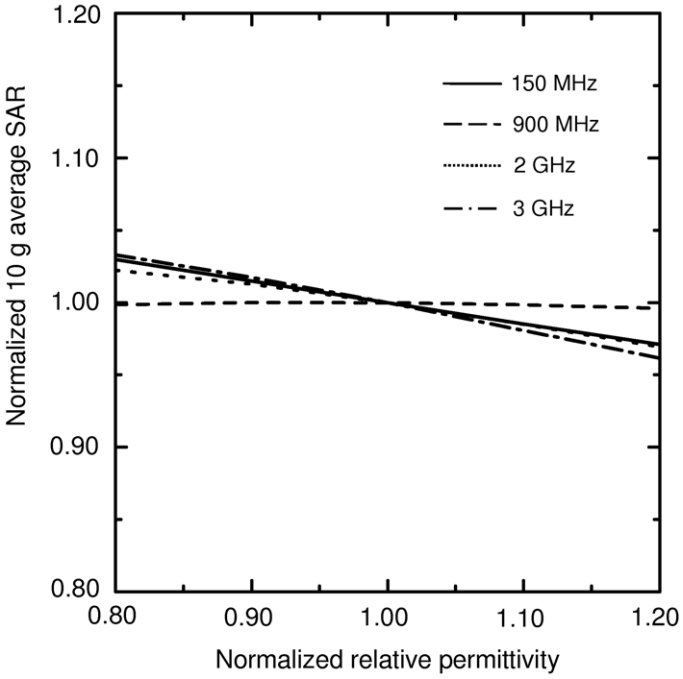

(a) Only ε_r is varied

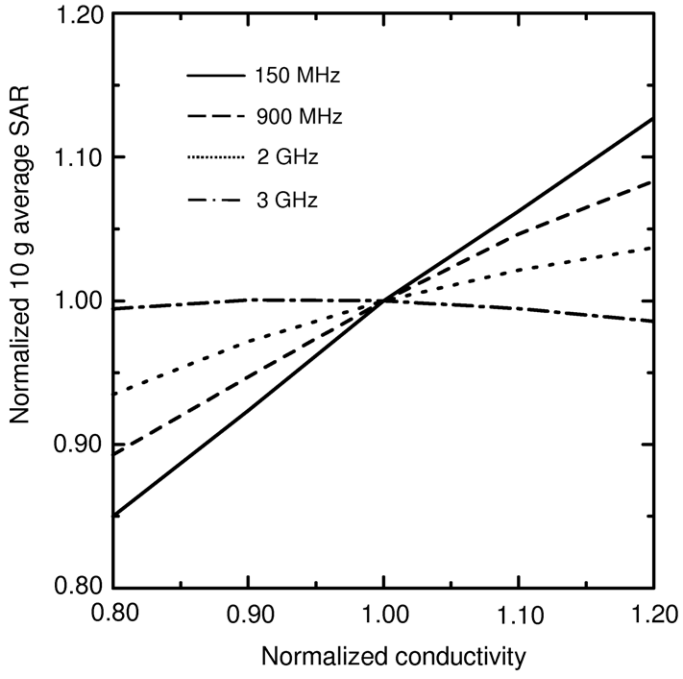

(b) Only σ is varied

Fig. 4.4 Effect of the inaccurate relative permittivity or conductivity on the 10 g average SAR.

4.3.2 Effect of the variation in the dielectric constants

In Section 4.3.1, the effect of the inaccurate relative permittivity or conductivity of the phantom on the local SARs was expressed. However, in the actual measurement, the dielectric constants are simultaneously varied. Therefore, in this Section, the error of the local average SARs is calculated when the dielectric constants of the phantom are simultaneously changed at 150 MHz to 3 GHz.

Figures 4.5, 4.6, 4.7, and 4.8 show the calculated result of the normalized local 1 g and 10 g average SAR using a contour line when the normalized dielectric constants, which are the $\varepsilon_r/\varepsilon_{r0}$ and σ/σ_0, are simultaneously varied from 0.8 to 1.2 at 150 MHz, 900 MHz, 2 GHz, and 3 GHz. Here, the variation in the local peak SAR is omitted.

As shown in Figs. 4.5 to 4.8, the effect of the inaccurate dielectric constants on the 1 g average SAR is larger than that on the 10 g average value. In addition, it is also confirmed that the difference between the variation in the 1 g average SAR and that in the 10 g average value is due to the frequency. Moreover, the variation in the SAR caused by the inaccurate dielectric constants is evaluated by use of these results. For example, as shown in Fig. 4.7 (b), the variation in the local 10 g average SAR is less than –5% to 0% at 2 GHz, when the $\Delta\varepsilon_r/\varepsilon_{r0} = -10\%$, $\Delta\sigma/\sigma_o = -15\%$.

Moreover, I can see from these results that the effect of the inaccurate dielectric constants on the local average SARs are almost equal to the sum of the change in the SAR caused by the inaccurate relative permittivity and that by conductivity. Therefore, the effect of the inaccurate dielectric constants on the local SARs is able to evaluate using Figs. 4.3 and 4.4 at 150 MHz to 3GHz.

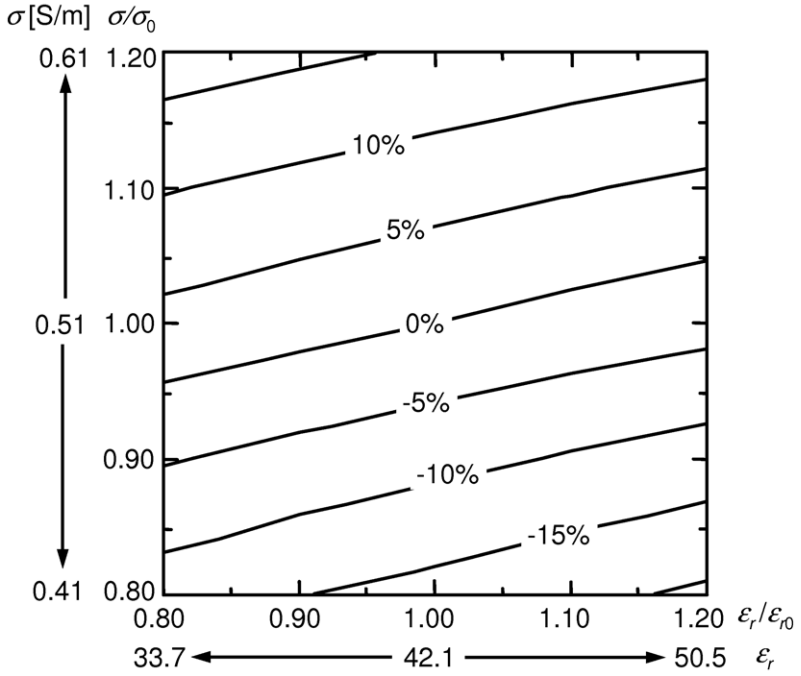

(a) 1 g average SAR

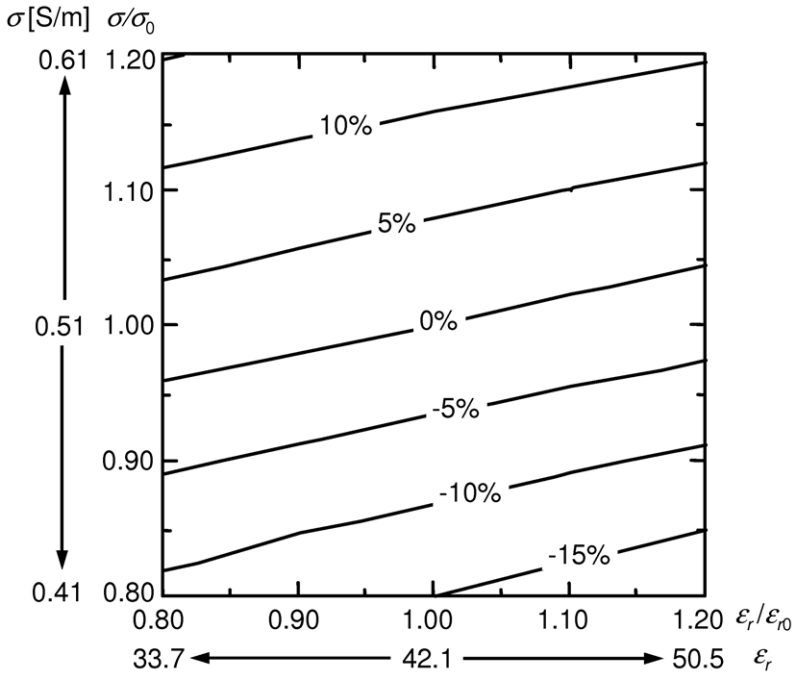

(b) 10 g average SAR

Fig. 4.5 Effect of the inaccurate dielectric constants on the local average SARs at 150 MHz (contour).

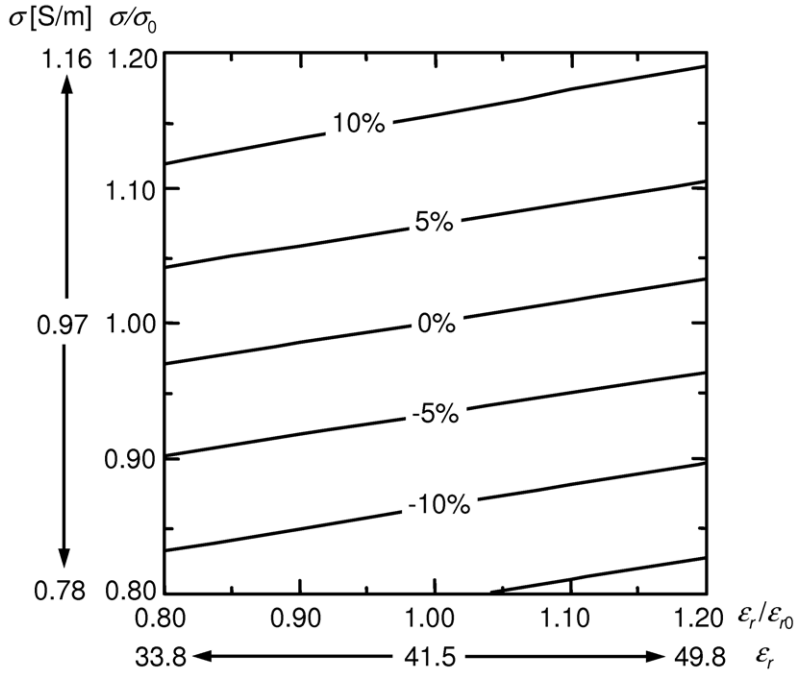

(a) 1 g average SAR

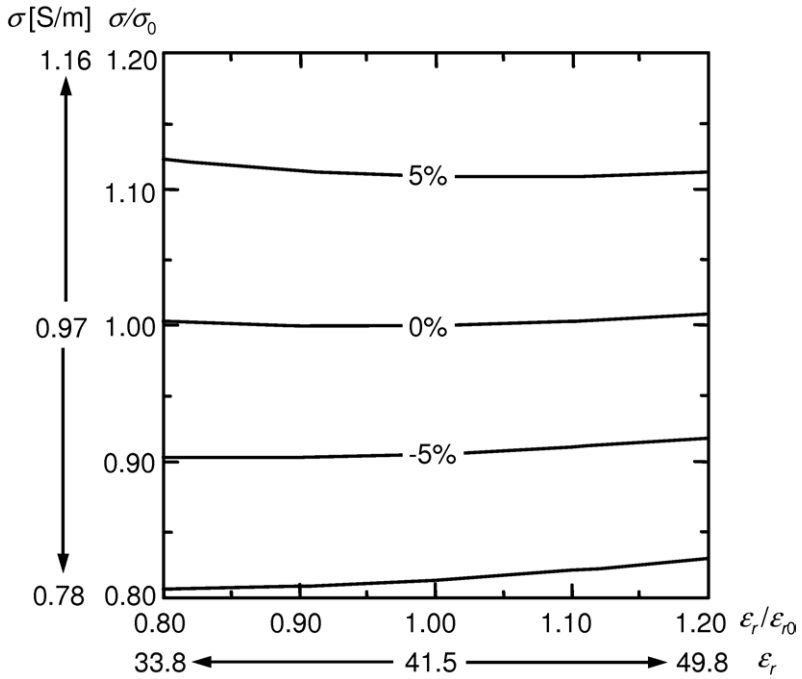

(b) 10 g average SAR

Fig. 4.6 Effect of the inaccurate dielectric constants on the local average SARs at 900 MHz (contour).

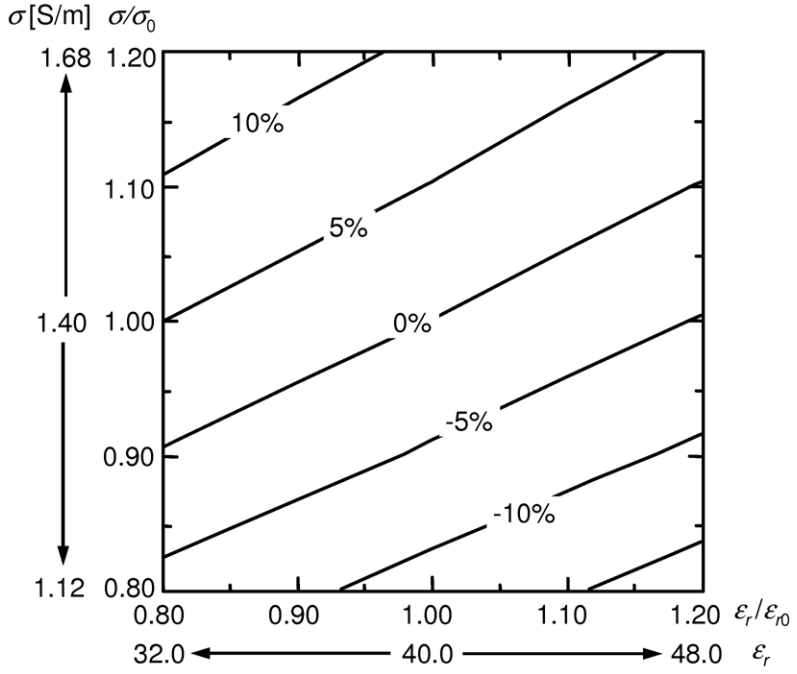

(a) 1 g average SAR

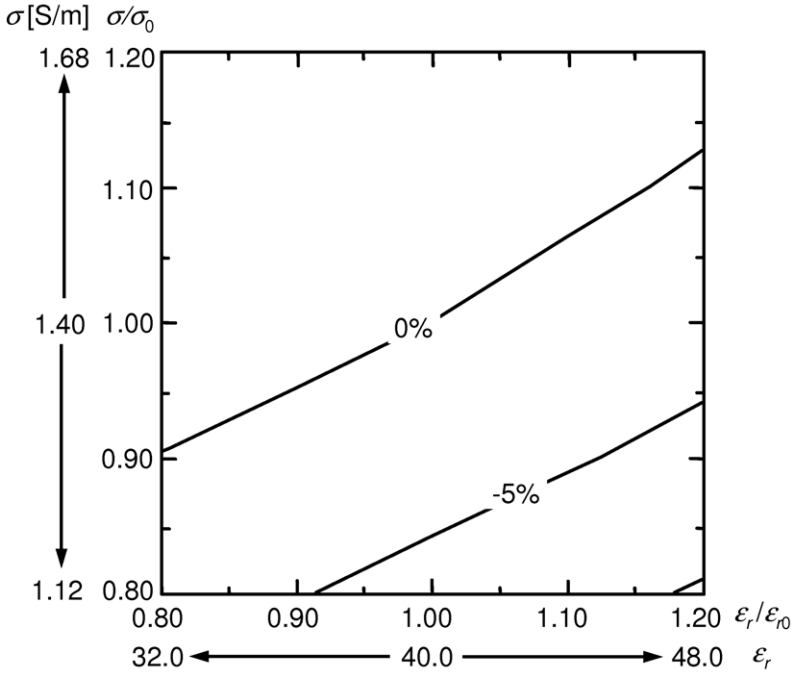

(b) 10 g average SAR

Fig. 4.7 Effect of the inaccurate dielectric constants on the local average SARs at 2 GHz (contour).

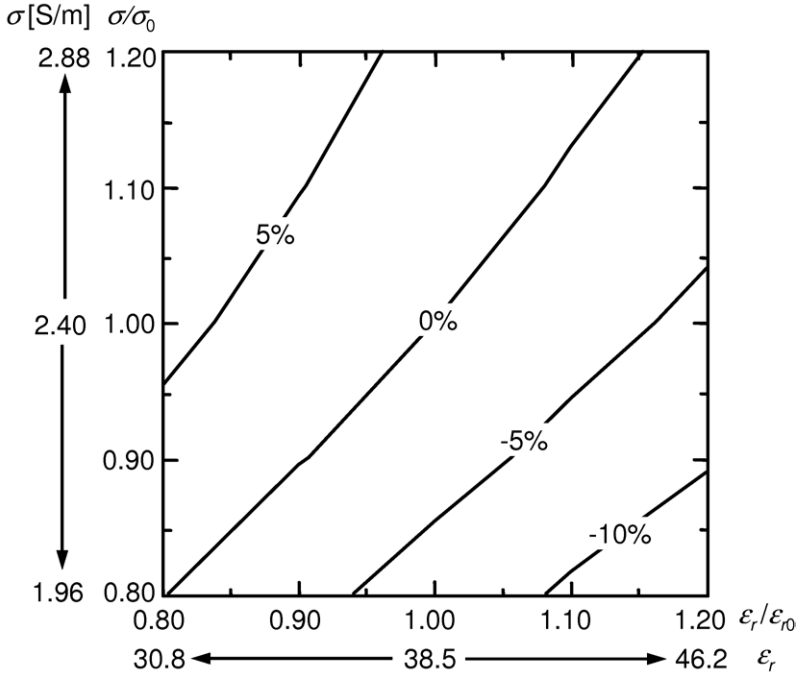

(a) 1 g average SAR

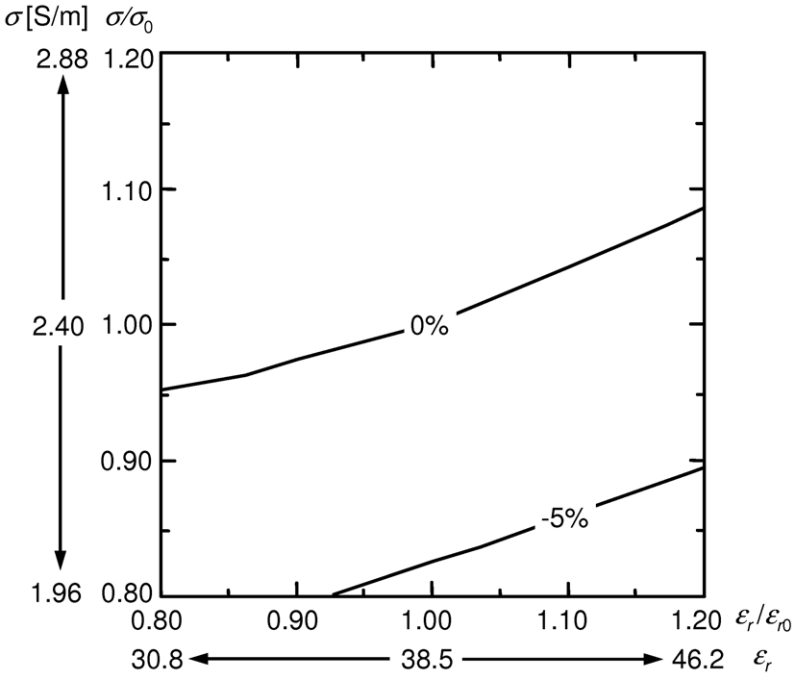

(b) 10 g average SAR

Fig. 4.8 Effect of the inaccurate dielectric constants on the local average SARs at 3 GHz (contour).

4.4 Effect of the variation in the dielectric constants on the SAR distribution inside the phantom

Section 4.3 proposed the effect of the inaccurate dielectric constants of the phantom on the SAR at point or averaged value. Such variation in the SARs is caused by the change in the SAR distribution in the phantom. Therefore, in this Section, the effect of the inaccurate electric constants on the internal SAR distribution of the phantom is calculated.

4.4.1 Internal SAR distribution

Figures 4.9, 4.10, 4.11, and 4.12 illustrate the calculated result of the normalized SAR distribution on the observation line [see Fig. 4.1], when the $\varepsilon_r/\varepsilon_{r0}$ or σ/σ_0 is varied at 0.8, 1.0, and 1.2 under the condition that the other is the unity at 150 MHz to 3 GHz.

As shown in Fig. 4.9, the attenuation inside the phantom is hardly due to the variation in the inaccurate dielectric constant at 150 MHz. In addition, the variation in the SAR in the 1 g average area (depth = 0–10 mm) is almost equal to that in the 10 g average area (depth = 0–21.5 mm). Therefore, the effect of the inaccurate dielectric constants on the local 1 g average SAR is almost equal to that of the 10 g average value, as given by Fig. 4.5.

From Fig. 4.10 (a), the variation in the in the SAR distribution caused by the inaccurate ε_r at the depth = 0–10 mm conflicts with that at the depth = 10–21.5 mm at 900 MHz. Therefore, the variation in the local 10 g average SAR is hardly due to the change in the ε_r such as given by Fig. 4.6 (b). On the other hand, As shown in Fig. 4.10 (b), the variation in the in the SAR caused by the σ at the depth = 0–10 mm is larger than that at the depth = 10–21.5 mm. Hence, the variation in the 1 g average SAR is larger than that in the 10 g average value at 900 MHz such as provided in Fig. 4.6. Moreover, the dependence of the variation in the SAR distribution caused by the σ is larger than that by the ε_r.

I can see from Figs. 4.11 (a) and (b) that the variation in the average SARs caused by

the inaccurate ε_r or σ is mainly due to the change in the SAR distribution at the depth = 0–7.5 mm. In addition, the dependence of the variation in the SAR distribution caused by the σ is larger than that by the ε_r. Therefore, the variation in the 1 g average SAR is also larger than that in the 10 g average value at 2 GHz such as provided in Fig. 4.7.

As shown in Fig. 4.12 (a), the variation in the average SARs at 3 GHz caused by the inaccurate ε_r is mainly due to the change in the SAR distribution at the depth = 0–7.5 mm. On the other hand, it is found form Fig. 4.12 (b) that the variation in the SAR distribution caused by the inaccuracy of the σ at the depth = 0–10 mm conflicts with that at the depth = 10–21.5 mm. Hence, the variation in the local 10 g average SAR is hardly due to the inaccurate σ at 3 GHz such as given by Fig. 4.8 (b).

From Figs. 4.9 to 4.12, the variation in the attenuation of the SAR distribution, which is caused by the inaccurate electric constant, is due to the frequency. In addition, the variation in the attenuation caused by the increase in the ε_r conflicts with that in σ. Therefore, the inclination in the average SAR caused by the increase in the ε_r also conflicts that in σ such as Figs. 4.3 and 4.4.

These variations in the SAR distribution are due to the change in the attenuation constant of the phantom. The variation in the attenuation constant of the phantom will be examined in Section 4.4.2.

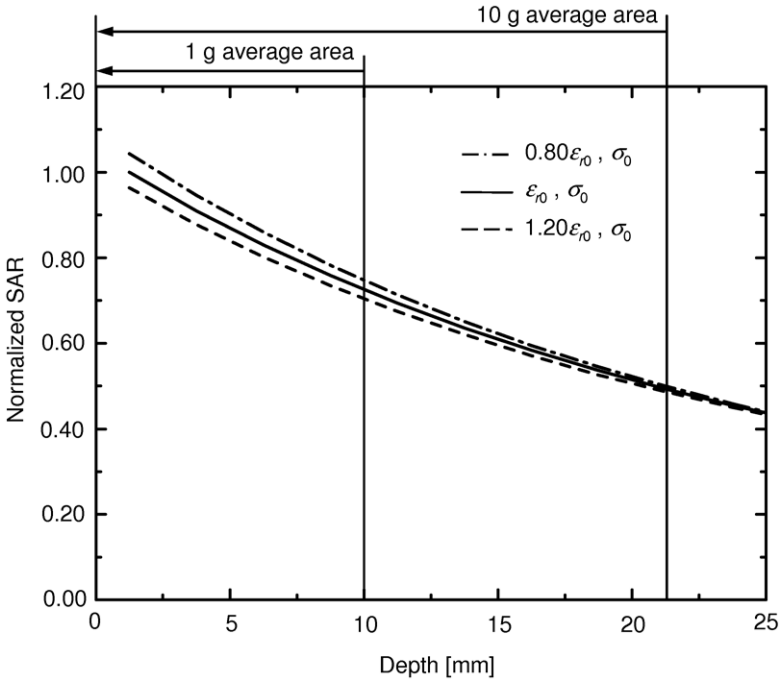

(a) Only ε_r is varied

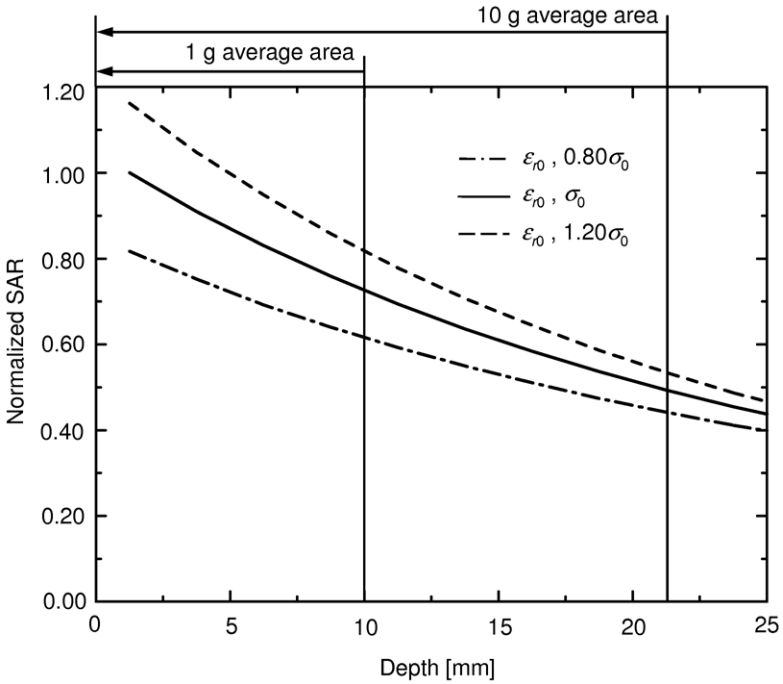

(b) Only σ is varied

Fig. 4.9 SAR distributions inside the phantom at 150 MHz.

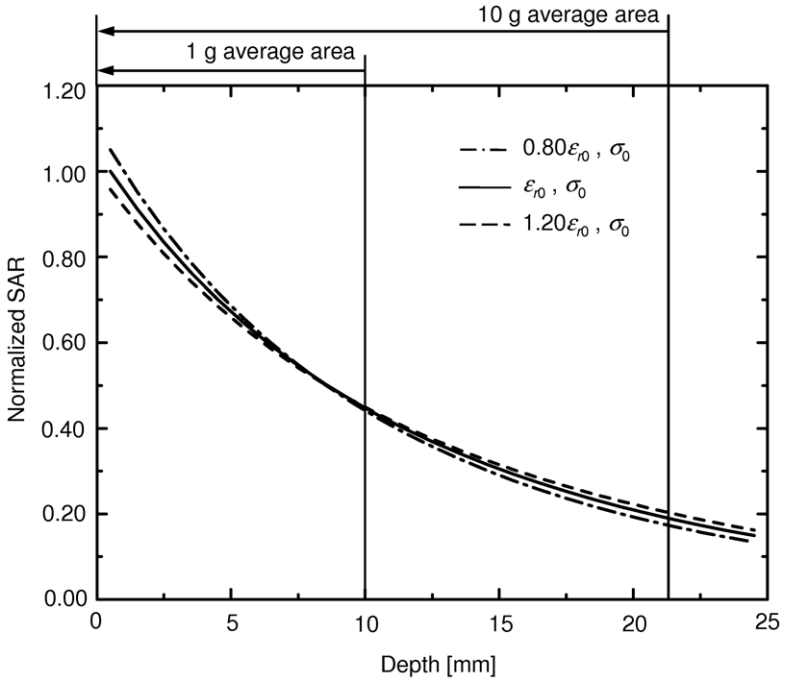

(a) Only ε_r is varied

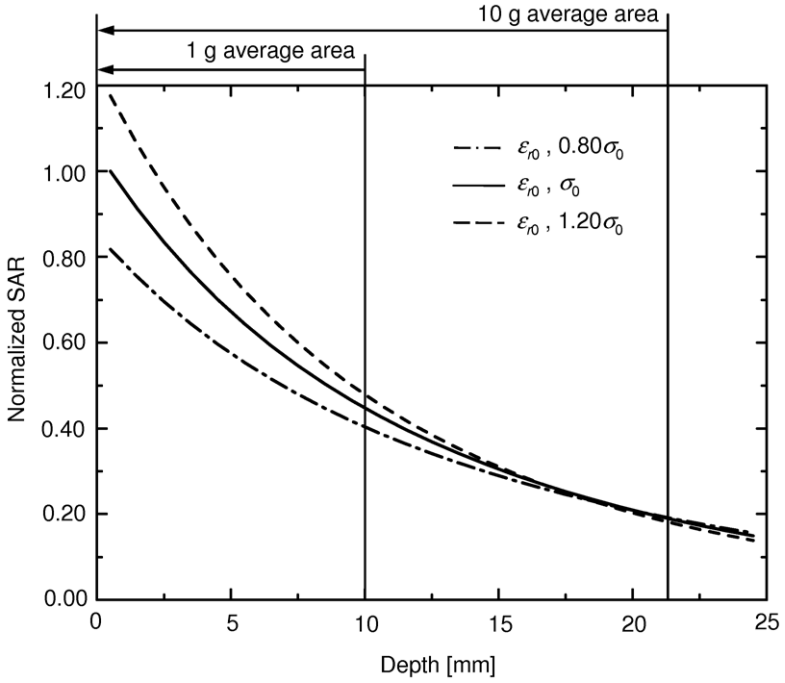

(b) Only σ is varied

Fig. 4.10 SAR distributions inside the phantom at 900 MHz.

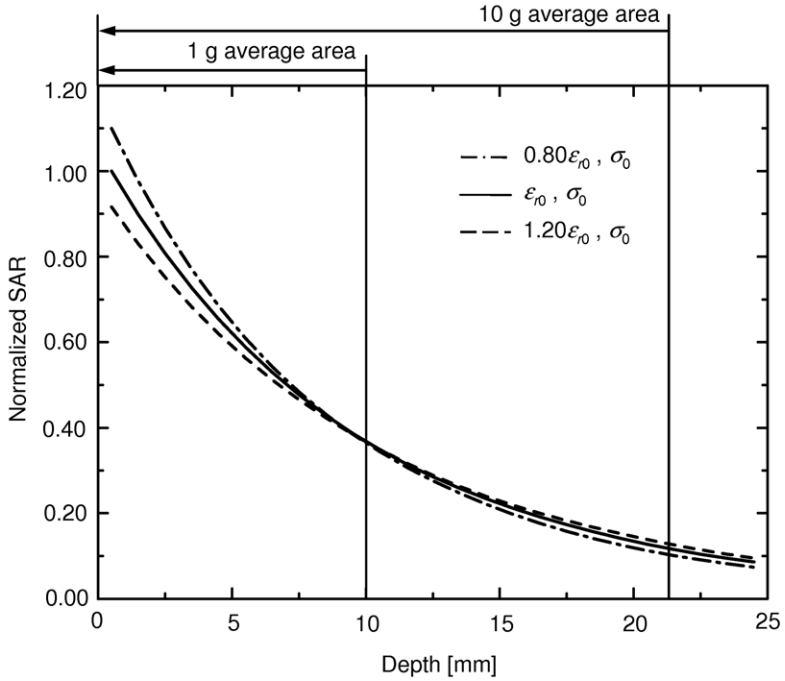

(a) Only ε_r is varied

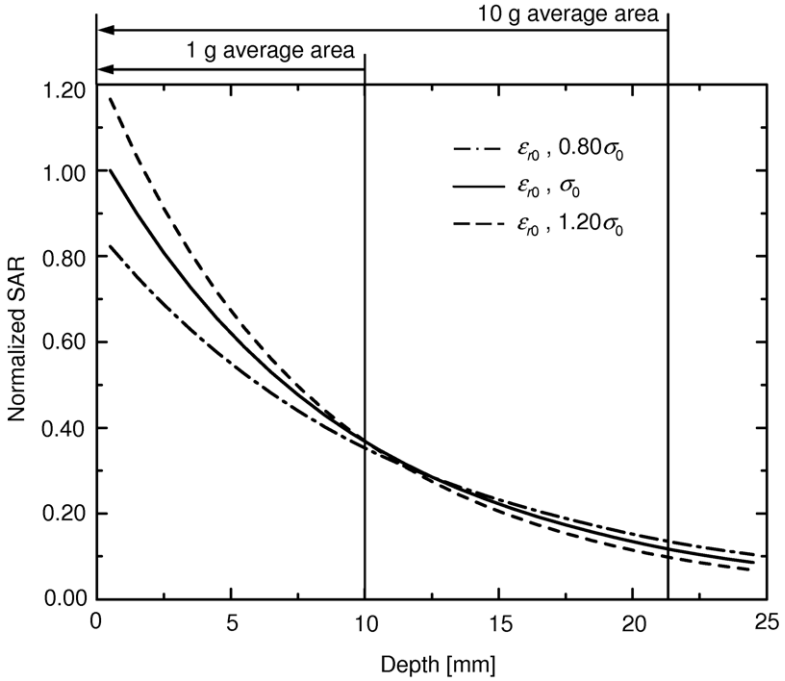

(b) Only σ is varied

Fig. 4.11 SAR distributions inside the phantom at 2 GHz.

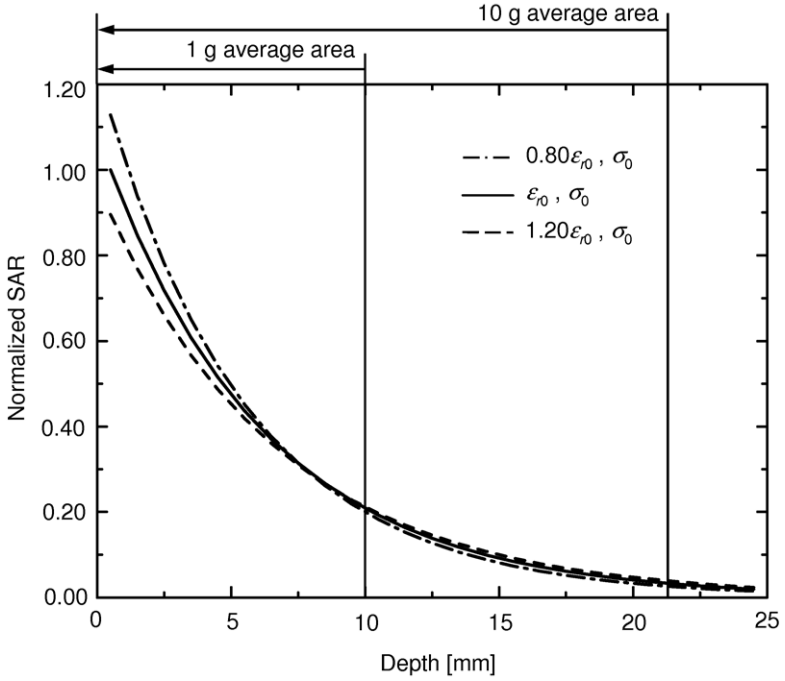

(a) Only ε_r is varied

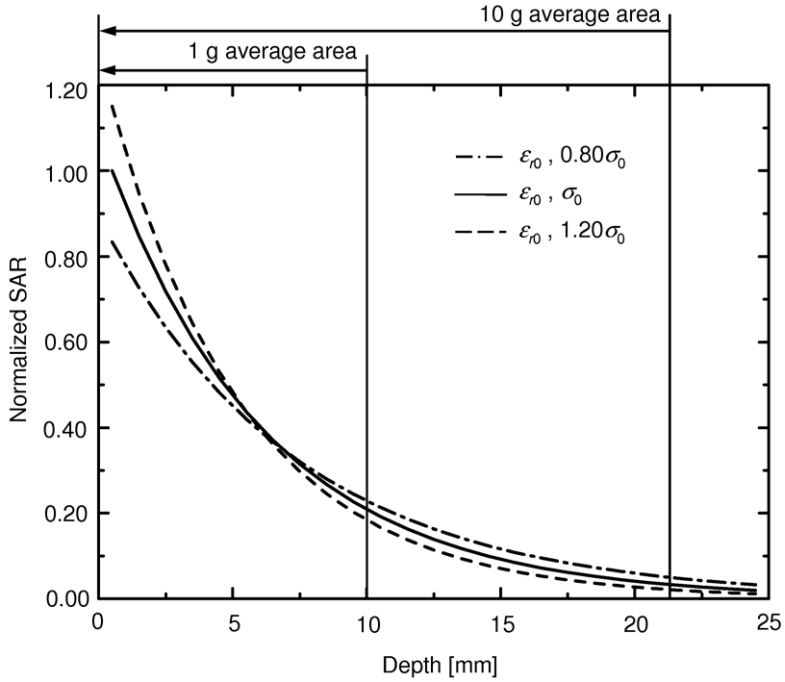

(b) Only σ is varied

Fig. 4.12 SAR distributions inside the phantom at 3 GHz.

4.4.2 Variation in the attenuation of the SAR

The variation in the attenuation of the SAR distribution is due to the change in the attenuation constant of the phantom. The attenuation constant is dependent on the dielectric constants of the phantom well as known [48], [49]. In the plane waves exposure, the attenuation constant α is given by

$$\alpha = \omega \left[\frac{\mu_0 \varepsilon_0 \varepsilon_r}{2} \left\{ \sqrt{1 + \left(\frac{\sigma}{\omega \varepsilon_0 \varepsilon_r} \right)^2} - 1 \right\} \right]^{1/2} \tag{4.1}$$

where α is the attenuation constant [Np/m], μ_0 is the permeability in the vacuum [H/m], ω is the angular frequency [rad/s].

However, it is difficult to discuss about the variation in the SAR distribution using the α. Therefore, this section uses the penetration depth of the phantom. Actually, the penetration depth of the phantom is different from a conductor because the phantom is a dielectric. In addition, the penetration depth is due to the radiation devices. Nevertheless, the variation in the SAR distribution may be assumed using the penetration depth. Here, the penetration depth d_s [mm] is given by $d_s = \alpha^{-1}$.

Figure 4.13 shows the variation in the d_s when the $\varepsilon_r/\varepsilon_{r0}$ or σ/σ_0 is changed at 0.8 to 1.2 under the condition that the other is the unity at 150 MHz to 3 GHz. Here, it is confirmed that the attenuation of the penetration depth vs. frequency is almost equal to that of the $f^{-1/2}$

As shown in Fig. 4.13, the decrease in the d_s is proportional to the increase in the frequency. The result also suggests the increase in the d_s is proportional to the increase in the $\varepsilon_r/\varepsilon_{r0}$. On the other hand, the decrease in the d_s is proportional to the increase in the σ/σ_0. In addition, the dependence of the variation in the d_s on the inaccurate ε_r is smaller than that on the inaccurate σ. Furthermore, the variation in attenuation of the SAR

distribution can be assumed by the result in Fig. 4.13.

From Fig. 4.13, the change in the d_s is almost equal to 68–95 at 150 MHz. Thus, the attenuation of the SAR distribution is hardly due to the inaccurate ε_r or σ at 150 MHz, as given by Fig. 4.9. In addition, the variation in the d_s is hardly dependent on the inaccuracy of the ε_r at 2 and 3 GHz as shown in Fig. 4.13 (b). Therefore, the change in the average SARs is almost dependent on the variation in the SAR distribution around the surface at these frequencies.

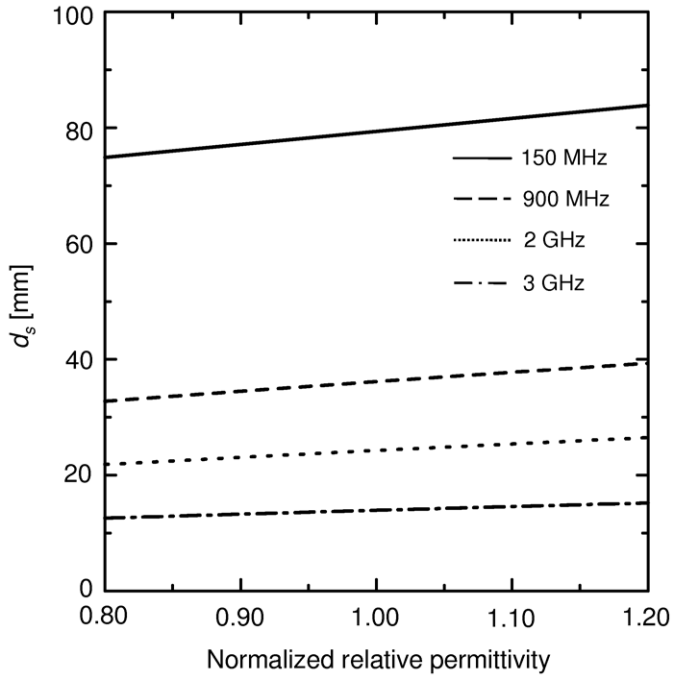

(a) Only ε_r is varied

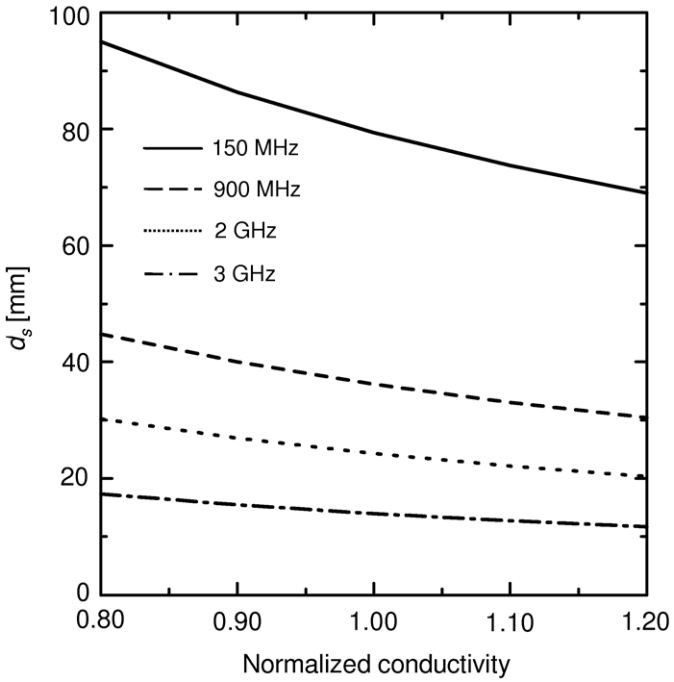

(b) Only σ is varied

Fig. 4.13 Effect of the inaccurate relative permittivity or conductivity on the d_s.

4.5 Relationship between the relative permittivity and the peak SAR

It is clear that the SAR is proportional to the conductivity σ, as expressed by Eq. (2.1). On the other hand, the relative permittivity ε_r is not included in Eq. (2.1). However, the SAR has been varied by the inaccurate ε_r in Sections 4.3 and 4.4. The variation in the local average SARs is due to the change in the SAR distribution, which is caused by the inaccurate dielectric constants, as shown in Section 4.4. Therefore, in this Section, I discuss about the relationship between the peak SAR and the ε_r.

As shown in Eq. (2.1), the σ and the density ρ is the constant of the phantom. Thus, the variation in the SAR is due to the change in the E, which is caused by the inaccurate ε_r. Figure 4.14 shows the calculation result of ${E_z}^2$ distribution inside the phantom, when the $\varepsilon_r/\varepsilon_{r0}$ or σ/σ_0 is changed at 1.0 and 1.2 under the condition that the other is the unity at 900 MHz and 3 GHz.

From Fig. 4.14, the maximum variation in the ${E_z}^2$ caused by the change in the ε_r at 3 GHz is larger than that at 900 MHz. This result is almost same as the variation in the peak SAR, as given by Fig. 4.2 (a). On the other hand, the maximum variation in the ${E_z}^2$ caused by the change in σ at 3 GHz is slightly larger than that at 900 MHz. Therefore, the variation in the peak SAR caused by the inaccuracy of σ is hardly due to the frequency such as shown in Fig. 4.2 (b). From this result, it is confirmed that only the effect of inaccurate ε_r on the ${E_z}^2$ is dependent on the frequency.

The decrease in the peak SAR is proportional to the increase in the ε_r was already proposed in Section 4.3. This relationship may be due to the variation in the electric displacement caused by the change in the ε_r. On the other hand, variation in the peak SAR caused by frequency is produced by various factors; e.g., variation in the E-field distribution

on the phantom surface caused by the shorten of the antenna, shorten of the wavelength, shorten of the internal wavelength of the phantom, change in the surface impedance of the phantom, etc. It is assumed that the variation of the peak SAR is mainly produced by the change in the E-field distribution which is caused by the shorten of the antenna because the E-field distribution on the phantom surface concentrates the point at 3 GHz. The investigation of the variation in the E-field distribution around the phantom surface in various cases is necessary to confirm the validity of this assumability.

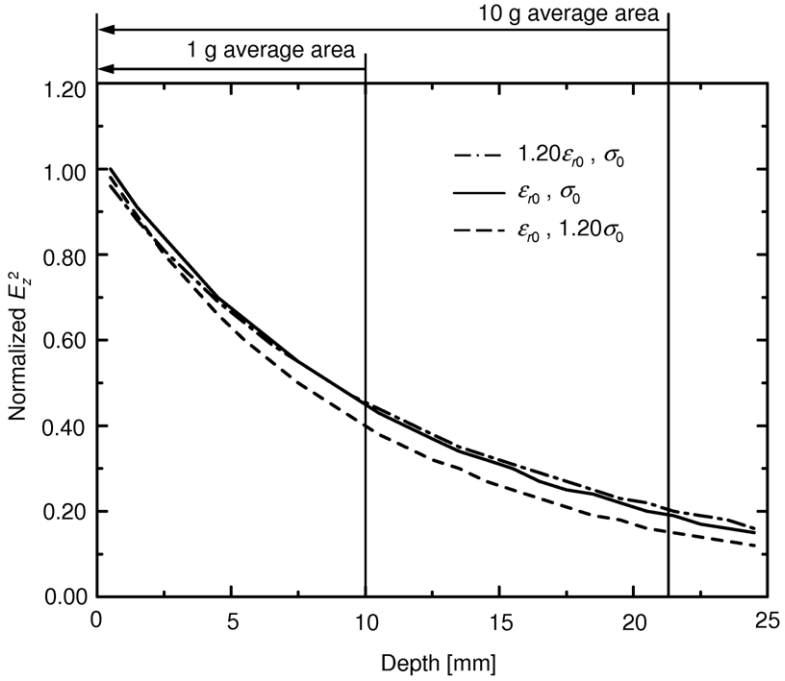

(a) 900 MHz

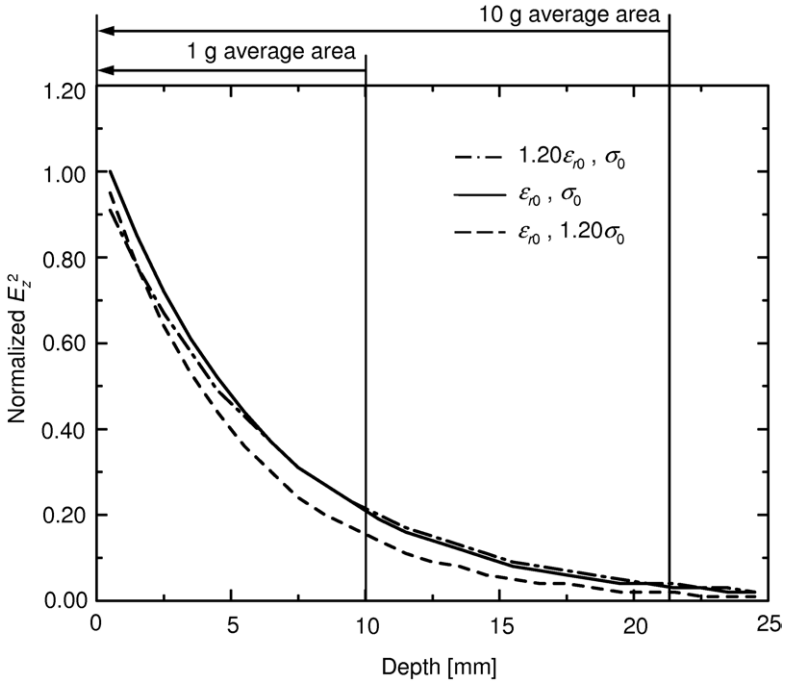

(b) 3 GHz

Fig. 4.14 Effect of the inaccurate relative permittivity or conductivity on the $E_z{}^2$ distribution inside the phantom.

4.6 Effect of the shape of the phantom

In Section 4.2 to 4.5, the COST244 cubic model is used as the human head. However, the real human head is composed by a curved and flat surface. Therefore, the investigation of the effect of the shape on the variation in the SAR, which is caused by the inaccurate dielectric constants, is important. In this Section, I calculate the effect of the inaccurate dielectric constants on the local SARs in the realistic and COST244 cubic models at 2 GHz.

4.6.1 Models and criteria

Figures 4.15 (a) and (b) show the basic model for calculations. Figure 4.15 (a) represents a half-wave dipole antenna and a realistic head model [45]. On the other hand, Fig. 4.15 (b) describes the antenna and a COST244 spherical model. The radius of the sphere is 100 mm. In addition, the distance between the feed point of the antenna and the phantom surface is 15 mm to realize the actual situation. The characteristics of the head models are as follows: the electrical properties at 2 GHz are $\varepsilon_r = \varepsilon_{r0} = 40.0$, $\sigma = \sigma_0 = 1.40$ S/m, the density $\rho =$ 1,000 kg/m^3 [12]. From now on, ε_{r0} and σ_0 are used as reference values for the inaccuracy of dielectric constants.

Table 4.2 describes the reference value of the local SARs in each model. In addition, the local SARs are normalized to these values. Moreover, these values are normalized to the 1 W output of the antenna.

Table 4.2 Criteria of local SARs in three types of models

Shape	Peak SAR [W/kg]	$SAR_{1\,g}$ [W/kg]	$SAR_{10\,g}$ [W/kg]
Cube	33.3	19.5	10.6
Real	31.5	19.1	10.8
Sphere	26.9	16.5	9.41

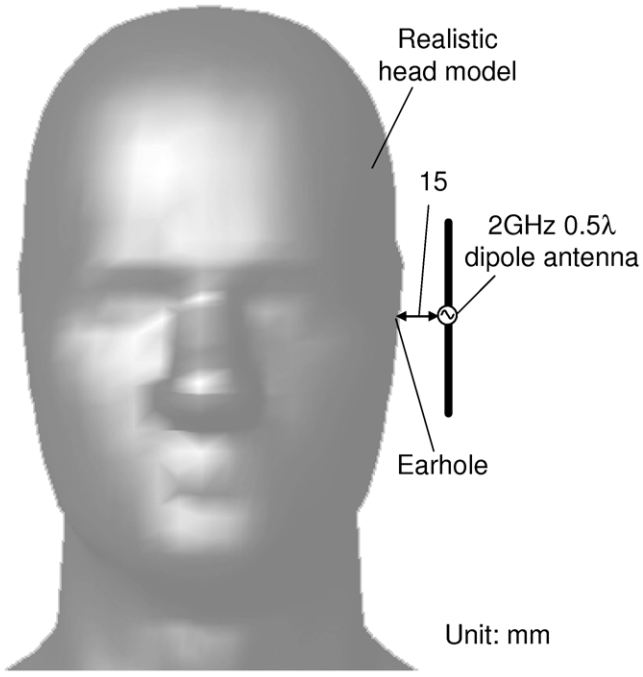

(a) Realistic model

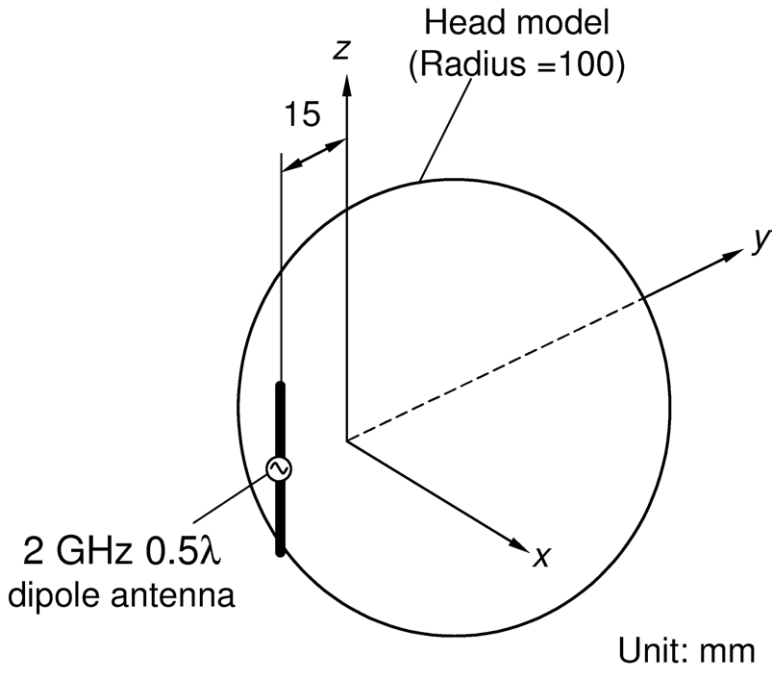

(b) Spherical model

Fig. 4.15 Models for calculations.

4.6.2 Effect of the variation in the relative permittivity or the conductivity

This Section suggests the dependence of the variation in the local SARs on the phantom shape when the only relative permittivity ε_r or conductivity σ is changed.

Figures 4.16 to 4.18 show the calculated results of the normalized local SARs, when the normalized electric constant of three types of models [see Figs. 4.1 (b) and 4.15], $\varepsilon_r/\varepsilon_{r0}$ or σ/σ_0 is varied from 0.8 to 1.2 under the condition that the other is the unity at 2 GHz. From now on, the local SARs were normalized to the referenced values in Tables 4.1 and 4.2.

As shown in Fig. 4.16 (a), the effect of the variation in the $\varepsilon_r/\varepsilon_{r0}$ on the peak SAR of the spherical model is larger than that of the others. On the other hand, the effect of the change in the σ/σ_0 is hardly due to the shape as given by Fig. 4.16 (b). Therefore, the variation in the shape causes only the effect of the inaccurate ε_r on the peak SAR. From these results, the effect of the variation in the peak SAR is less than 3% when $\varepsilon_r/\varepsilon_{r0}$ or σ/σ_0 is varied from 0.8 to 1.2.

From Fig. 4.17 (a), the effect of the variation in the $\varepsilon_r/\varepsilon_{r0}$ on the 1 g average SAR of the realistic and spherical model is larger than that of the cubic one. Therefore, the dependence of the 1 g average SAR on the inaccurate ε_r is due to the variation in the E-field distribution caused by the curvature of the model. On the other hand, the effect of the variation in the σ on the 1 g average SAR of the realistic model is slightly larger than that of the others as shown in Fig. 4.17 (b). These results also suggest the effect of the variation in the 1 g average SAR is less than 2%.

As shown in Fig. 4.18 (a), the effect of the variation in the $\varepsilon_r/\varepsilon_{r0}$ on the 1 g average SAR of the realistic and spherical model is slightly larger than that of the cubic one. On the other hand, the effect of the variation in the σ on the 10 g average SAR of the realistic model is slightly larger than that of the cubic one. In addition, the dependence of the 10 g

average SAR on the σ of the spherical model is slightly smaller than that of the cubic one as given by Fig. 4.18 (b). These results also support the effect of the variation in the 10 g average SAR is less than 1%.

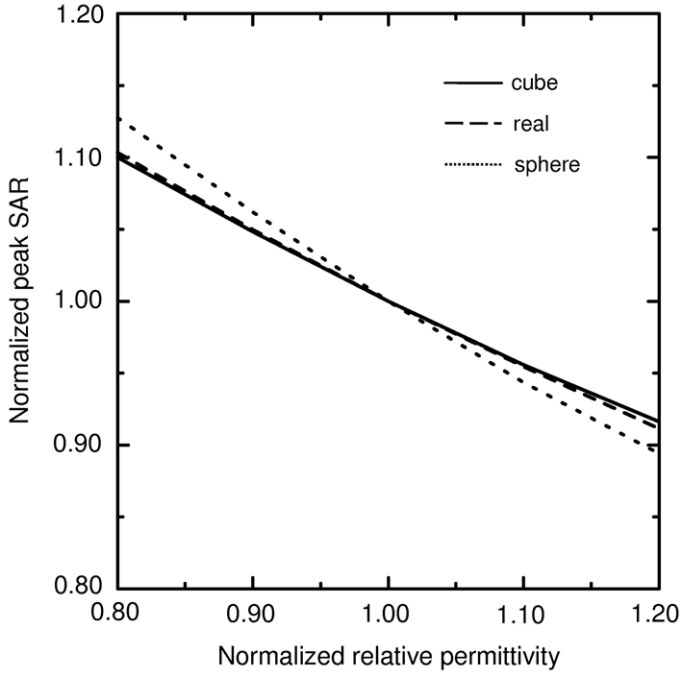

(a) Only ε_r is varied

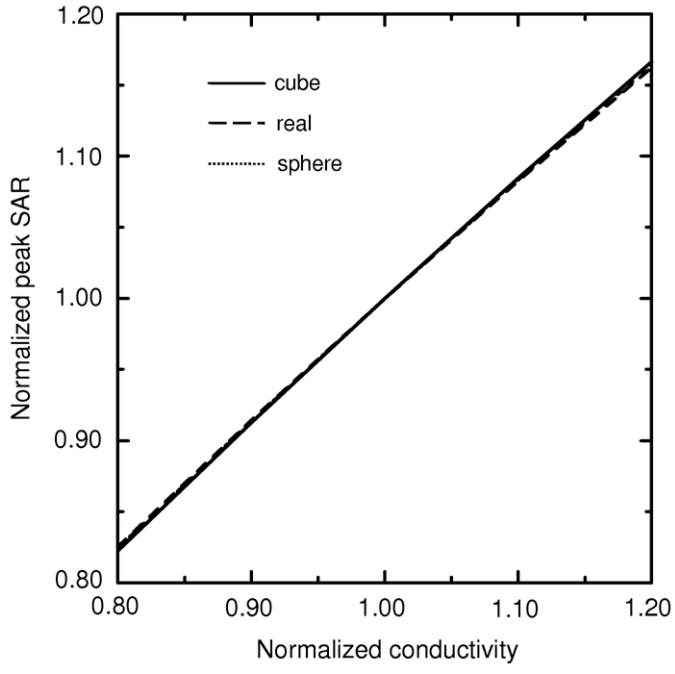

(b) Only σ is varied

Fig. 4.16 Effect of the inaccurate relative permittivity or conductivity on the peak average SAR in three types of head model.

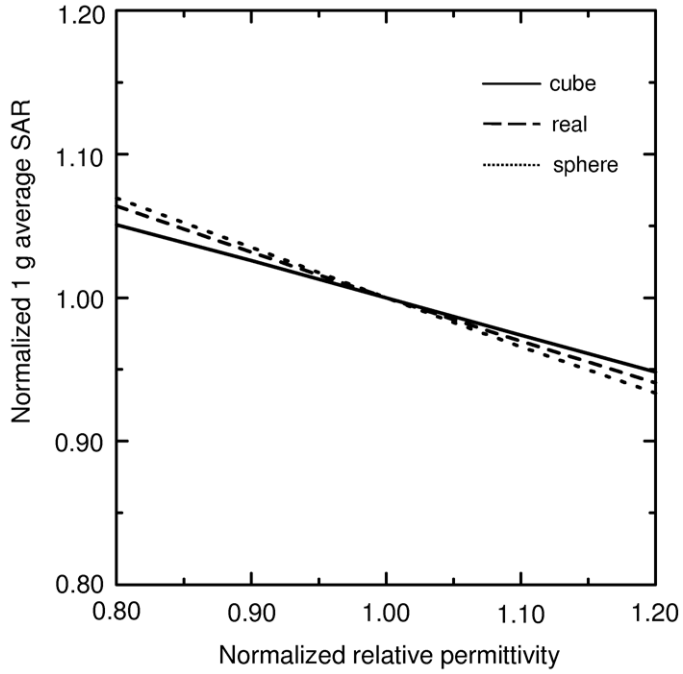

(a) Only ε_r is varied

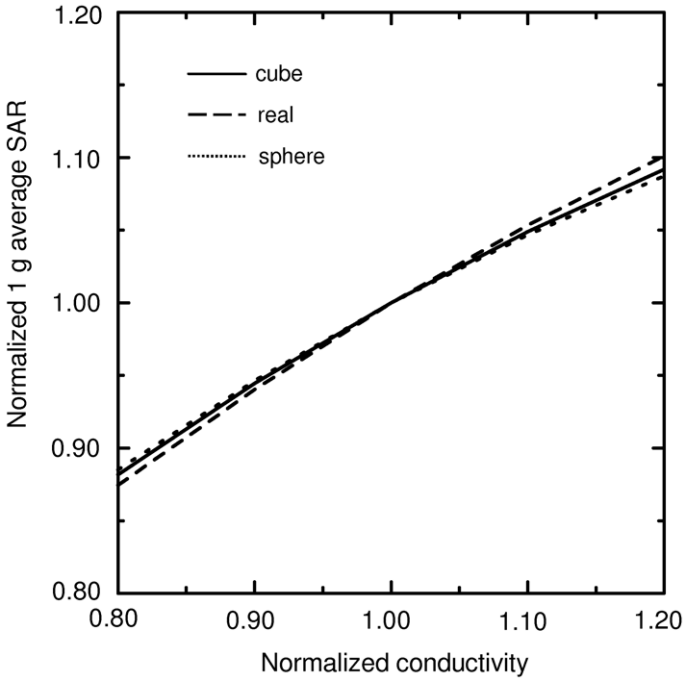

(b) Only σ is varied

Fig. 4.17 Effect of the inaccurate relative permittivity or conductivity on the 1 g average SAR in three types of head model.

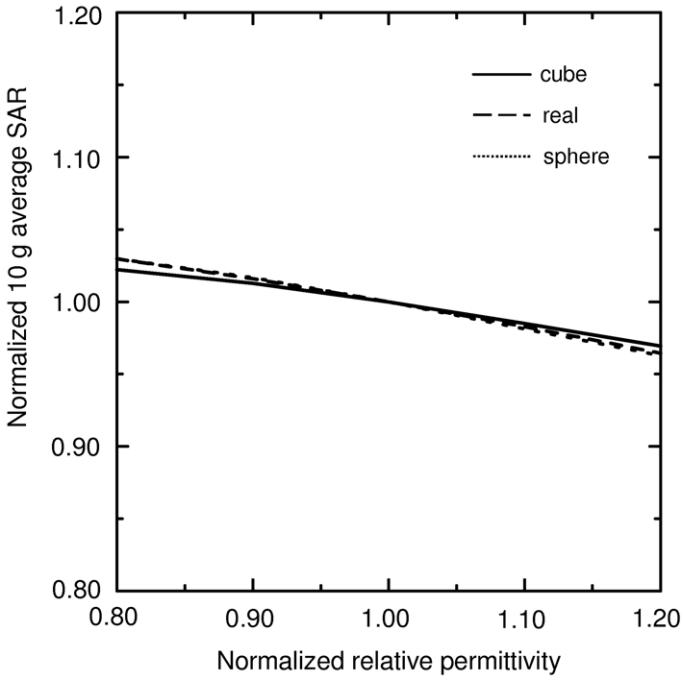

(a) Only ε_r is varied

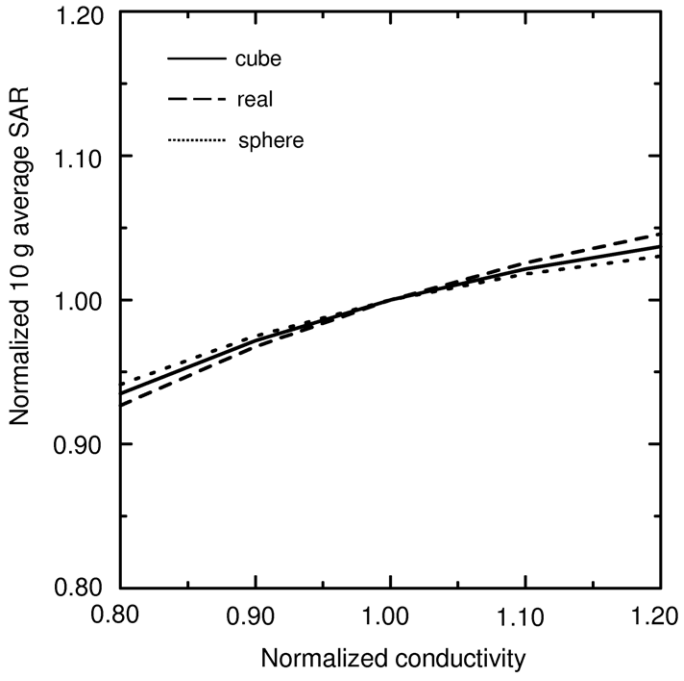

(b) Only σ is varied

Fig. 4.18 Effect of the inaccurate relative permittivity or conductivity on the 10 g average SAR in three types of head model.

4.6.3 Effect of the variation in the dielectric constants

Figures 4.19 and 4.20 show the calculated result of the normalized local 1 g and 10 g average SAR in the realistic and spherical models using a contour line when the $\varepsilon_r/\varepsilon_{r0}$ and σ/σ_0, are simultaneously varied from 0.8 to 1.2 at 2 GHz. The result of the cubic model is already proposed as given by Fig. 4.7.

As shown in Figs. 4.7, 4.19, and 4.20, the variation in the local average SARs of the realistic model is the largest in the models. In addition, these result also suppose the effect of the variation in the average SARs is less than 3%. From these results, the dependence of the change in the average SAR on the inaccurate dielectric constants is slightly due to the shape.

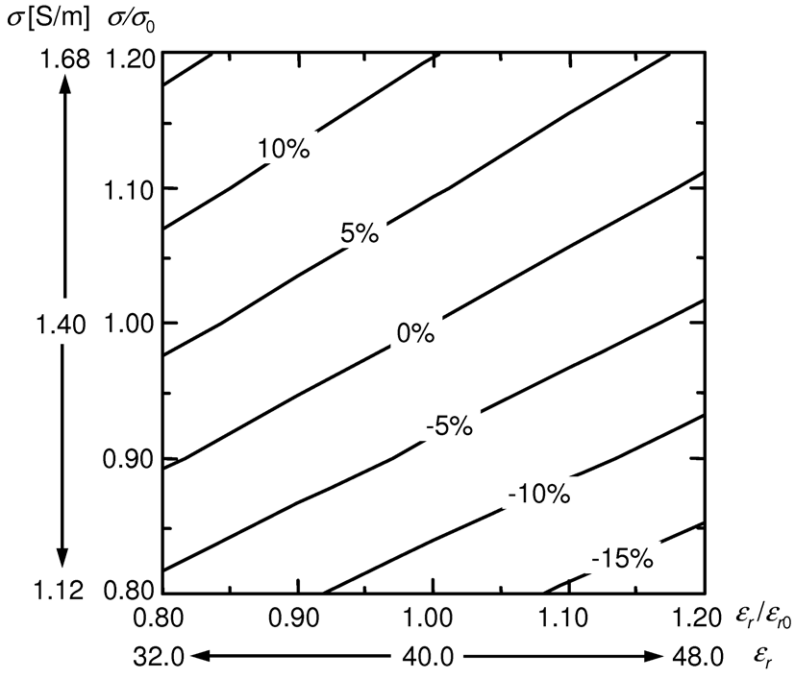

(a) 1 g average SAR

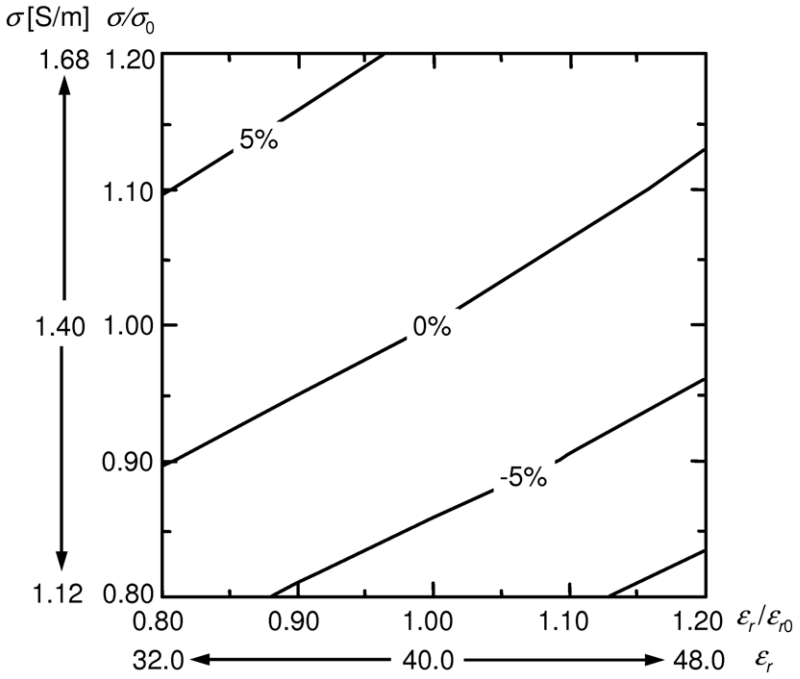

(b) 10 g average SAR

Fig. 4.19 Effect of the inaccurate dielectric constants on the local average SARs in the real head model (contour).

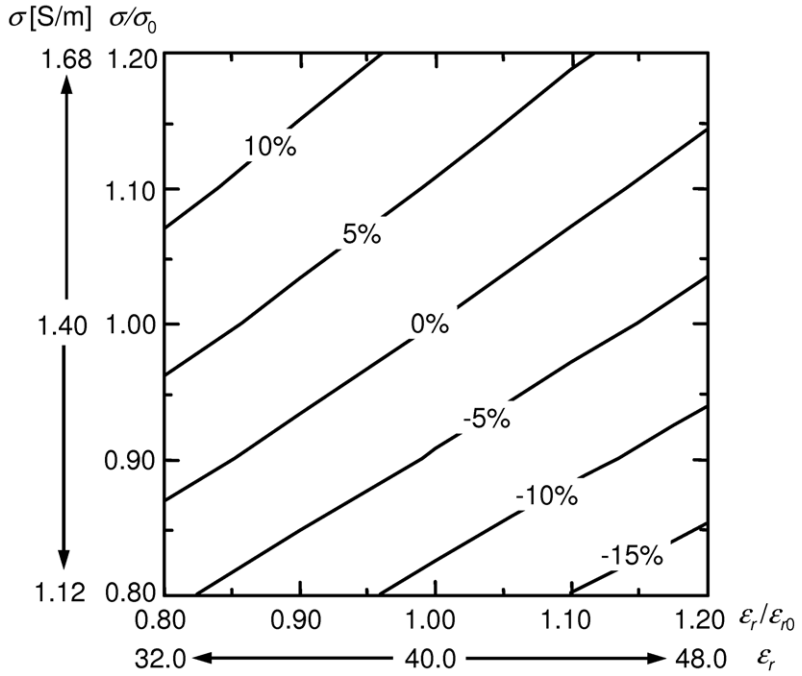

(a) 1 g average SAR

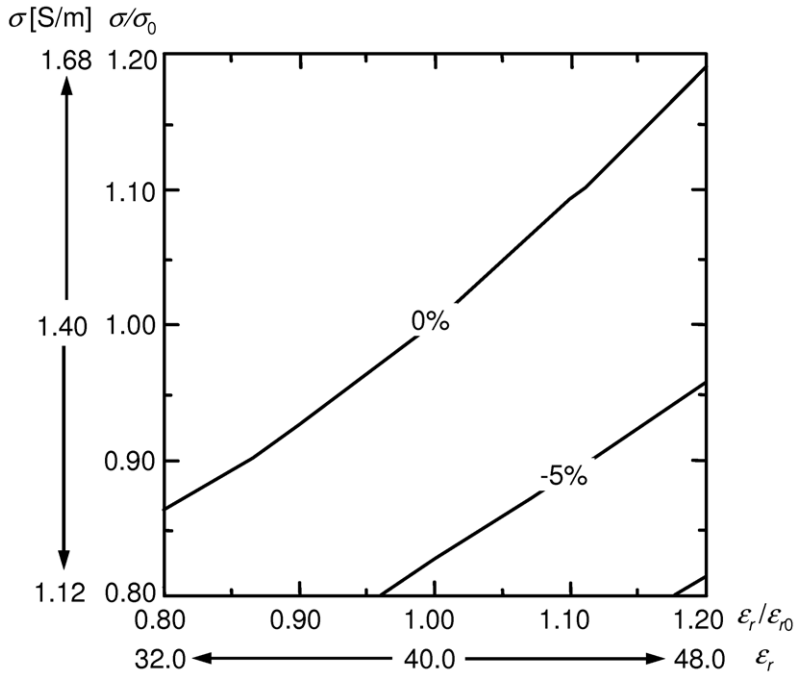

(b) 10 g average SAR

Fig. 4.20 Effect of the inaccurate dielectric constants on the local average SARs in the spherical model (contour).

4.7 Corrective method of the error of the SAR by the inaccuracy of dielectric constants

The error of the local SAR caused by the inaccurate dielectric constants of the biological tissue-equivalent phantom can be corrected using the proposed results in Section 4.3. Therefore, the regular measurement of the inaccuracy of the dielectric constants of the phantom using such as the dielectric probe measurement system is very important to realize the precision evaluation of the SAR. However, the evaluation of the dielectric constants is difficult when the actual measurement of the SAR; e.g., evaluation of the many devices, using the large model, etc. In these cases, the corrective method of the SAR is as follows:

1) investigation of the measurement time and condition of the room.

2) leave the phantom, which has same volume of the measurement, in the same condition of the SAR estimation at the same time.

3) measurement of the dielectric constants after 1).

4) calculation of the variation in the dielectric constants at the unit time.

5) correction of the SAR using the result of 3) at optional time.

4.8 Conclusions

This Chapter presented the investigation of the effect of the inaccurate dielectric constants of the biological tissue-equivalent phantom on the local SARs in the human model when the dielectric constants are varied at 150 MHz, 900 MHz, 2 GHz, and 3 GHz. The important findings in this Chapter are as follows;

1) Local peak, 1 g and 10 g average SARs in the human model were calculated using the FDTD method, when the relative permittivity ε_r or conductivity σ are varied from criteria to $\pm$ 20% under the condition that the other was the unity at 150 MHz–3 GHz. As a result, it has been confirmed the decrease in the local SARs is proportional to the increase in the ε_r. On the other hand, the increase in the local SARs is proportional to the increase in the σ. Moreover, the dependence of the local SARs on the inaccurate ε_r or σ is due to the frequency. However, the variation in the peak SAR is hardly due to the frequency.

2) Local 1 g and 10 g average SAR were evaluated when the ε_r and σ were simultaneously varied from criteria to $\pm$ 20% at 150 MHz–3 GHz. As a consequence, I have confirmed that the effect of the inaccurate dielectric constants on the local average SARs is almost equal to the sum of the change in the SAR caused by the inaccurate $\varepsilon_r$and that by the σ as given by 1). In addition, the variation in the local average SARs is dependent on the frequency.

3) The effect of the shape on the variation in the local SARs of three types of models caused by the inaccurate dielectric constants was investigated at 2 GHz. As a result, it has been confirmed that the effect of the variation in the average SARs is less than 3%. In addition, the dependence of the change in the average SAR on the inaccurate dielectric constants is slightly due to the curvature of the shape.

Chapter 5 Modeling of a simple abdomen model of pregnant women

5.1 Introduction

Recently, RF devices, which are usually placed in the vicinity of the human body, have been widely used. Pregnant women and their fetuses may be exposed to the EM waves radiated from these devices, e.g., portable radio terminals, induction heating cookers, hand-held metal detectors, etc. It is therefore necessary to evaluate the EM exposure of the fetus inside pregnant women.

To the author's knowledge, several papers on the evaluation of the EM exposure in the fetus have been published [50], [51]. In the papers, the abdomen of pregnant women is replaced as the simple models. For example, Figs. 5.1 (a) and (b) illustrate the abdomen models of pregnant women in the previous studies. Figure 5.1 (a) describes the homogeneous and layered spherical models replace the pregnant women to evaluate the SAR generated by the plane waves' exposure at 300–1500 MHz [50]. On the other hand, the model simulates a external structure of a pregnant woman in the 34th weeks pregnancy as given by Fig. 5.1 (b) to calculate the induced current densities and the SAR which is produced by a hand-held metal detectors (HHMDs) [51]. However, as shown in Fig. 5.1, the structure inside the model is inaccurate because the magnetic resonance imaging (MRI) tomograms of the pregnant women are hard to obtain. In addition, little is known about the dielectric constants of the amniotic fluid and fetus. Therefore, an accurate structure of the model and the dielectric constants of

the fetus are indispensable to evaluate the precision EM exposure in the fetus.

This Chapter proposes the modeling of the abdomen of pregnant women. First, in Section 5.2, the dielectric constants of the amniotic fluid and fetus of the rabbit are measured because the electrical properties of mammals are almost equal to those of the human [52]. In addition, the dielectric constants of internal organs of the rabbit are also measured. Next, in Section 5.3, a simple abdomen model of the pregnant women, which is composed by three types of tissues (body, amniotic fluid, fetus), based on measurements of MRI tomograms is introduced. Finally, in Section 5.4, an simple abdomen solid phantom of the pregnant women, which is used as the measurement, is presented.

The study in Chapters 5 and 6 is the joint research with Research Center for Frontier Medical Engineering in Chiba University, Graduate School of Medicine in Chiba University, Chiba University Hospital, Panasonic Mobile Communications Co., Ltd., and Matsushita Electric Industrial Co., Ltd.

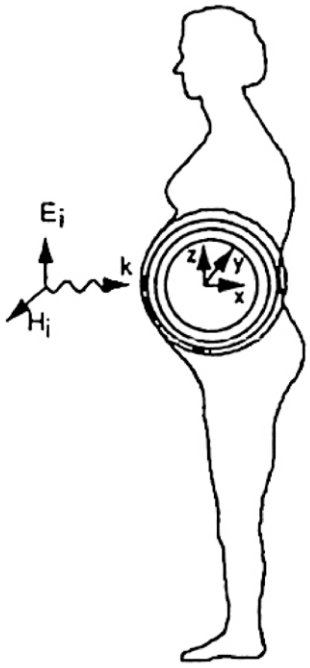

(a) Fleming's model [50]

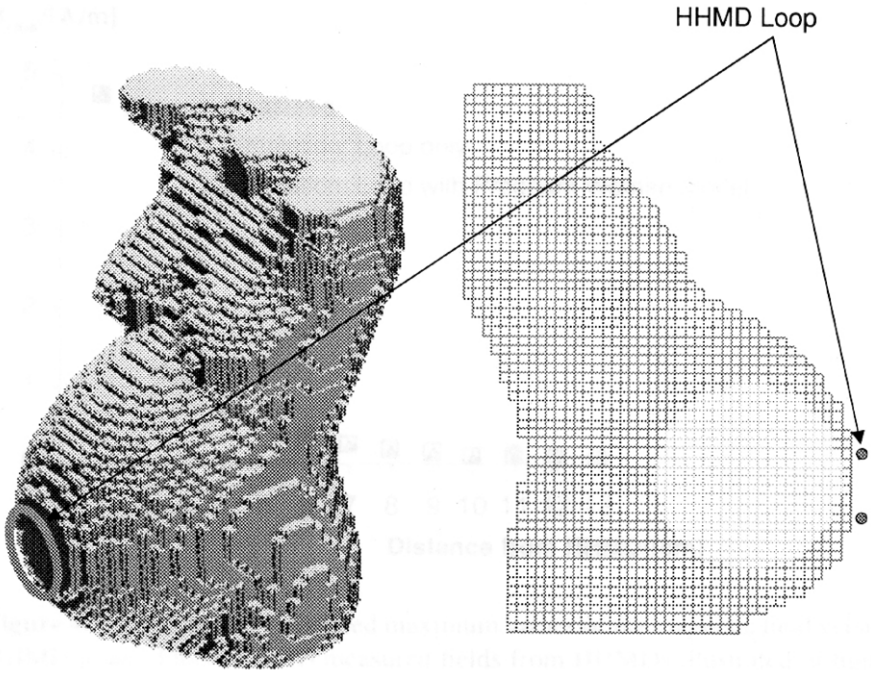

(b) Kainz's model [51]

Fig. 5.1 Instance of the numerical models of pregnant women.

5.2 Measurement of the electric constants of internal organs of a rabbit

5.2.1 Condition and setting

In the measurement of the dielectric constants, a Japanese White rabbit of twenty five days of pregnancy and eight fetuses of the rabbit are used. Figure 5.2 shows the measurement rabbit because the measurement of the dielectric constants of the amniotic fluid and the fetus is difficult in early pregnancy. Here, the pregnancy of the rabbit is almost equal to eight to nine months of pregnancy for the human. In addition, the amount of the amniotic fluid is the maximum in this pregnancy.

In the euthanasia of rabbits, a pentobarbital sodium solution is used. The euthanasia and dissection of the rabbit were realized following a guideline of experiments on animals of Chiba University in Inohana area.

The measurement instrument of the dielectric constants is an HP-85070M dielectric-probe measurement system manufactured by the Agilent Technology Co. Ltd., Tokyo, Japan. The temperature in the measurement room is 22 °C. In addition, the humidity of the room is 32%. The temperature of the internal organs is 22–24 ° C.

Fig. 5.2 A rabbit by use of measurement (twenty-five days of pregnancy).

5.2.2 Results

Internal organs

Figures 5.3–5.6 illustrates the measured dielectric constants of the uterus, liver, muscle, and brain of the rabbit at 100 MHz to 3 GHz because the position of the uterus, liver, and muscle is close to the amniotic fluid and fetus. On the other hand, the value of the brain is usually used as the value of the human head. In addition, the reference value of the human is usually used as the value of the human tissue [52].

As shown in Figs. 5.3–5.6, the dielectric constants of the tissues vs. the frequency fit those of the human below 2 GHz. On the other hand, the differences between the two are obtained at 2–3 GHz because the result includes the error caused by the measurement system above 2 GHz. From Fig. 5.5, the different of the conductivity of the muscle is the largest in the tissues because the measurement deviation of the muscle is caused by the difference of the fiber direction.

From these results, I have confirmed that the electrical properties of this rabbit are almost equal to those of the human.

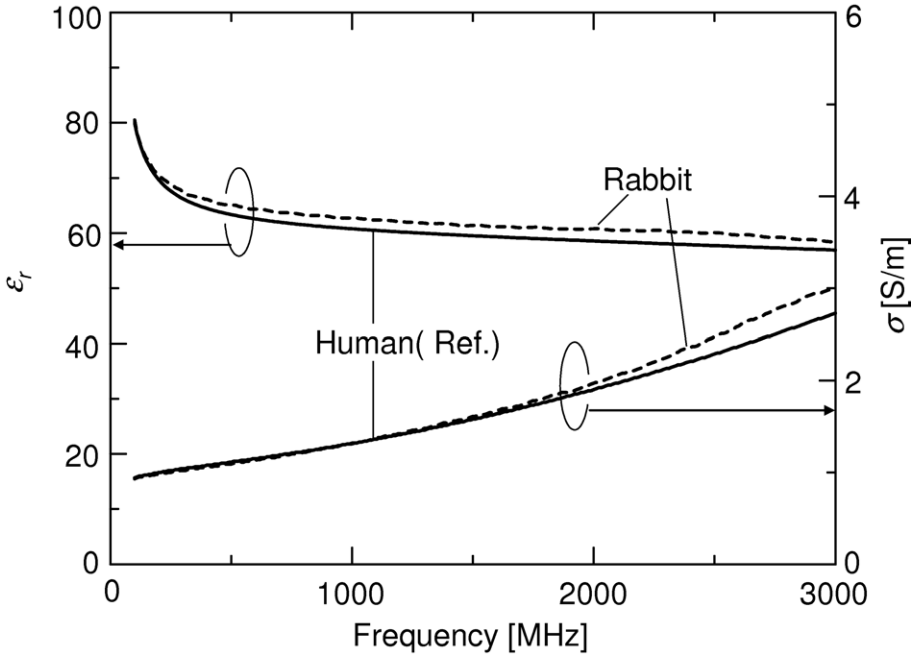

Fig. 5.3 Measured dielectric constants of the uterus of a rabbit.

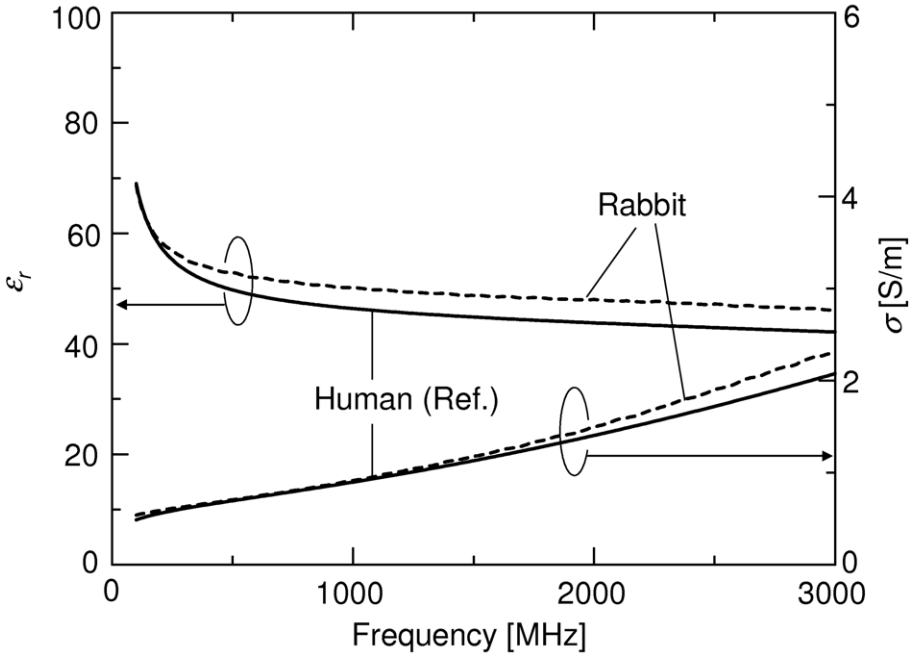

Fig. 5.4 Measured dielectric constants of the liver of a rabbit.

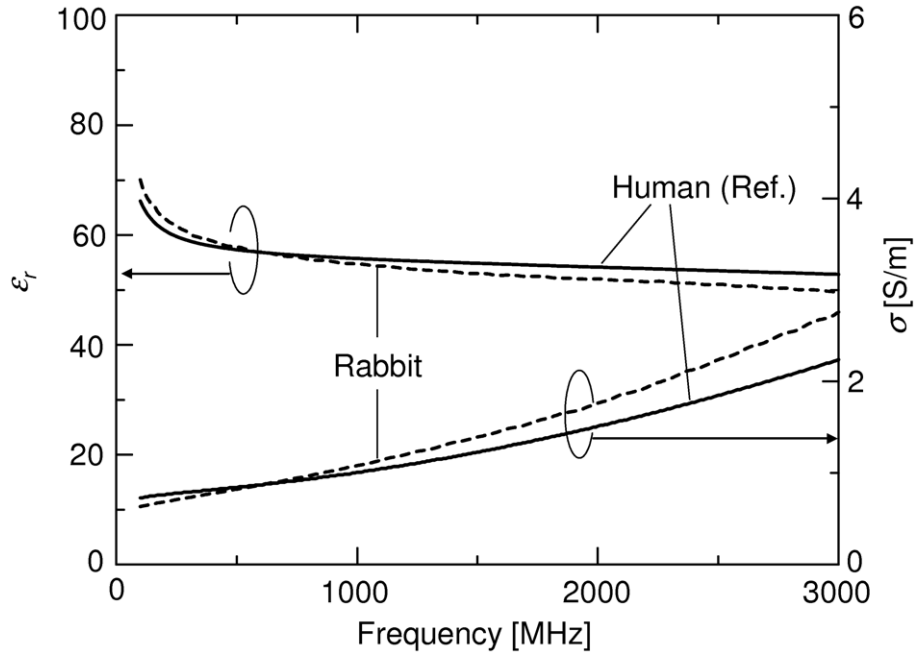

Fig. 5.5 Measured dielectric constants of the muscle of a rabbit.

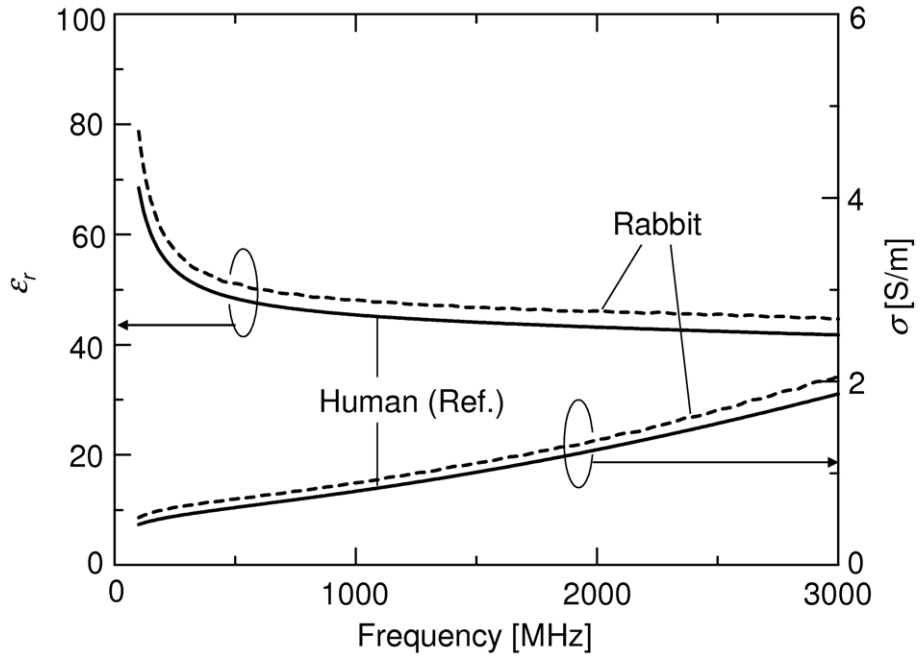

Fig. 5.6 Measured dielectric constants of the brain of a rabbit.

Amniotic fluid and fetus

Figure 5.7 shows measured dielectric constants of the amniotic fluid of a human and the rabbit at 100 MHz to 3 GHz. Here, the amniotic fluid of the human has been received from a healthy volunteer. Figure 5.8 describes the measured dielectric constants of the fetus of the rabbit. The value of the fetus of the rabbit is averaged by the value of eight fetuses.

As shown in Fig 5.7, the dielectric constants of the amniotic fluid of the rabbit fit those of the human. On the other hand, the conductivity of the fetus of the rabbit is 1.3 times larger than that of the muscle of the adult human, as given by Fig. 5.8. This result suggests the dielectric constants of the biological tissue is due to the age. Literature [53] proposed almost same result of the measured dielectric constants of rats.

From Figs. 5.7 and 5.8, the conductivity of the tissues is 1.8 or 1.3 times larger than that of the muscle of the adults at 150 MHz. The results suggest the modeling of the pregnant women including the amniotic fluid and the fetus is necessary.

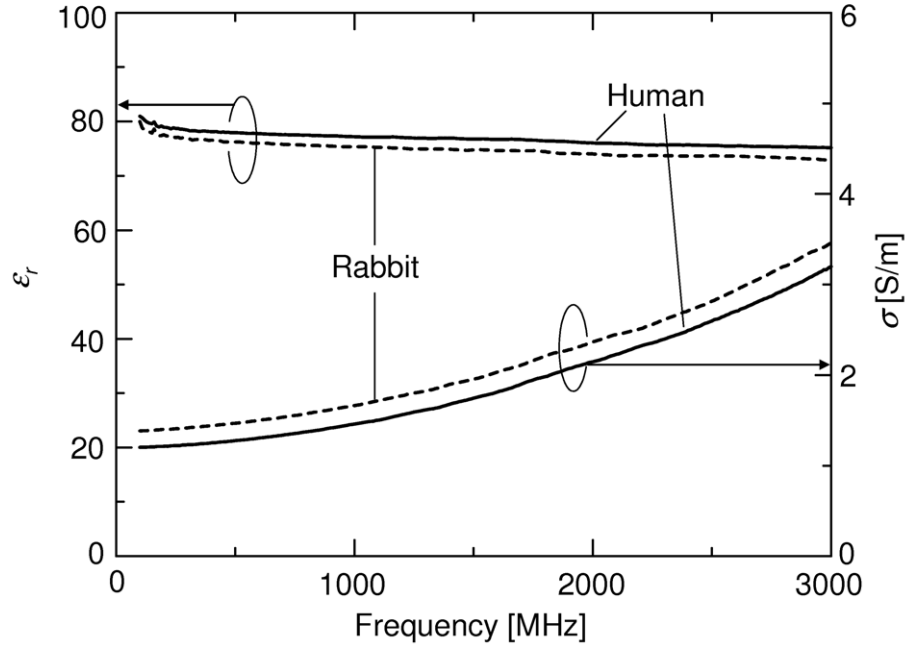

Fig. 5.7 Measured dielectric constants of the amniotic fluid of a human and a rabbit.

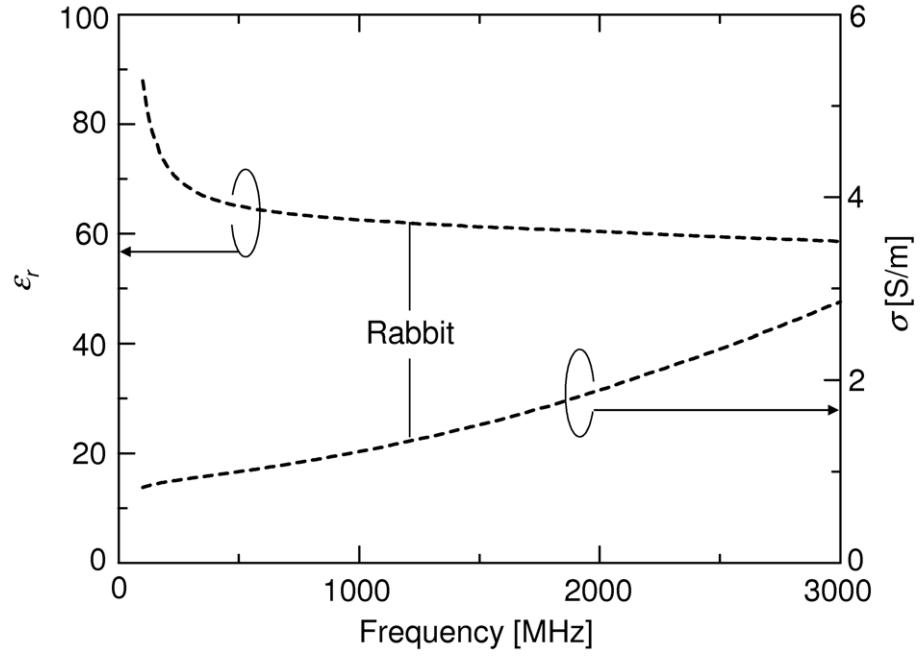

Fig. 5.8 Measured dielectric constants of the fetus of a rabbit.

5.3 Modeling of the abdomen model of pregnant women

The SAR in the fetus is dependent on the pregnant term. The external shape of pregnant women is almost equal to nonpregnant women at the early pregnancy which is less than five month of pregnancy. In addition, the measurement of the dielectric constants of the fetus at the early pregnancy is difficult. On the other hand, the work of the pregnant is difficult at the late pregnancy which is above nine month of pregnancy. Therefore, MRI tomograms of the pregnant women at the six to eight month are used.

Twenty tomograms of pregnant women are detected in Chiba University Hospital. However, the detailed modeling of pregnant women using the tomograms is difficult because the tomograms are usually taken at interval of about ten mm in order to confirm a deformed child. Here, three tomograms of the pregnant women, which has the almost same weight of average pregnant women, are used as the evaluation of the measurements of the tissue.

Figure 5.9 shows an instance of MRI tomogram of a woman at thirty weeks of pregnancy. From three tomograms such as given by Fig. 5.9, the measurements of the maximum width, height, position of the mothers' body, amniotic fluid, and fetus is evaluated. Figure 5.10 illustrates a simple abdomen model of pregnant women based on the measurements. As shown in Fig. 5.10, the amniotic fluid and fetus are modeled by ellipsoids. Here, theses ellipsoids have almost the same volume as the amniotic fluid and the fetus in Fig. 5.9. On the other hand, the mother's body is replaced by a homogeneous cylindroid.

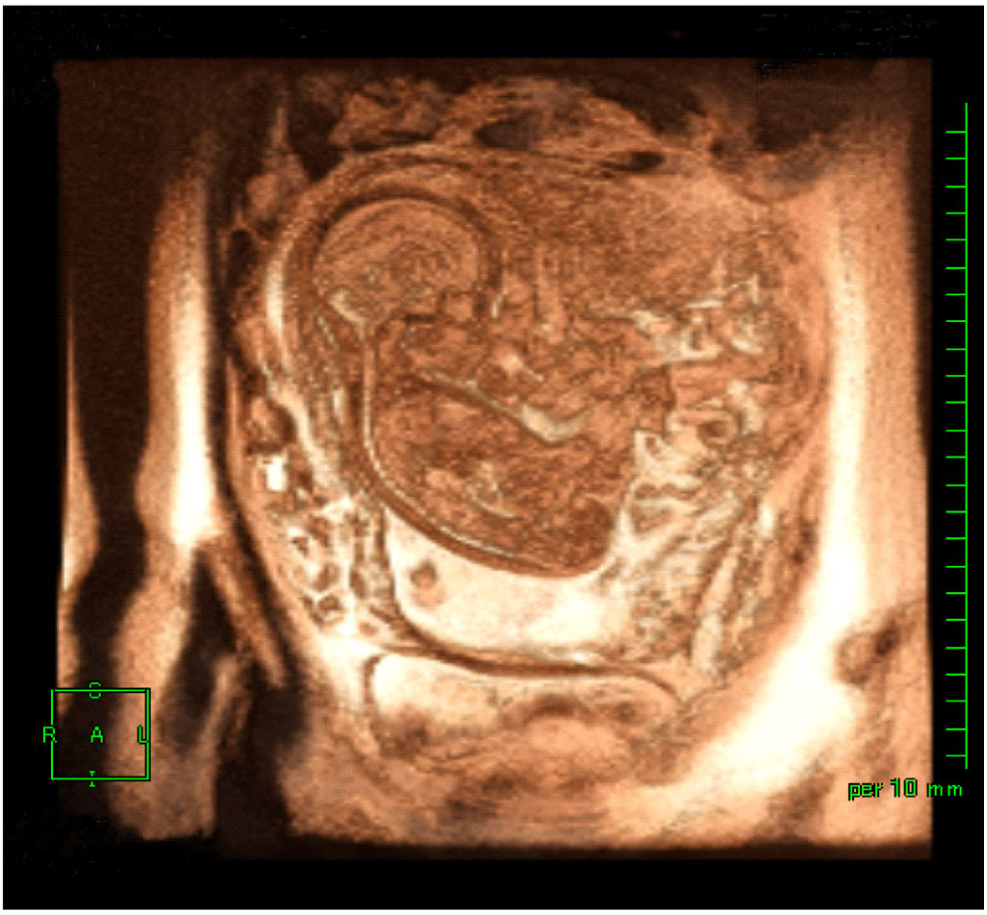

Fig. 5.9 Instance of MRI tomograms of pregnant women.

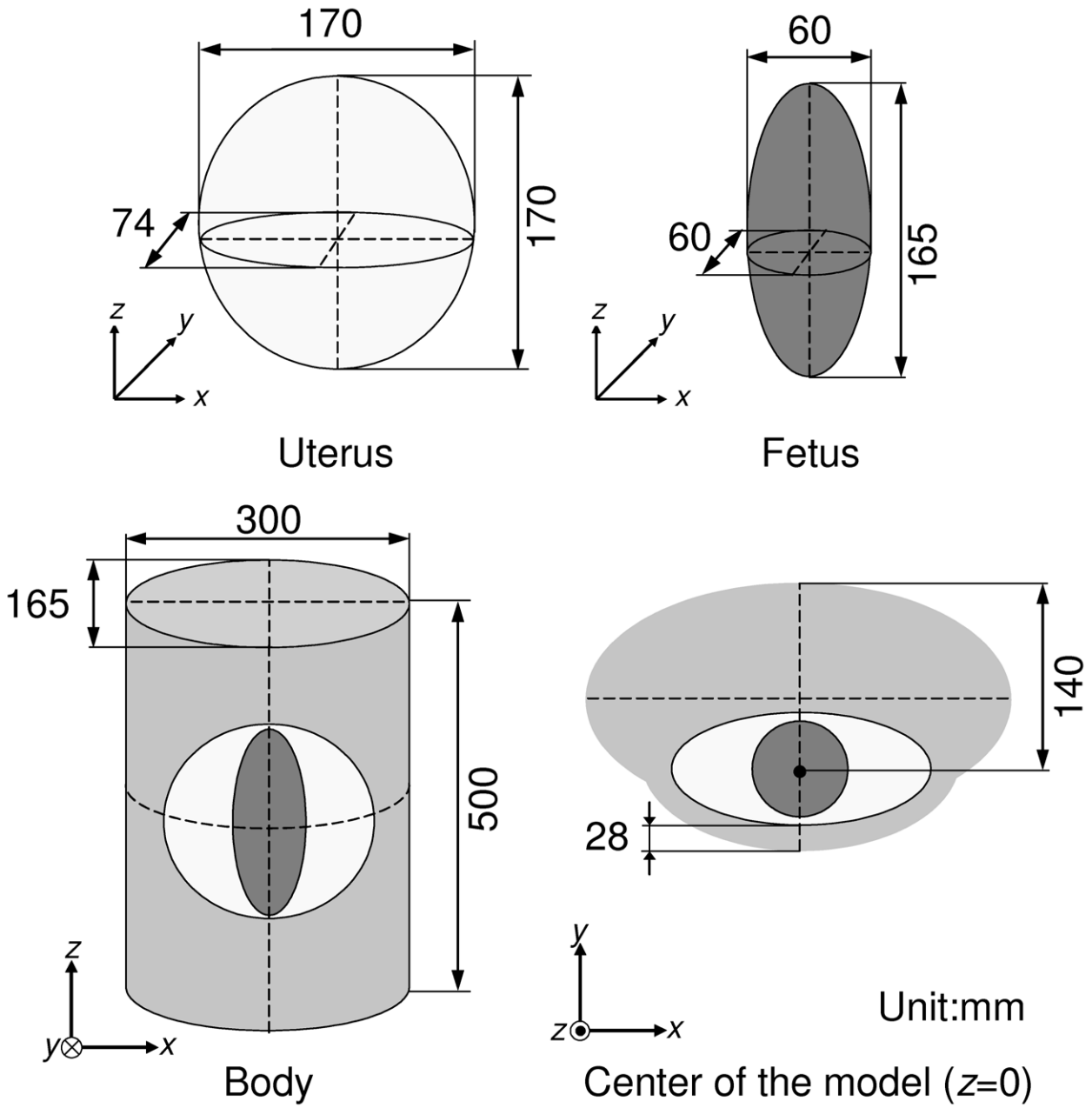

Fig. 5.10 Simple abdomen model of pregnant women.

5.4 Abdomen solid phantom of pregnant women

The decision of the ingredients of the amniotic fluid- and the fetus-equivalent phantoms is necessary to realize the layered abdomen phantom. Here, the ingredients of the body phantom are already proposed [35], [36].

Tables 5.1–5.3 describe the ingredients of the body-, amniotic fluid-, and fetus- equivalent phantoms at 150 MHz. The dielectric constants of the amniotic fluid- and fetus- equivalent phantoms are adjusted to have the same value in Figs. 5.7 and 5.8.

Figure 5.11 shows a simple abdomen phantom of the pregnant women which is composed by three types of tissues.

Table 5.1 Ingredients of the body-equivalent phantom at 150 MHz

Material	Mass [g]	Weight ratio [%]
Glycerol	1,000	32.9
Deionized water	1,500	49.3
Sodium chloride	42	1.4
Agar	100	3.3
Polyethylene powder	400	13.1

The volume of a completed phantom is approximately 4,200 cm^3.

Table 5.2 Ingredients of the amniotic fluid-equivalent phantom at 150 MHz

Material	Mass [g]	Weight ratio [%]
Deionized water	482	91.8
Sodium benzoate	18	3.4
Agar	25	4.8

The volume of a completed phantom is approximately 500 cm^3.

Table 5.3 Ingredients of the fetus equivalent phantom at 150 MHz

Material	Mass [g]	Weight ratio [%]
Deionized water	488	92.9
Sodium benzoate	12	2.3
Agar	25	4.8

The volume of a completed phantom is approximately 500 cm^3.

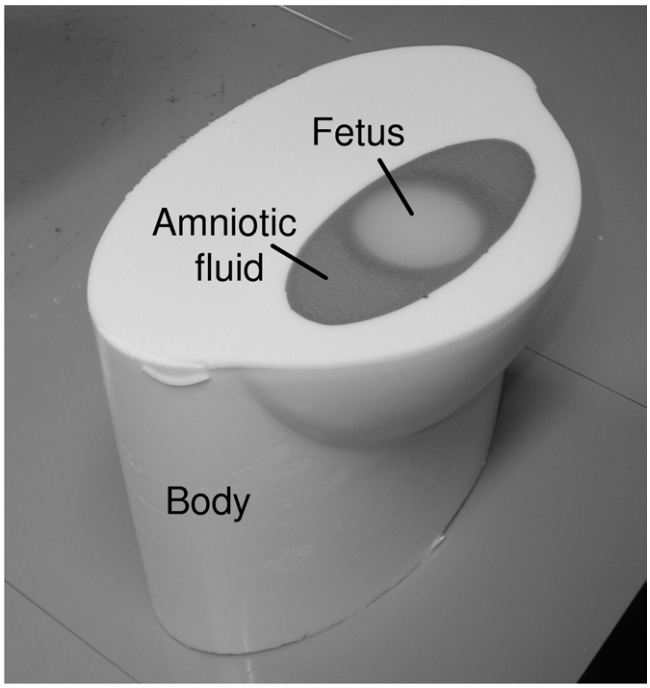

Fig. 5.11 Simple abdomen solid phantom of pregnant women.

5.5 Conclusions

In this Chapter, the modeling of the abdomen of pregnant women was proposed. First, the dielectric constants of the amniotic fluid and fetus of the rabbit were measured, because the electrical properties of mammals are almost equal to those of the human. As a result, the conductivity of the tissues was 1.8 or 1.3 times larger than that of the muscle of adults at 150 MHz. The results have suggested the modeling of the pregnant women including the amniotic fluid and the fetus is necessary. In addition, the dielectric constants of internal organs of the rabbit were also measured. As a consequence, I have confirmed that the electrical properties of measured rabbit is almost equal to those of the human. Next, the simple abdomen model of the pregnant women, which is composed by three types of tissues (body, amniotic fluid, fetus), based on measurements of the MRI tomograms was introduced. Finally, the simple abdomen solid phantom of the pregnant women, which is used as the measurement, was presented.

The evaluation of the SAR inside the proposed abdomen model will be examined close to the portable radio terminals in next Chapter.

Chapter 6 Evaluation of the SAR inside a simple abdomen model of pregnant women

6.1 Introduction

Portable radio terminals for business purposes at 150 MHz are usually used in a radio set, which is attached to the human abdomen. In addition, the EM waves at 150 MHz can penetrate into the human body more easier than those at the frequencies of cellular phones [15]–[17]. Therefore, it is important to evaluate the SAR in the internal organs in order to confirm the EM-safety problem by use of the portable radio terminals at 150 MHz. In particular, pregnant women such as police women and her fetus may be exposed to the EM waves radiated from the portable terminals at 150 MHz. In addition, to the author's knowledge, very little work is currently available in the published literature on the evaluation of the SAR in the pregnant women and her fetus at 150 MHz. In addition, the measurement of the SAR inside the layered phantom is also hardly evaluated in the previous studies. It is therefore important to evaluate that the SAR in the pregnant women in the vicinity of the portable terminals at 150 MHz.

In this research, the SAR in the simple abdomen phantom as expressed by Section 5.4 is measured using the thermographic method. However, in the thermographic method, long time exposure at 120–180 s is needed to evaluate the precision SAR distribution inside the phantom at 150 MHz [36]. Such long time exposure causes the thermal error. Hence, I evaluate the thermal error in the abdomen model and the exposure condition of the measurement

using the thermal analysis.

In this Chapter, the SAR inside the proposed simple abdomen model of the pregnant women close to the portable radio terminals is investigated at 150 MHz. First, in Section 6.2, the numerical and experimental models are proposed. In Section 6.3, the SAR distribution and average value in the abdomen model is calculated using the FDTD method. Next, in Section 6.4, the thermal error in the abdomen model and the exposure condition of the measurement is solved by the thermal analysis. Finally, in Section 6.5, the temperature distribution in the abdomen phantom is measured and compared with the calculated result.

6.2 Numerical and experimental Models

6.2.1 Structure of antennas

Figure 6.1 shows the structure of the normal mode helical antennas (NHAs) [55]–[57]. From now on, the antennas are called the ANT1 and ANT2. In this dissertation, the NHAs simulates the actual portable radio terminals at 150 MHz, which is composed by a monopole NHA and a small radio box. The validity of the replacement of the NHAs has been proposed [36]. These NHAs are conjugate-matched by a capacitor. The parameters of ANT1 (pitch S, number of windings N, winding diameter $2R$, and axial length L) are as follows; $L = 212$ mm (0.11λ), $N = 38.4$, $2R = 15$ mm, $S = 5.4$ mm. On the other hand, the data of ANT2 are as follows; $L = 356$ mm (0.18λ), $N = 99$, $2R = 7.5$ mm, $S = 3.4$ mm. Here, the $2R$ of ANT1 is twice of that of ANT2 in order to improve the radiation efficiency. The diameter of the metal wire (copper, $\sigma = 5 \times 10^7$ S/m) is 1 mm. The measured efficiency of the NHAs in free space is –1.4 dB (ANT1) and –1.2 dB (ANT2).

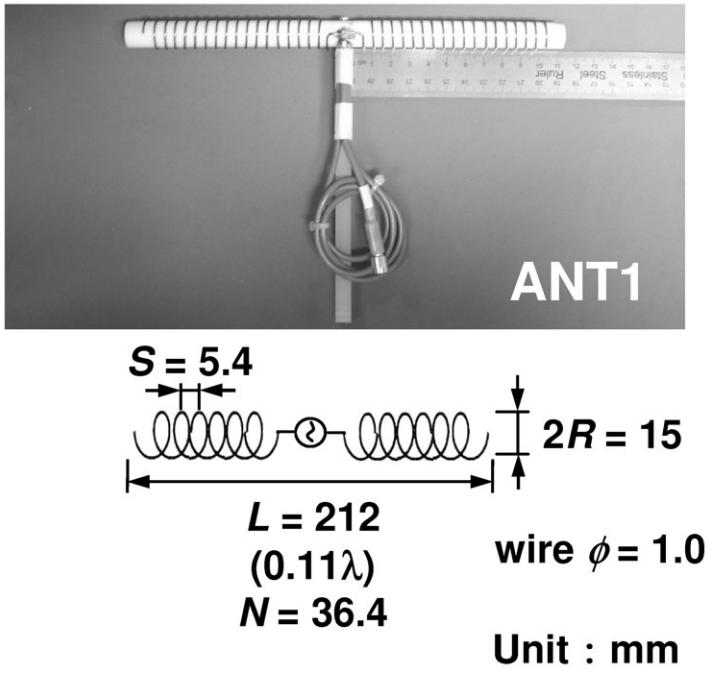

(a) ANT1

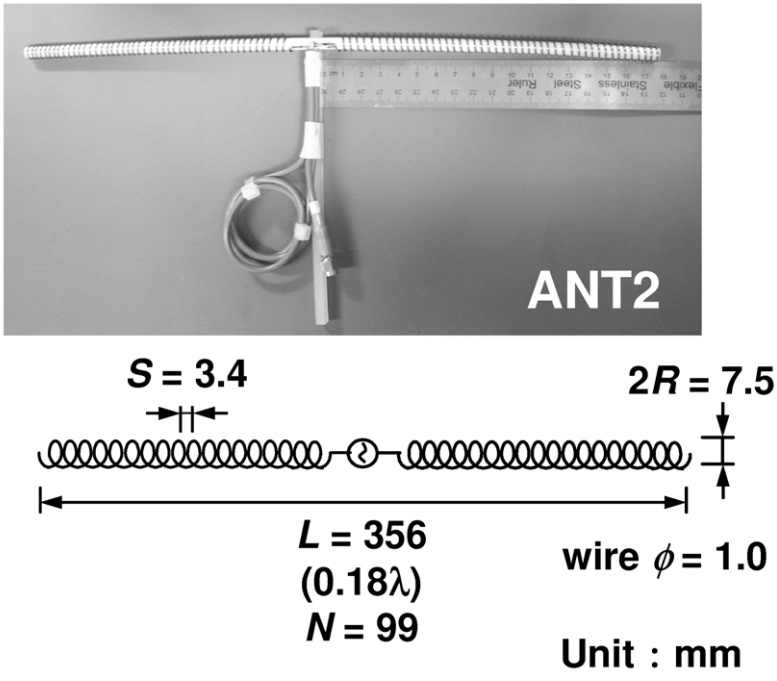

(b) ANT2

Fig. 6.1 Normal mode helical antennas.

6.2.2 Model

Figure 6.2 shows the numerical and experimental model. Figure 6.2 (a) illustrates the evaluation model of the normal case, when the NHA is attached to the side of a simple abdomen model, as shown in Fig. 5.10. On the other hand, Fig. 6.2 (b) presents the evaluation model to consider the worst case of the exposure inside the fetus, when the NHA is attached in front of the abdomen model. In addition, the distance between the antenna and the surface of the human model is 40 mm in order to realize the actual situation. Moreover, the origin is the feed point of the antenna.

Figure 6.3 (a) illustrates the observation plane, which is the $x-y$ plane at $z=0$, of the SAR and temperature distributions inside the abdomen model in the normal case. On the other hand, Fig. 6.3 (b) shows the observation plane and line in the worst case. Here, the observation line is direct under the feed point along the y-axis on the observation plane to confirm the variation in the distributions around the boundary of the layer.

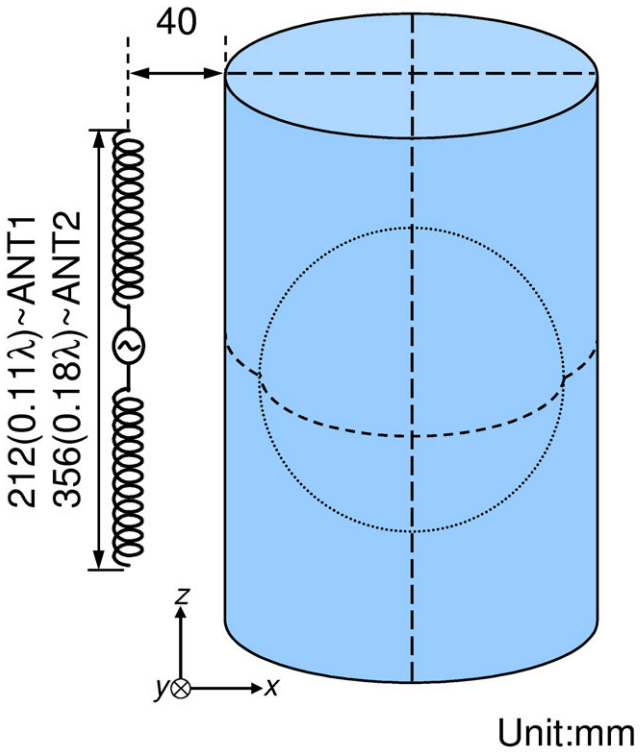

(a) Side (normal position)

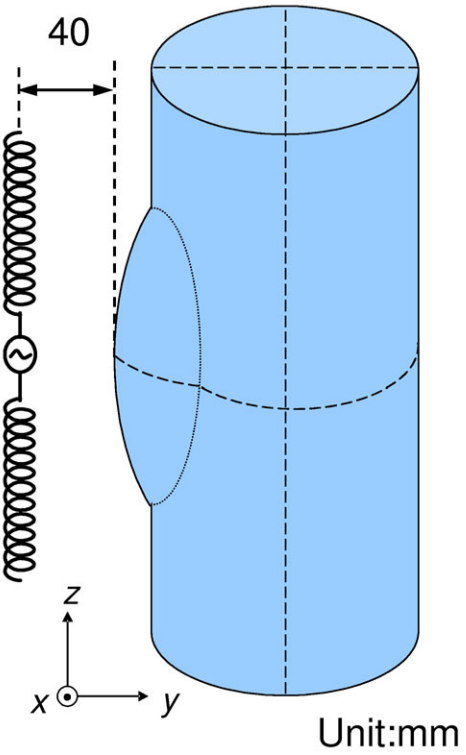

(b) Front (worst position)

Fig. 6.2 Numerical and experimental models.

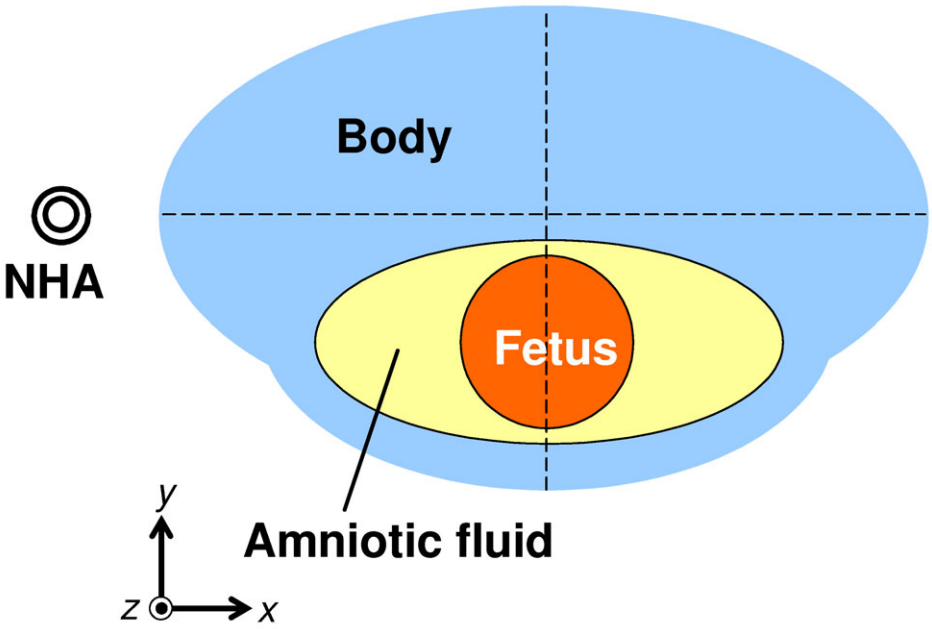

(a) Side (normal position)

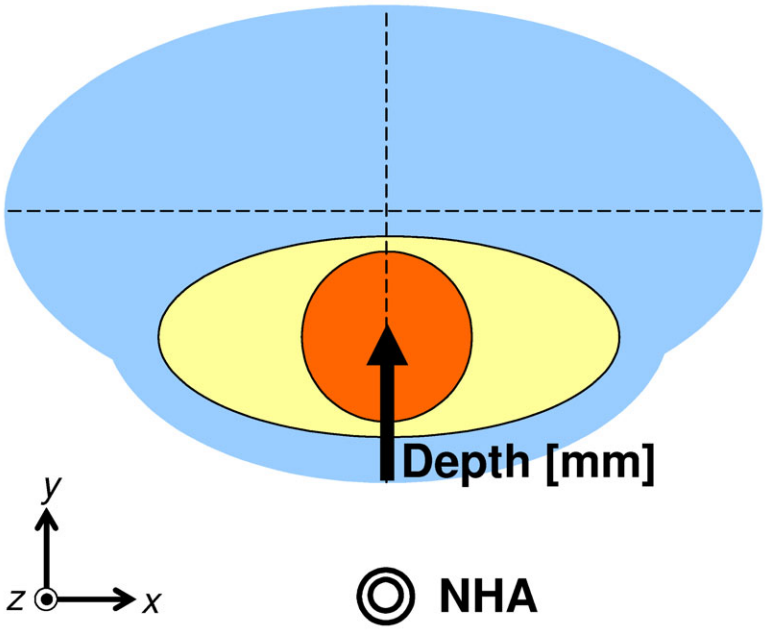

(b) Front (worst position)

Fig. 6.3 Observation plane in the models.

6.3 SAR calculation

6.3.1 Numerical condition

The FDTD software (SEMCAD ver. 1.6) is used for the SAR calculating in the abdomen models. The parameters of the FDTD calculation employed in this Chapter are as follows. The cell size of the NHAs is 0.5–1 mm, abdomen model is 0.5–5 mm, and free space is 0.5–20 mm. In addition, the absorbing boundary condition is the PML (eight layers). Moreover, the calculation time is thirty (ANT1) or twenty five (ANT2) periods at 150 MHz to get converged results.

Table 6.1 describes the measured dielectric constants and the density of the body-, amniotic fluid-, fetus- equivalent phantoms. Here, the electrical properties of the phantoms are measured using the HP-85070M dielectric-probe measurement system. The density is evaluated by the weight ratio of the water, which has the same volume of tissues.

Table 6.1 Dielectric constants and density of tissues

Tissue	Body	AF	Fetus
ε_r	42.1	78.3	76.9
σ [S/m]	0.50	1.23	0.91
ρ [kg/m^3]	907	986	967

AF: Amniotic fluid

6.3.2 Calculated SAR distributions

SAR distributions on the observation plane

Figure 6.4 shows the calculated SAR distribution inside the abdomen model on the observation plane, as given by Fig. 6.3 (a), when the antennas are attached to the side of the model. From now on, the input power of the antennas is normalized to 1 W. Here, the output power of the antennas is corrected by the efficiency in free space, as expressed in 6.2.1.

As shown in Fig. 6.4, the peak SAR of the ANT1 is larger than that of the ANT2 because the axial length of the ANT2 is longer than that of the ANT1. In addition, the SAR in the fetus is hardly obtained because the SAR in the fetus is attenuated by the distance from the surface. Moreover, the SAR in the fetus produced by the ANT1 is almost equal to that by the ANT2.

Figure 6.5 illustrates the calculated SAR distribution inside the abdomen model on the observation plane, as given by Fig. 6.3 (b), when the antennas are attached in front of the model to evaluate the worst case exposure.

From Fig. 6.5 (a), the SAR distribution in the model by the ANT1 is asymmetrical on the y axis because of the current distribution on the NHA. Here, the asymmetry by the ANT1 is larger than that by the ANT2. In addition, from Figs. 6.5 (a) and (b), the high SAR distribution in the amniotic fluid is obtained because the conductivity of the amniotic fluid is almost 2.6 times higher than that of the body, as expressed by Table 6.1. The result also shows the variation in the SAR distribution around the boundary of the layer of the tissues.

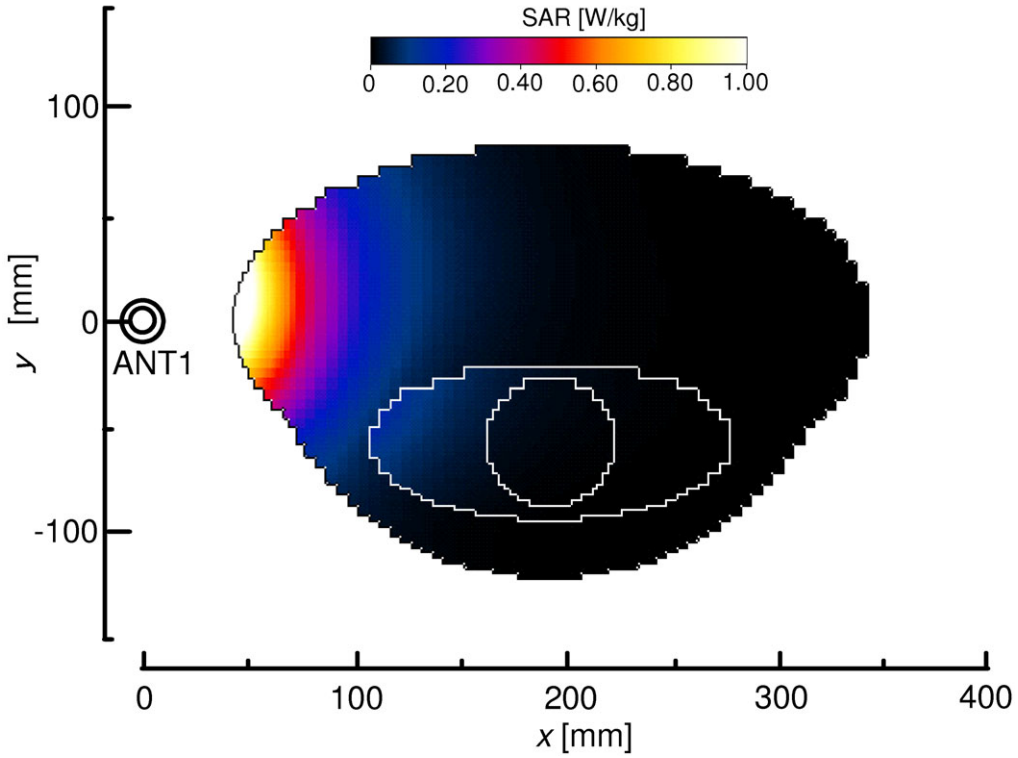

(a) ANT1

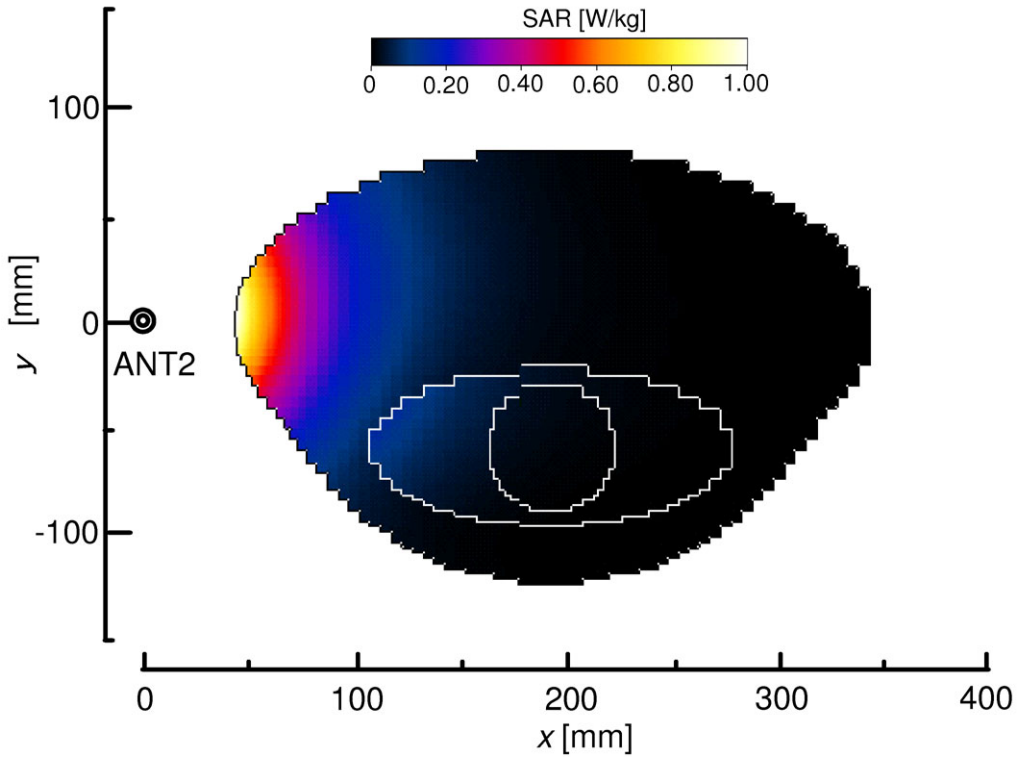

(b) ANT2

Fig. 6.4 SAR distributions on the observation plane (normal position).

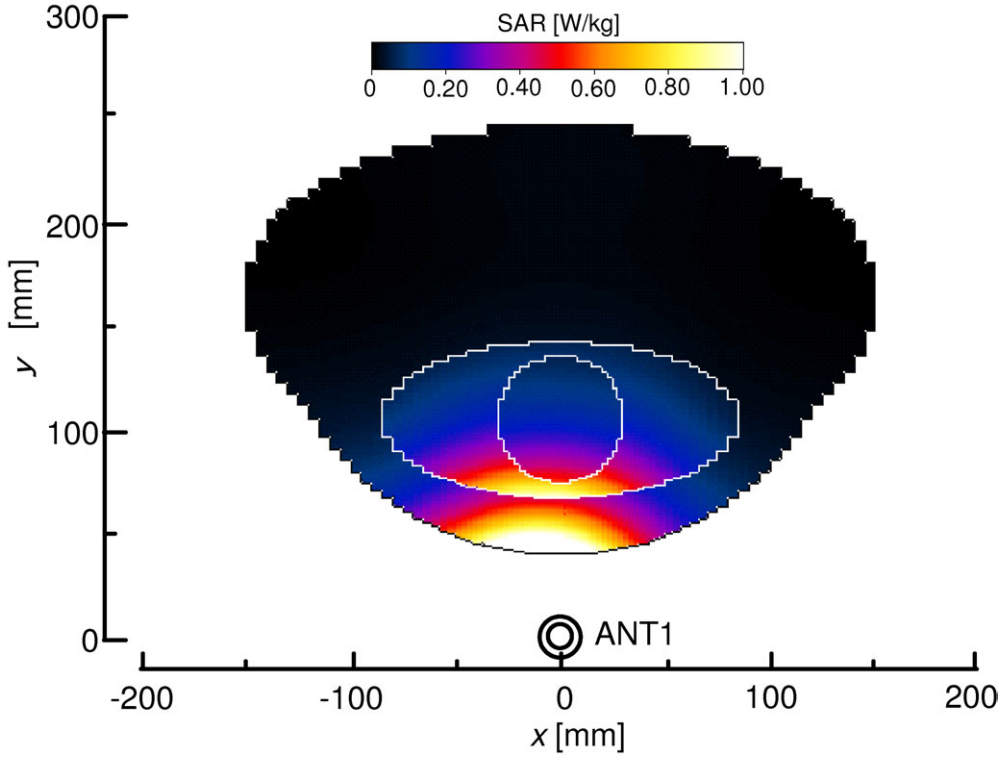

(a) ANT1

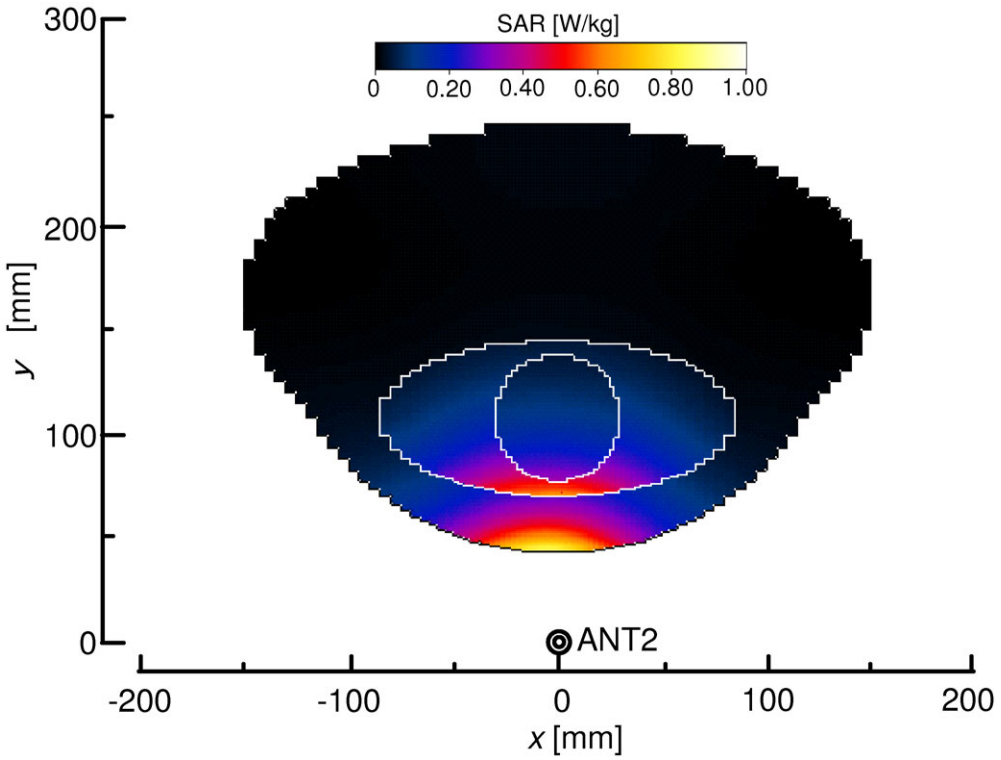

(b) ANT2

Fig. 6.5 SAR distributions on the observation plane (worst position).

SAR distributions on the observation line

Figure 6.6 shows the calculated SAR distribution on the observation line, as given by Fig. 6.3 (b). Here, the SAR distribution of the homogeneous model, which is the body-equivalent tissue, is also evaluated to confirm the variation in the SAR distribution caused by the layered structure.

As shown in Fig. 6.6, it has been confirmed that the attenuation of the SAR in the body is sharp varied by the layered structure. In addition, the SAR distribution inside the model varies suddenly around the boundary of the tissue because the difference of the conductivity between the tissues is very large, as expressed in Table 6.1. Moreover, the SAR in the fetus is larger than that in the homogeneous model.

From these results, it has been confirmed that the layered abdomen model of pregnant women is indispensable to accurate evaluate the SAR in the fetus.

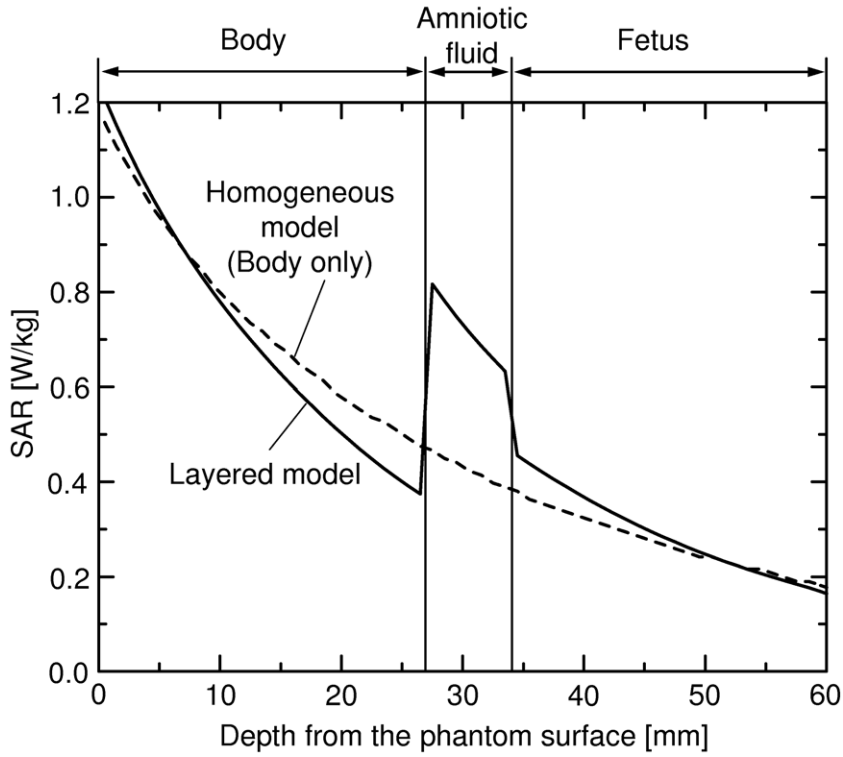

(a) ANT1

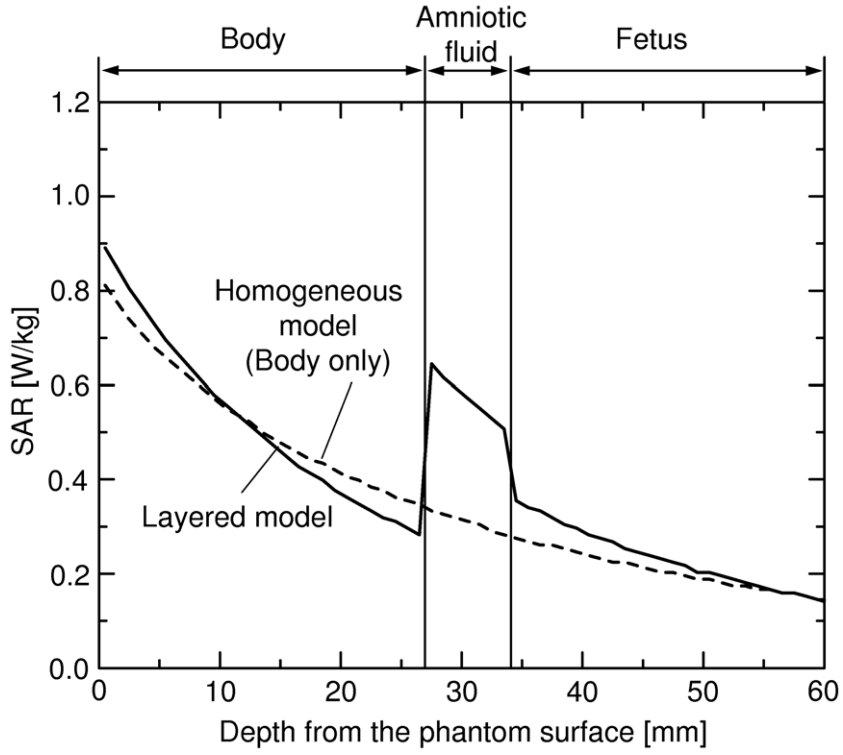

(b) ANT2

Fig. 6.6 SAR distributions on the observation line.

Local average SARs

Table 6.2 describes the calculated local 1 g and 10 g average SARs in the model, when the NHAs are attached the side of the abdomen model. As shown in Table 6.2, it is confirmed that the EM waves is hardly penetrate into the fetus. The result also suggests the local 10 average SAR in the fetus is less than 0.15 W/kg at 5 W input (maximum power of portable radio terminals in Japan), when the antenna is attached to the side of the abdomen of pregnant women.

Table 6.3 shows the calculated local 1 g and 10 g average SARs in the model, when the NHAs are attached in front of the abdomen model. From Table 6.3, the local average SAR produced by the ANT1 is almost equal to that by the ANT2. The result also suggests the local 10 average SAR in the fetus is less than 1.5 W/kg at 5 W input. From these results, the local 10 g average SAR in the fetus is less than 2 W/kg which is the limit, as expressed in Section 2.2.

Table 6.2 Local average SARs in the mother and fetus in the normal case exposure

Tissue		ANT1	ANT2
Mother	$SAR_{1\ g}$	1.12	0.90
	$SAR_{10\ g}$	0.91	0.72
Fetus	$SAR_{1\ g}$	0.03	0.03
	$SAR_{10\ g}$	0.02	0.03

Table 6.3 Local average SARs in the mother and fetus in the worst case exposure

Tissue		ANT1	ANT2
Mother	$SAR_{1\ g}$	1.04	0.76
	$SAR_{10\ g}$	0.79	0.59
Fetus	$SAR_{1\ g}$	0.39	0.32
	$SAR_{10\ g}$	0.30	0.26

6.4 Thermal analysis

6.4.1 Necessity of the thermal analysis

The thermal error is mainly caused by the thermal conduction inside the phantom and the heat transfer on the phantom surface [37]. In order to reduce these thermal errors, the short time exposure is important. However, the short time exposure is difficult at VHF band [35], [36]. In these cases, the thermal analysis inside the phantom is indispensable. Therefore, this section proposes the effect of the exposure time on the temperature distribution inside the abdomen models.

6.4.2 Mathematical formulation

The temperature distribution inside the biological tissue could be calculated by solving the bioheat equation [58]

$$\rho c \frac{\partial T}{\partial t} = \kappa \nabla^2 T - \rho \rho_b c_b F (T - T_b) + \rho \cdot \mathrm{SAR} \tag{6.1}$$

where T is the temperature of the tissue [K], t is the time [s], ρ is the density of the tissue [kg/m^3], c is the specific heat of the tissue [J/kg·K], κ is the thermal conductivity of the phantom [W/m·K], ρ_b is the density of the blood [kg/m^3], c_b is the specific heat of the blood [J/kg·K], T_b is the temperature of the blood [K], and F is the blood flow rate [m^3/kg·s].

Here, in solid phantoms, F is equal to 0. Therefore, the temperature inside the phantom is given by

$$\rho c \frac{\partial T}{\partial t} = \kappa \nabla^2 T + \rho \cdot \mathrm{SAR} \tag{6.2}$$

Additionally, the boundary condition for Eq. (6.2) is given by the following equation [59]–[62]

$$h(T - T_a) = \kappa \frac{\partial T}{\partial n} \tag{6.3}$$

where h is the heat transfer coefficient [W/m^2·K], T_a is the temperature of the air around the phantom [K], and $\partial T/\partial n$ is the variation in the temperature toward normal from the

phantom surface. Therefore, the temperature-rise inside the phantom can calculate by solving Eqs. (6.2) and (6.3). The thermal analysis inside the head model using these equation has been widely proposed [59]–[62]. Here, $t \to 0$, the SAR is given by following equation

$$\mathrm{SAR} = c\frac{\Delta T}{\Delta t} \qquad [\mathrm{W/kg}] \tag{6.4}$$

In the thermographic method, the SAR is given by Δt and ΔT using Eq. (6.4). However, in the thermal measurement, the SAR includes the thermal error by κ and h because the $\Delta t \to 0$ is difficult at 150 MHz.

6.4.3 Numerical condition

The thermal solver, which is including SEMCAD ver. 1.6, is used for the thermal analysis in the abdomen model. In the thermal analysis, the temperature distribution inside the model as given by Fig. 6.2 (b) is calculated because the measurement of the temperature-rise inside the fetus when the NHAs are attached the side of the abdomen model. In addition, the measurement of the variation in the SAR distribution around the boundary is important.

Table 6.4 describes the thermal properties of the phantoms. Here, these values of the body and fetus are measured by the Agune Technical Center Co., Ltd., Tokyo, Japan. On the other hand, the values of the amniotic fluid are presumptive value from the results of the fetus because the ingredients of the two tisse is almost similar. As shown in Table 6.4, the thermal conductivity is larger than that of the others.

In the thermal analysis, the calculated results of the SAR by the FDTD method is used as a source of heat in Eq. (6.2). The conditions of the thermal analysis are as follows. The first temperature of the phantoms and the air is 18 $^{\circ}$C to realize the actual measurement. In addition, the heat transfer coefficient h is 20 W/m$^2\cdot$ K to realize the condition of the radio anechoic chamber in Chiba University. Moreover, the input power of the antennas is 84 W,

which is corrected by the cable loss. Furthermore, the exposure time is varied from 60–240 s. Here, the output power of the antennas is corrected by the efficiency of the NHAs.

Table 6.4 Thermal constants of tissues

Tissue	Body	AF	Fetus
c [J/kg·K]	3,060	4,000	4,030
κ [W/m·K]	0.36	0.60	0.61

AF: Amniotic fluid

6.4.4 Calculation results of thermal analysis

Figure 6.7 shows the temperature-rise ΔT distribution on the observation line, as given by Fig. 6.3 (b). As shown in Fig. 6.7, the increase in the ΔT in the abdomen model is proportional to the increase in the exposure time Δt. In addition, the increase in the error around the surface, which is caused by the heat transfer toward the air, is also proportional to the increase in the Δt. Moreover, the $\Delta T \geq$ several K in the fetus is necessary to evaluate the temperature distribution inside the fetus. Therefore, Δt above 180 s is needed to measure the distribution in the fetus.

Figure 6.8 illustrates the SAR distribution, which is calculated by the temperature distribution using the Eq. (6.4), on the observation line. The FDTD line is the calculated result of the SAR distribution in Fig. 6.6. As shown in Fig. 6.8, the increase in the error around the boundary of the amniotic fluid is proportional to the increase in the exposure time Δt. In addition, the maximum difference between the FDTD and the others is almost equal to 40%. Moreover, the difference in the amniotic fluid is the largest because the SAR around this tissue is larger than that of the others. These results also suggests the precision evaluation of the SAR in the abdomen model using the raw temperature distribution is difficult.

From Figs. 6.7 and 6.8, the optimize exposure time of this model is 180 s in each antenna to evaluate the temperature distribution in the fetus.

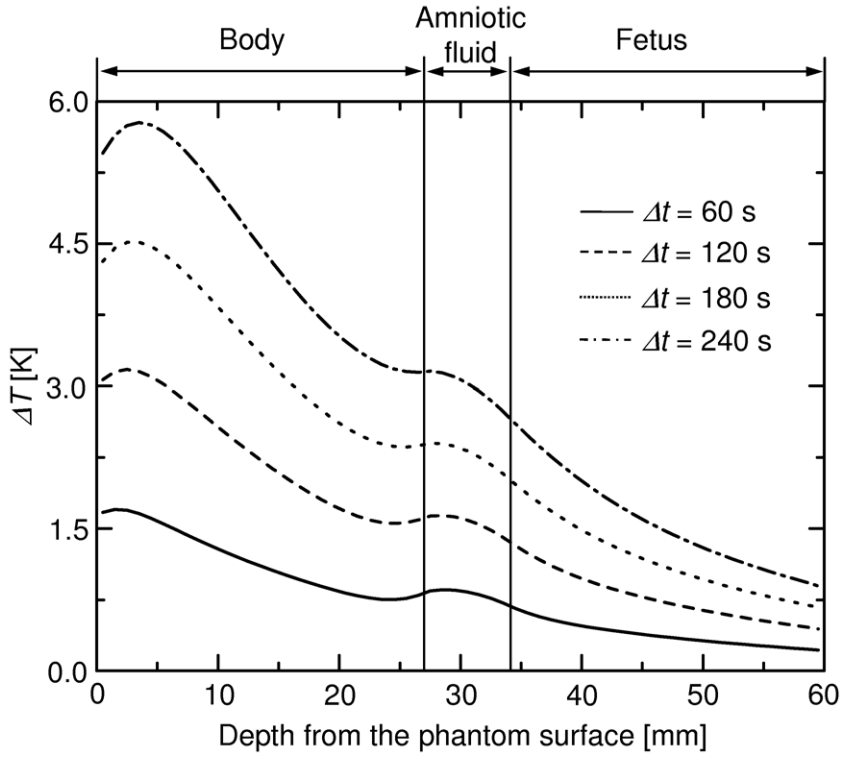

(a) ANT1

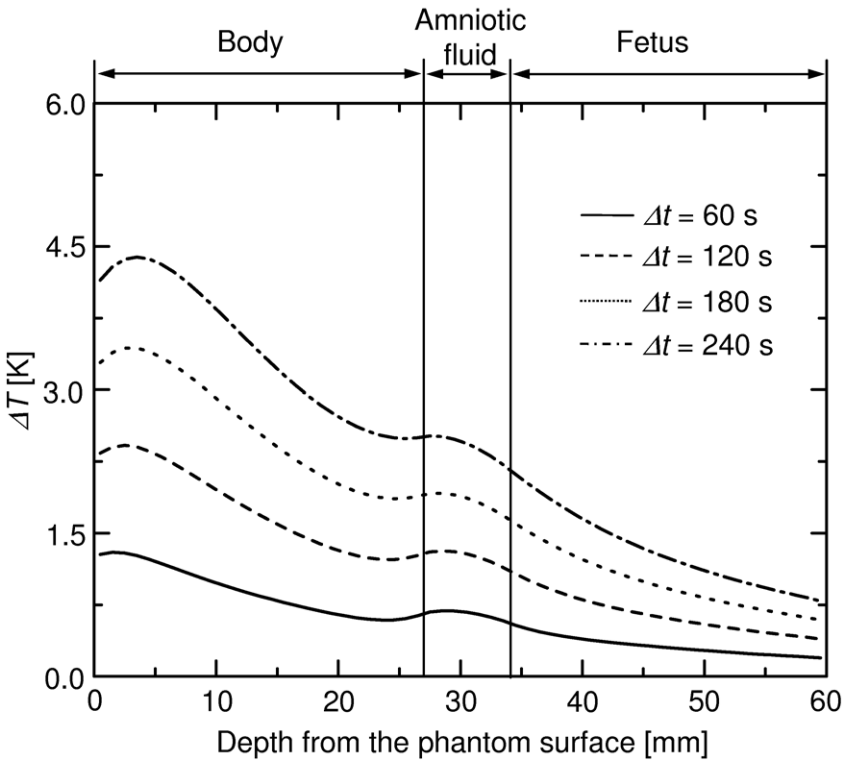

(b) ANT2

Fig. 6.7 Temperature-rise distributions on the observation line.

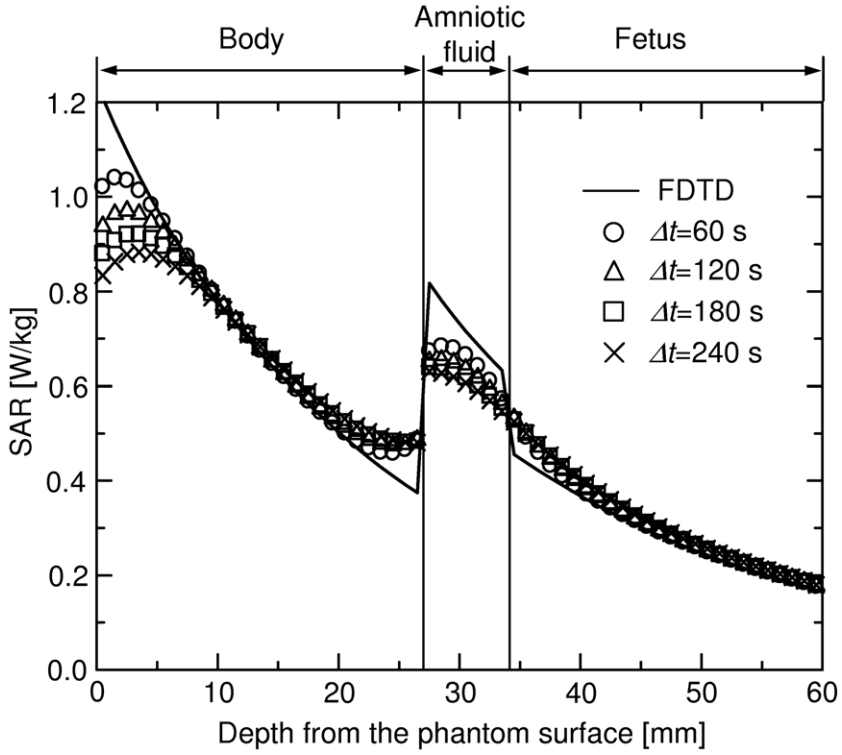

(a) ANT1

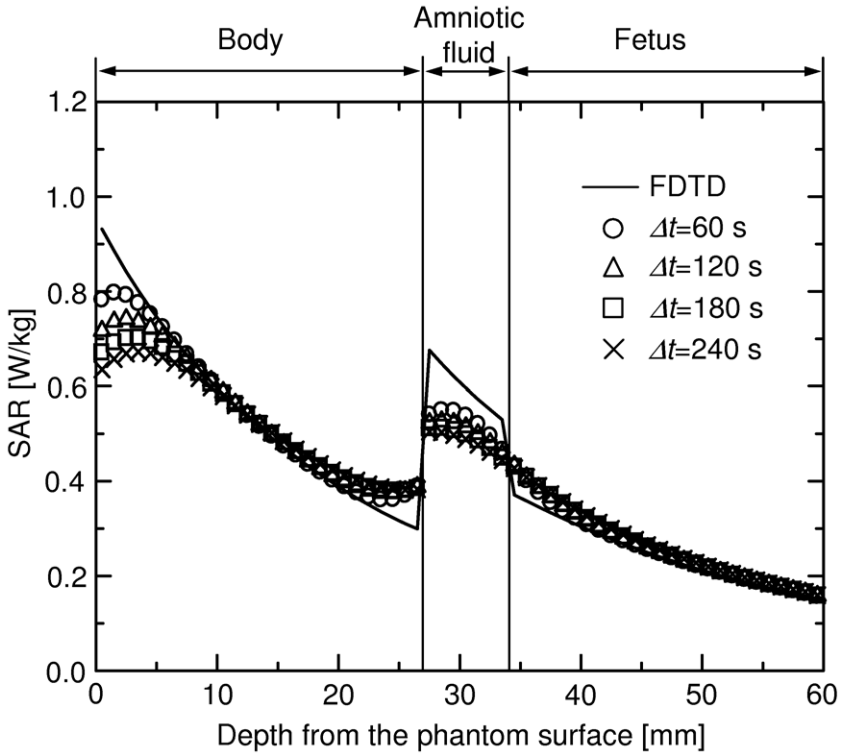

(b) ANT2

Fig. 6.8 SAR distributions on the observation line based on the thermal analysis.

6.5 Measurement

In Section 6.4, the exposure time in the measurement is simulated. In this Section, the temperature distribution inside the phantom is measured.

6.5.1 Condition and Setting

Figure 6.9 shows the setting of the measurement. The temperature distribution is measured using the radio anechoic chamber in Chiba University. The infrared camera used for the measurement is TH3102MR manufactured by the NEC Co., Ltd., Tokyo, Japan.

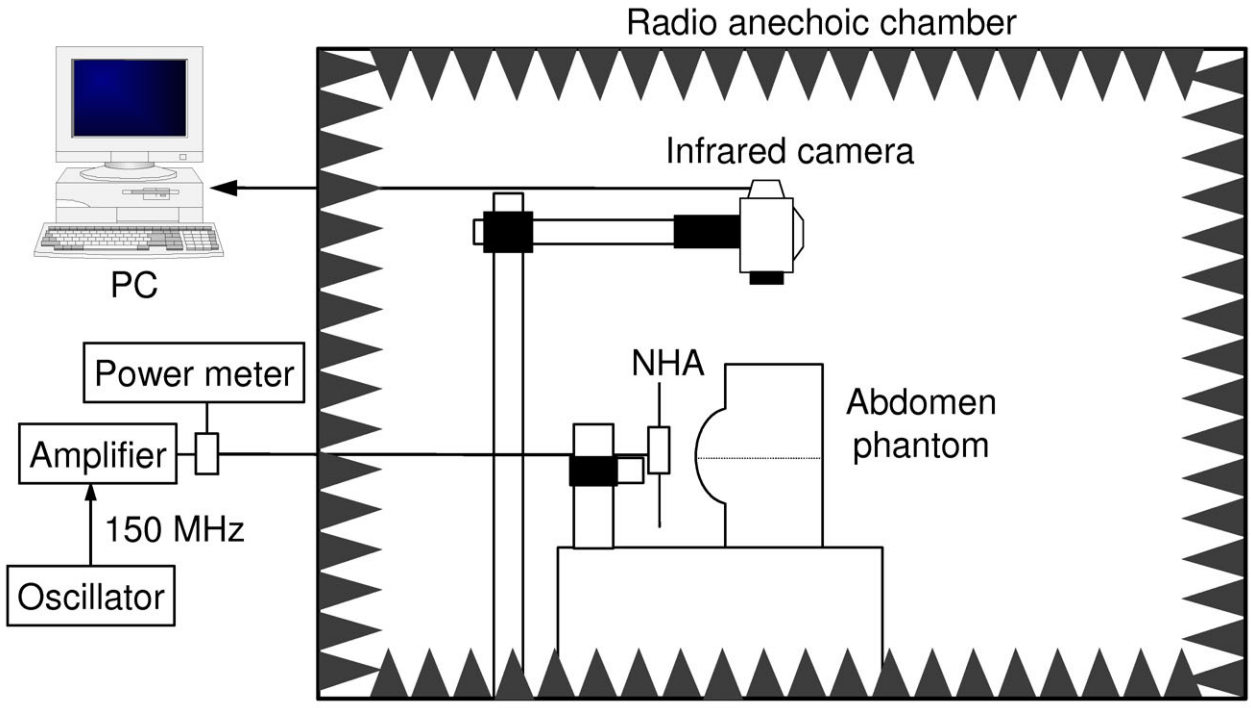

Fig. 6.9 SAR measurement system using the thermographic method.

6.5.2 Measurement of the emittance and corrective method of the temperature

Measurement of the emittance

The simple abdomen phantom is composed by the three types of phantoms. Therefore, the measurement of the emittance of each phantom is necessary to evaluate the precision temperature distribution. In this study, two types of the measurement method, which are using a contact thermometer and black tape ($X = 0.95$).

Figure 6.10 shows the two measurement method of emittance. The measurement method using the contact thermometer (Fig. 6.10 (a)) are as follows. At first, the water of higher temperature (about 70 ° C) than the phantom (about 70 ° C) is touched to the surface of the phantom for about ten seconds in the first step, and hot spot is generated. Then, the temperature of the hot spot the surface is measured and compared using an infrared camera and contact thermometer when the emittance of the infrared camera is varied. At this time, the temperature measured by the contact thermometer is used as the accurate. In the second step, the temperature gradient with the hot spot temperature is examined. If temperature gradient is positive, the estimate of the emittance is lowered, and the measurement is repeated from the second step. In addition, if temperature gradient becomes zero, the emittance of the phantom is fixed In Fig. 6.10 (b), the temperature on the black tape is used as the accurate.

Table 6.5 describes the measured emittance of the phantom. In the two methods, almost same results are obtained. As shown in Table 6.5, the emittance of the body is deferent from that of the others because the emittance of the phantom is due to the ingredient.

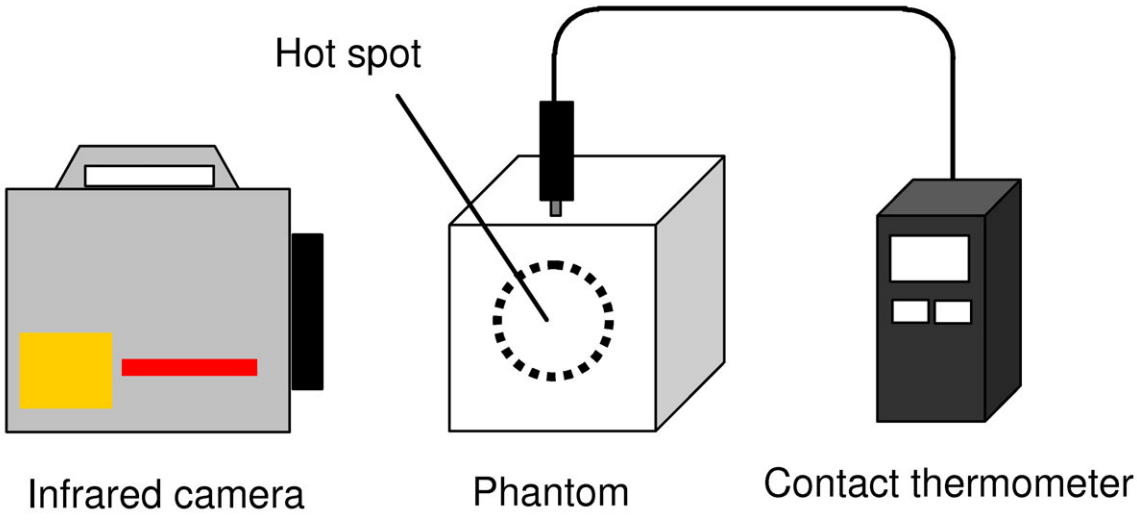

(a) Using a contact thermometer

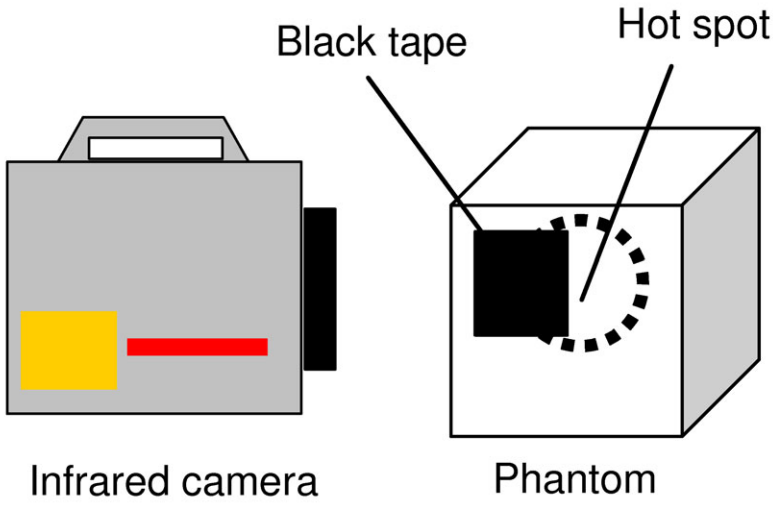

(b) Using a black tape($X = 0.95$)

Fig. 6.10 Measurement method of the emittance.

Table 6.5 Measured results of the emittance

Tissue	Body	AF	Fetus
emittance	0.60	0.84	0.84

AF: Amniotic fluid

Corrective method of the temperature

In the measurement, the infrared camera in our laboratory can evaluate the temperature using only an emittance. Therefore, three times measurement is necessary to evaluate the temperature in the three types of phantoms. The correction of the temperature is necessary to evaluate the temperature in the phantom at same time. In this Section, corrective method of the temperature using the difference of the emittance is proposed. Here, the emittance of the fetus-equivalent phantom is used as a criteria because the temperature of the fetus is the most important in this study.

The emittance of the phantom is defined as expressed in Eq. (2.3). In the measurement, the temperature-rise in the model using the emittance of the fetus phantom is given by

$$\Delta T_p : \Delta T_a = 1 : X_a \tag{6.5}$$

where ΔT_p is the temperature-rise in the model using the emittance of the black body [K], ΔT_a is the temperature-rise in the model using the emittance of the fetus phantom, X_a is the emittance of the fetus phantom. Similarly, the temperature-rise in the model using the emittance of the body or amniotic fluid phantom is given by

$$\Delta T_p : \Delta T_b = 1 : X_b \tag{6.6}$$

where ΔT_b is the temperature-rise in the model using the emittance of the body or amniotic fluid phantom, X_b is the emittance of the body or amniotic fluid phantom. Substitution of

Eq. (6.6) in Eq. (6.5) leads to Eq. (6.7)

$$\Delta T_b = \Delta T_a \frac{X_b}{X_a} \quad [\mathrm{K}] \tag{6.7}$$

From Eq. (6.7), the actual temperature-rise in the body or amniotic fluid phantom can be evaluated.

Table 6.6 describes the comparison between the measured temperature-rise in the phantoms ΔT_c [K] by the contact thermometer and the that by the infrared camera ΔT_b using Eq. (6.7) when the hot water is torched on the phantom at 10 s. As shown in Table 6.6, difference between the ΔT_c and the ΔT_b is less than $\pm$ 0.1 °C. The difference is including in the precision of the infrared camera. Therefore, I have confirmed from these results that the temperature distribution in the three types of phantoms can be evaluated using the proposed corrective method.

Table 6.6 Comparison between ΔT_c and ΔT_a

Tissue	ΔT_c [K]	ΔT_a [K]	ΔT_b [K]	$\Delta T_c - \Delta T_b$ [K]
Body	2.4	3.3	2.36	0.04
Fetus	2.4	2.4	2.4	0

ΔT_c: Temperature-rise by the contact thermometer

6.5.3 Measured temperature distribution

Figure 6.11 illustrate the temperature-rise ΔT distribution on the observation plane after 84 W–180 s exposure using the thermographic method at X =0.84, when the ANT1 is attached in front of the phantom. Here, the temperature distribution is not corrected by use of the difference of the emittance. As shown in Fig. 6.11, the high ΔT distribution around the amniotic fluid and fetus is obtained. On the other hand, the ΔT in the body is smaller than that of the others. Moreover, the SAR in the abdomen model is asymmetrical on the y axis.

Figure 6.12 shows the ΔT distribution on the observation line. Here, the distribution in the body is corrected by the difference of the emittance, as expressed in last Section. From Fig. 6.12, the ΔT distribution of the measurement around the amniotic fluid and fetus layer is larger than that of the calculated one. The difference is mainly generated by the gap between the body layer along the z axis. On the other hand, the distribution of the measurement in the body layer conflicts with the calculated one, which is also caused by the gap between the upper and lower phantom. In the measurement, the precision setting of the phantom is indispensable to evaluate the SAR inside the abdomen phantom of the pregnant women using the thermographic method. It is therefore necessary to develop the sticky body phantom to realize the precision measurement.

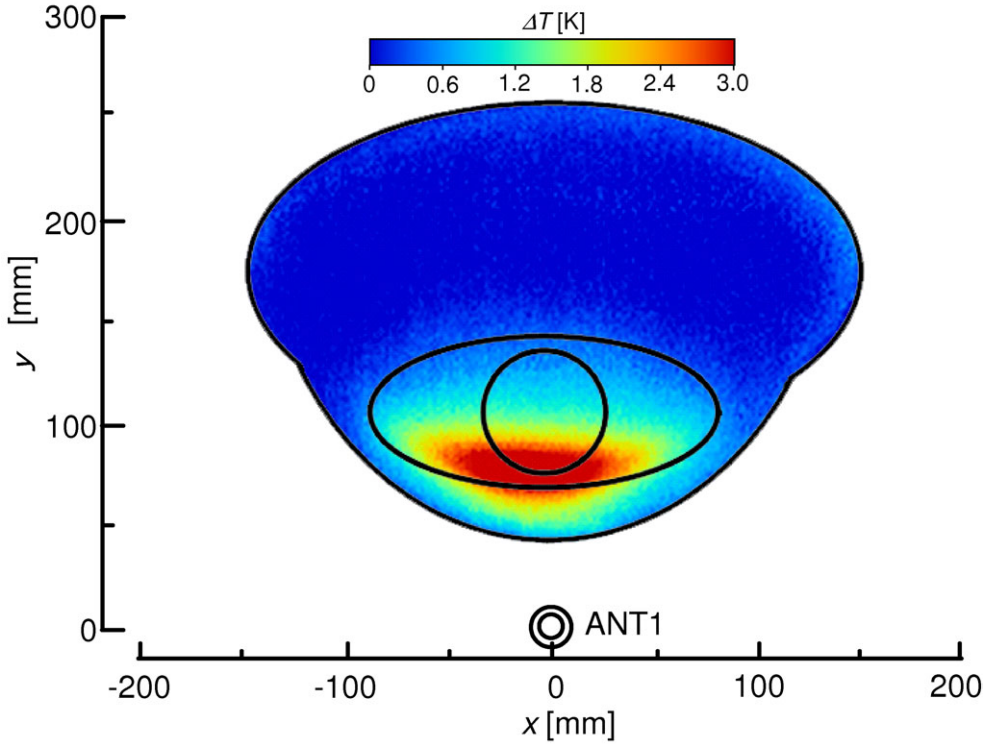

Fig. 6.11 Measured temperature-rise distributions on the observation plane (ANT1).

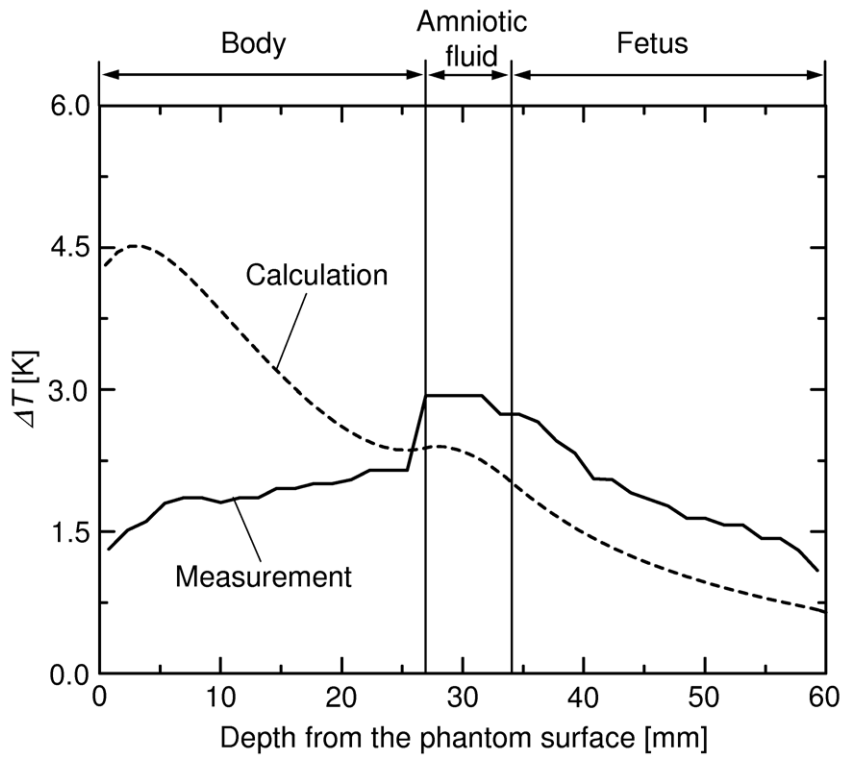

Fig. 6.12 Measured temperature-rise distributions on the observation line.

6.6 Conclusions

In this Chapter, the SAR inside the proposed simple abdomen model of the pregnant women, which was close to the NHAs, was investigated at 150 MHz.

The important findings in this Chapter are as follows;

1) The SAR distribution in the abdomen model was calculated using the FDTD method. As a result, the peak SAR in the abdomen model by the ANT1 (0.11λ NHA) is larger than that by the ANT2 (0.18λ NHA). On the other hand, the attenuation of the SAR in the model by the ANT1 is larger than that by the ANT2 because the diffraction of the E-field in z direction of the ANT2 is larger than that of the ANT1. Moreover, the SAR distribution around the boundary of the amniotic fluid is sharp varied by the layered structure when the antenna is attached in front of the body.

2) The average SAR in the abdomen model was also investigated. As a consequence, the local 10 g average SAR in the fetus is less than 0.15 W/kg at 5 W input (maximum input power of the portable radio terminals), when the antenna is attached to the side of the model. On the other hand, the 10 g average SAR in the fetus is less than 1.50 W/kg at 5 W input, when the antenna is placed in front of the model. From these results, the 10 g average SAR in the fetus is less than 2 W/kg to consider the worst case exposure.

3) The thermal error in the abdomen model and the exposure condition of the measurement was solved by the thermal analysis. As a result, it has been confirmed that the optimize exposure time is 180 s in each NHA. In addition, the maximum thermal error is almost equal to 40% at 180 s exposure.

4) The temperature-rise distribution in the abdomen phantom was measured and compared with the calculated result of the thermal analysis. As a result, great difference between the measurement and calculation, which is caused by the gap of the phantom, is obtained. In the measurement, the precision setting of the phantom is indispensable to evaluate the SAR inside the abdomen phantom of the pregnant women using the thermographic method.

In near future, I will measure the temperature distribution in the abdomen model once again using the sticky body phantom.

Chapter 7 Conclusions

This dissertation dealt with the evaluation of the SAR inside the human bodies which is close to the portable communication devices at VHF and UHF bands.

In Chapter 2, the definition, limits of guideline, and measurement method of the SAR were introduced. This Chapter also explained the problems of the measurement method of the SAR.

In Chapter 3, the simple evaluation method of the estimating local 10 g average SAR was proposed, which is based on the SAR distribution in the specific plane or axes by use of the thermal technique. First, the limit of simplification was investigated when the four types of the antenna, which is the half-wave dipole antenna, monopole antenna mounted on the metal box, PIFA, and half-wave dipole antenna with the planar reflector, were close to the COST244 cubic and spherical head model at 900 MHz and 2 GHz. As a result, it had been confirmed that the SAR distribution in the horizontal plane or axes is necessary to evaluate the local 10 g average SAR because the variation in the horizontal direction is larger than that in the vertical one using the antennas. In addition, the proposed method was almost able to evaluate the local 10 g average SAR, which is the deviation within ± 10%, in the cubic model at 900 MHz and 2 GHz. Moreover, the difference between the two methods in the spherical model was within –12% to +17% at both frequencies. Next, the effect of the distance between the antenna and the head model on the averaged SAR using this method was evaluated at 900 MHz to investigate the application of this method. The results indicated the deviation of the local 10 g average SAR was within ± 10% when the distance

between the two is larger than 10 mm. Third, the dependence of the proposed method on the frequency was investigated at 300 MHz to 3 GHz. It was found from the result that the proposed method can be applied to the local average SAR estimation in the cubic model at 300 MHz to 3 GHz. Finally, I evaluated the average SAR in the realistic head model at 2 GHz. The result reached that the proposed method also evaluates the average SAR in the realistic head model within ± 15% of the deviation. From these investigations, I may conclude the proposed method can evaluate the local 10 g average SAR using the distribution on the optimum planes and axes within ± 10% of the deviation at 300 MHz to 3 GHz, except in special cases.

In Chapter 4, I investigated the effect of the inaccurate dielectric constants of the biological tissue-equivalent phantom on the local SARs in a human model when the dielectric constants are changed at 150 MHz, 900 MHz, 2 GHz, and 3 GHz. First, Local peak, 1 g and 10 g average SARs in the human model were calculated using the FDTD method when the relative permittivity ε_r or conductivity σ are varied from criteria to ± 20% under the condition that the other was the unity at 150 MHz–3 GHz. As a result, it has been confirmed the decrease in the local SARs is proportional to the increase in the ε_r. On the other hand, the increase in the local SARs is proportional to the increase in the σ. Moreover, the dependence of the local SARs on the inaccurate ε_r or σ is due to the frequency. However, the variation in the peak SAR is hardly due to the frequency. Local 1 g and 10 g average SAR were evaluated when the ε_r and σ were simultaneously varied from criteria to ± 20% at 150 MHz–3 GHz. As a consequence, I have confirmed that the effect of the inaccurate dielectric constants on the local average SARs are almost equal to the sum of the change in the SAR caused by the inaccurate $\varepsilon_r$and that by the σ as given by 1). In addition, the variation in the local average SARs is dependent on the frequency. Next, the variation in the SAR distribution inside the model, which was caused by the inaccuracy of the relative

permittivity or conductivity, was evaluated to try to find the cause of the error of the local average SARs. In addition, the relationship between the variation in the relative permittivity or conductivity and the local SARs was investigated. Moreover, the effect of the shape on the variation in the local SAR was investigated when the dielectric constants were varied at 2 GHz. As a result, it has been confirmed that the effect of the variation in the average SARs is less than 3%. In addition, the dependence of the change in the average SAR on the inaccurate dielectric constants is slightly due to the curvature of the shape. Furthermore, the corrective method of the variation in the SAR, which was caused by the inaccurate dielectric constants, was proposed.

In Chapter 5, the modeling of the abdomen of pregnant women was proposed. At first, the dielectric constants of the amniotic fluid and fetus of the rabbit were measured. As a result, the conductivity of the tissues was 1.8 or 1.3 times larger than that of the muscle of the adults at 150 MHz. The results suggested the modeling of the pregnant women including the amniotic fluid and the fetus is necessary. Next, a simple abdomen model of the pregnant women, which was composed by three types of tissues, based on measurements of MRI tomograms was introduced. Finally, an simple abdomen solid phantom of the pregnant women was presented.

In Chapter 6, the SAR inside the proposed simple abdomen model of the pregnant women, which was close to the portable radio terminals, was investigated at 150 MHz. At first, the SAR distribution in the abdomen model was calculated using the FDTD method. As a result, the SAR in the fetus by the ANT1 (0.11λ NHA) is larger than that by the ANT2 (0.18λ NHA). On the other hand, the attenuation of the SAR in the model by the ANT1 is larger than that by the ANT2 because the diffraction of the E-field in the z direction of the ANT2 is larger than that of the ANT1. Moreover, the SAR distribution around the boundary of the amniotic fluid is sharp varied by the layered structure when the antenna is attached in

front of the body. Next, the average SAR in the abdomen model was also investigated. As a consequence, the local 10 g average SAR in the fetus is less than 0.15 W/kg at the 5 W input (the maximum input of the portable radio terminals at 150 MHz in Japan), when the antenna is attached to the side of the model. On the other hand, the 10 g average SAR in the fetus is less than 1.50 W/kg at the 5 W input, when the antenna is placed in front of the model. From these results, the 10 g average SAR in the fetus is less than 2 W/kg to consider the worst case exposure. Third, the thermal error in the abdomen model and the exposure condition of the measurement was solved by the thermal analysis. As a result, it has been confirmed that the optimize exposure time is 180 s in each NHA. In addition, the maximum thermal error is almost equal to 40% at 180 s exposure. Finally, the temperature-rise distribution in the abdomen phantom was measured and compared with the calculated result of the thermal analysis. As a result, great difference between the measurement and calculation, which is caused by the gap of the body phantom, is obtained. In the measurement, the precision setting of the phantom is indispensable to evaluate the SAR inside the abdomen phantom of the pregnant women using the thermographic method.

In near future, the use of the portable communication devices will be going to grow. Therefore, the importance of the evaluation of the SAR, which is not due to the frequency, shape, devices, will be increasing.

The author will be glad if this study is of any help to the people concerning to the study of the interaction between the EM waves and the human body.

Acknowledgments

I would specifically like to thank the continuing guidance and encouragement of Professor Koichi Ito. It has a great honor and at the same time a great experience to study under his instruction.

I wish to thank Professor Hiroyuki Yoshimura for his valuable comments and reviews of many of my papers. Thanks are also due to Dr. Kazuyuki Saito for his valuable guidance and many helpful discussions. I would also like to thank Professor Masaharu Takahashi for his helpful comments.

The author is indebted to Professor Kenichiro Yashiro, Professor Hiroyuki Hachiya, Professor Toshiaki Takano, Chiba University, for their helpful discussion on my research and this dissertation.

Many thanks are expressed particularly to Dr. Soichi Watanabe, National Institute on Information and Communications Technology, and Dr. Yoshinobu Okano, Musashi Institute of Technology, for their helpful comments and discussions.

My gratitude also goes to Dr. Koichi Ogawa, Matsushita Electric Industrial Co., Ltd., Dr. Yoshio Koyanagi, Panasonic mobile communications Co., Ltd., Mr. Genji Hirokawa, Panasonic System Solutions Co. Ltd., for their useful discussions and preparation of the experimental materials.

Acknowledgments are also made to Professor Hisao Ito, Dr. Takuya Ueda, Dr. Masao Saito, Radiation Oncology, Graduate School of Medicine, Chiba University, and Dr. Hisao Osada, Chiba University Hospital, for their helpful discussion on my research and this cooperation.

I would like to give my appreciation to Mr. Teruo Onishi, Mr. David Delaune, Mr. Katsuyuki Fujii, Mr. Shoichi Kajiwara, and Mr. Toshimitsu Tanaka, who are graduate

student of Chiba University, for providing me with many valuable discussions and priceless experience during my schooling, I would like to express my sincere gratitude to Mr. Kazuya Nagasawa, Mr. Takuya Takimoto, Mr. Toshihiro Togashi, Chiba University, and other students at Ito laboratory. Thanks are direct as well to Dr. Lira Hamada, Dr. Takefumi Namiki, Dr. Ichiro Ida, Mr. Toshihiro Asahina, Mr. Yoshiki Okano, and Mr. Toshihiro Yokota, who are the excellent graduates of Chiba University, for their sincere cooperation in my research.

I would like to thank the Technical Groups of IEICE: Antennas and Propagation Group and Electro Magnetic Compatibility Group and Human Phantoms for Electromagnetics Group for helpful comments. Acknowledgments are also made to Matsushita Industrial Co., Ltd for its financial support.

I would also like to thank Professor Toru Uno, Tokyo University of Agriculture and Technology, Professor Osamu Fujiwara, Nagoya Institute of Technology, Professor Toshio Nojima, Hokkaido University, and Dr. Akimasa Hirata, Osaka University, for their helpful comments.

I wish to acknowledge all the other people who have contributed to the completion of this dissertation.

At last, I express the respects to all members of my family, who have given me encouragement and willingness to let me study.

Publication list

Journal papers

(1) H. Kawai, H. Yoshimura, and K. Ito, "Effects of inaccurate electric constants of the tissue-equivalent phantoms on the local SAR and the SAR distribution," (in Japanese), *Trans. IEICE*, vol. J85-B, no. 5, pp. 619–630, May 2002.

(2) H. Kawai and K. Ito, " Simple evaluation method of estimating local average SAR," *IEEE Trans. Microwave Theory Tech.*, vol. J86-B, no. 8, pp. 2021–2029, Aug. 2004.

Other papers

(1) Y. Okano, K. Ito, and H. Kawai, "Solid phantom composed of glycerin and its application to SAR estimation," (in Japanese), *Trans. IEICE*, vol. J83-B, no. 4, pp. 534–543, Apr. 2000.

(2) K. Ito, H. Kawai, and K. Saito, "State of the art and future prospects of biological tissue-equivalent phantoms," (in Japanese), *Trans. IEICE*, vol. J85-B, no. 5, pp. 582–596, May 2002.

(3) Y. Koyanagi, H. Kawai, K. Ogawa, and K. Ito, "Consideration of the local SAR and radiation characteristics of a helical antenna using a cylindroid whole body phantom at 150MHz," (in Japanese), *Trans. IEICE*, vol. J85-B, no. 5, pp.664–675, May 2002.

(4) Y. Koyanagi, H. Kawai, K. Ogawa, and K. Ito, "Estimation of the local SAR in the human abdomen using a human body phantom and small antennas at 150 MHz," (in Japanese), *Trans. IEICE*, vol. J86-B, no. 7, pp. 1207–1218, July 2003.

International conference

(1) H. Kawai, H. Yoshimura, and K. Ito, "A precise measurement method for the local peak SAR estimation by using the solid phantoms," in *Proc. Int. Antennas Propagation Symp.*, vol. 3,Fukuoka, Japan, Aug. 2000, pp. 1063–1066.

(2) H. Kawai, Y. Okano, H. Yoshimura, and K. Ito, "A precise measurement of the SAR distribution in the human head model using the thermographic method," in *Proc. Asia-Pacific Broadcasting and Communications Symp.*, VL-05, Bangkok, Thailand, Dec. 2000, pp. 43–46.

(3) H. Kawai, H. Yoshimura, and K. Ito, "Estimation of an error caused by inaccurate electric constants of the biological tissue-equivalent phantom," in *Proc. Int. IEEE Antennas and Propagation Society Symp.*, vol. 2, Boston, USA, July 2001, pp. 52–55.

(4) Yoshio KOYANAGI, Hiroki KAWAI, Koichi OGAWA, Hiroyuki YOSHIMURA, and Koichi ITO, "Estimation of the radiation and SAR characteristics of the NHA at 150 MHz by use of the cylindroid whole body phantom," in *Proc. Int. IEEE Antennas and Propagation Society Symp.*,vol. 3, Boston, USA, July 2001, pp. 78–81.

(5) K. Ito, H. Kawai, H. Yoshimura, Y. Koyanagi, and K. Ogawa, "Phantoms for estimation of the interaction between EM waves and a human body," in *Proc. Asia-Pacific Radio Science Conference*, K6-2-01, Tokyo, Japan, Aug. 2001, p. 270.

(6) H. Kawai, H. Yoshimura, and K. Ito, "Effect of inaccurate electric constants of the biological tissue-equivalent phantom on the local average SAR," in *Proc. Korea-Japan AP/EMC/EMT Joint Conference*, Taejon, Korea, Sept. 2001, pp. 103–106.

(7) H. Kawai, H. Yoshimura, and K. Ito, "Effects of inaccurate electric constants of the tissue-equivalent phantoms on the local averaged SAR at 900 MHz and 2.0 GHz," in *Proc. Int. USNC/URSI Radio Science Meeting*, San Antonio, USA, June 2002, p. 51.

(8) Yoshio KOYANAGI, Hiroki Kawai, Koichi OGAWA, and Koichi ITO, "Internal distribution of the local SAR in the human abdomen measured by a split phantom and small helical antennas at 150 MHz," in *Proc. Int. IEEE Antennas and Propagation Symp.*, vol. 3, Columbus, USA, June 2003, pp. 1079–1082.

(9) H. Kawai, Y. Koyanagi, K. Ogawa, K. Saito, and K. Ito, "A study on the evaluation of the electromagnetic exposure in the human fetus model at 150 MHz," in *Proc. Int. IEEE Antennas and Propagation Symp.*, vol. 3, Columbus, USA, June 2003, pp. 1087–1090.

(10) K. Ito and H. Kawai, "Phantoms for evaluation of interactions between antennas and human body," in *Proc. Int. URSI EMT-S Electromagnetic Theory Symp.*, vol. 2, Pisa, Italy, May 2004, pp. 1104-1106.

Technical Reports

(1) H. KAWAI, Y. Okano, H. Yoshimura, and K. Ito, "Solid phantom composed of glycerin and its application to SAR estimation by using the thermographic method," (in Japanese), in *Proc. IEICE Tech. Rep. A·P2000–8*, Yokohama, Japan, Apr. 2000, pp. 49–54.

(2) O. Kagaya, S. Watanabe, K. Wake, H. KAWAI, T. Uno, M. Takahashi, Y. Yamanaka, and K. Ito, "The dependence of the accuracy of the SAR estimation based on temperature measurement on the material and based on temperature measurement on the material and shape of phantoms," (in Japanese), in *Proc. IEICE Tech. Rep. EMCJ2000–111*, Nagoya, Japan, Dec. 2000, pp. 61–66.

(3) Y. Okano, H. KAWAI, K. Koyanagi, H. Yoshimura, and K. Ito, "A Study on the reduction of the local SAR by use of the folded dipole antenna with a planar reflector," (in Japanese), in *Proc. IEICE Tech. Rep. A·P2001–159*, Tokyo, Japan, Dec. 2001, pp. 23–30.

(4) H. KAWAI, T. Yokota, Y. Koyanagi, K. Ogawa, K. Saito, and K. Ito, "A study on the human abdomen phantom for SAR estimation based on the electric constants of internal organs of a rabbit," (in Japanese), in *Proc. IEICE Tech. Rep. EMCJ2003–3*, Tokyo, Japan, Apr. 2003, pp. 17–22.

(5) T. Yokota, H. KAWAI, K. Ito, K. Saito, H. Yoshimura, T. Ueda, M. Saito, H. Ito, Y. Koyanagi, and K. Ogawa, "Evaluation of the SAR using a simple abdomen model based on pregnant women data," (in Japanese), in *Proc. IEICE Tech. Rep. EMCJ2003–126*, Tokyo, Japan, Jan. 2004, pp. 13–28.

(6) H. KAWAI, K. Ito, K. Saito, H. Yoshimura, T. Ueda, M. Saito, H. Ito, Y. Koyanagi, and K. Ogawa, "Thermal analysis inside a simple abdomen model based on pregnant women data," (in Japanese), in *Proc. IEEJ Tech. Rep. EMC–04–37*, Tokyo, Japan, Apr. 2004, pp. 29–34.

(7) K. Nagasawa, H. KAWAI, K. Ito, K. Saito, H. Yoshimura, T. Ueda, M. Saito, H. Ito, Y. Koyanagi, and K. Ogawa, "Evaluation of the SAR by the thermographic method for a simple abdomen solid phantom of pregnant women," (in Japanese), in *Proc. IEICE Tech. Rep. A·P2004–134*, Tokyo, Japan, Oct. 2004, pp. 7–12.

References

[1] C. Hill and T. Kneisel, "Portable radio antenna performance in the 150, 450, 800, and 900 MHz bands "outside" and in-vehicle," *IEEE Trans. Veh. Tech.*, vol. 40, no. 4, pp. 750–756, Nov. 1991.

[2] M. A. Jensen and Y. Rahmat-Samii, "EM interaction of handset antennas and a human in personal communications," *Proc. IEEE*, vol. 83, no. 1, pp. 7-17, Jan. 1995.

[3] S. Watanabe, M. Taki, and T. Nojima, "Effects of the interaction between a human head and a hand-held portable radio on the antenna input impedance," (in Japanese), *Trans. IEICE*, vol. J79-B-II, no. 9, pp. 557–565, Sep. 1996.

[4] K. Ogawa, H. Iwai, J. Hatakenaka, "A high-precision real human phantom for EM evaluation of handheld terminal antennas in a talk situation," (in Japanese), *Trans. IEICE*, vol. J85-B, no. 5, pp. 676-686, May 2002.

[5] M. Saito and M. Taki, "Biological effects of electromagnetic fields and health risks," (in Japanese), *J. IEICE*, vol. 82, no. 6, pp. 572–579, June 1999.

[6] ICNIRP, "Guidelines for limiting exposure to time-varying electric, magnetic, and electromagnetic fields (up to 300 GHz)," *Health Phys.*, vol. 74, no. 4, pp. 494–522, Apr. 1998.

[7] EU, "Council Recommendation on the limitation of exposure of the general public to electromagnetic fields (0Hz to 300GHz)," Official Journal of the European Communities, 1999/519/EC, Jul. 1999.

[8] "Guidelines for evaluating the environmental effects of radiofrequency radiation," FCC, Wahington, DC, FCC ET Docket 93–62, 1997.

[9] IEEE standard for safety levels with respect to human exposure to radio frequency electromagnetic fields, 3 kHz to 300 GHz, ANSI/IEEE Standard C95.1-1991, Apr. 1992.

[10] IEEE Standards Coordinating Committee 34 on Product Performance Standards Relative to the Safe Use of Electromagnetic Energy, "Draft Recommended Practice for Determining the Spatial-Peak Specific Absorption Rate (SAR) in the Human Body Due to Wireless Communications Devices: Experimental Techniques," P1528, 200X.

[11] "Radio-radiation protection guidelines for human exposure to electromagnetic fields," (in Japanese), Telecommun. Technol. Concil Ministry Posts Telecommun., Deliberation Rep. 89, Tokyo, Japan, 1997.

[12] *Specific absorption rate (SAR) estimation for cellular phone*, ARIB Standard T-56, ver. 1.0, Jan. 2002.

[13] International Electrotechnical Commission, "Procedure for determine the SAR for hand held mobile phones in the frequency range of 300MHz to 3GHz," TC106, IEC/106/49/CD.

[14] O. P. Gandhi, G. Lazzi, and C. M. Furse, "Electromagnetic absorption in the human head and neck for mobile telephones at 835 and 1900 MHz," *IEEE Trans. Microwave Theory Tech.*, vol. 44, no. 10, pp. 1884–1897, Oct. 1996.

[15] S. S. Stuchly, M. A. Stuchly, A. Kraszewski, and G. Hartsgrove, "Energy deposition in model of man: frequency effects," *IEEE Trans. Biomed. Eng.*, vol. 33, no. 7, pp.702–711, Jul. 1986.

[16] M. A. Stuchly, A. Kraszewski, and S. S. Stuchly "Exposure of human models in the near and far field - a comparison," *IEEE Trans. Biomed. Eng.*, vol. 32, no. 8, pp.609–616, Aug. 1985.

[17] M. A. Stuchly, A. Kraszewski, S. S. Stuchly, G. W. Hartsgrove, and R. J. Spiegel, "RF Energy deposition in heterogeneous model of man: near-field exposures," *IEEE Trans. Biomed. Eng.*, vol. 34, no. 12, pp.944–950, Dec. 1987.

[18] V. Hombach, K. Meier, M. Burkhardt, E. Kühn, and N. Kuster, "The dependence of EM energy absorption upon human head modeling at 900MHz," *IEEE Trans. Micowave Theory Tech.*, vol. 44,no. 10, pp. 1865–1873, Oct. 1996.

[19] K. Meier, V. Hombach, R. Kastle, R. Y-S Tay, N. Kuster, "The dependence of electromagnetic energy absorption upon human head modeling at 1800 MHz," *IEEE Trans. Micowave Theory Tech.*, vol. 45,no. 11, pp. 2058–2062, Nov. 1997.

[20] F. Schoenborn, M. Burkhardt, and N. Kuster, "Difference in energy absorption between heads of adults and children in the near field of sorces," *Health Phys.*, vol. 74, no. 2, pp. 160–168, Feb. 1998.

[21] O. Fujiwara, J. Wang, T. Hisada, S. Watanabe, Y. Yamanaka, "Comparison of local SAR in realistic head models of adults and children for portable telephones," (in Japanese), *Trans. IEICE*, vol. J86-B, no. 7, pp. 1219–1224, July 2003.

[22] A. W. Guy, C. -K. Chou, and B. Neuhaus, "Average SAR and SAR distributions in man exposed to 450-MHz radiofrequency radiation," *IEEE Trans. Micowave Theory Tech.*, vol. 32, no. 8, pp. 752–762, Aug. 1984.

[23] T. Nagaoka, K. Sakurai, E. Kunieda, S. Watanabe, H. Honma, T. Suzuki, M. Kawai, K. Sakamoto, K. Ogawa, K. Konokawa, K. Kubota, B. Kim, M. Taki, Y. Yamanaka, and S. Watanabe, "The development of whole-body high-resolution voxel models of the average Japanese adult male and female," (in Japanese), *Bio. Med. Eng.*, vol. 40, no. 4, pp. 45–52, Dec. 2002.

[24] A. Drossos, V. Santomaa, and N. Kuster, "The dependence of electromagnetic energy absorption upon human head tissue composition in the frequency range of 300-3000 MHz," *IEEE Trans. Microwave Theory Tech.*, vol. 48, no. 11, pp. 1988–1995, Nov. 2000.

[25] N. Kuster and Q. Balzano, "Energy absorption mechanism by biological bodies in the near field of dipole antenna above 300 MHz," *IEEE Trans. Microwave Veh. Technol.*, vol. 41, no. 1, pp. 17–23, Feb. 1992.

[26] A. W. Guy, "Analysis of electromagnetic fields induced in biological tissues by the thermographic studies on equivalent phantom models," *IEEE Trans. Microwave Theory Tech.*, vol. 19, no. 2, pp. 205–214, Feb. 1971.

[27] Q. Balzano, O. Garay, and F. Steel, "Energy deposition in simulated human operators of 800 MHz portable transmitters," *IEEE Trans. Veh. Tech.*, vol. 27, no. 5, pp. 174–181, May 1978.

[28] Y. Okano, K. Ito, I. Ida, and M. Takahashi, "The SAR evaluation method by a combination of thermographic experiments and biological tissue-equivalent phantoms," *IEEE Trans. Microwave Theory Tech.*, vol. 48, no. 11, pp. 2094–2103, Nov. 2000.

[29] H. Kawai, H. Yoshimura, and K. Ito, "A precise measurement method for the local peak SAR estimation by using the solid phantoms," in *Proc. Int. Antennas Propagation Symp.*, vol. 3, Fukuoka, Japan, Aug. 2000, pp. 1063–1066.

[30] S. Amari, Y. Okano, and M. Abe, "Study on the SAR estimation by optical fiver thermometer," (in Japanese), in *Proc. IEICE Tech. Rep. EMCJ2002-98*, Tokyo, Japan, Jan. 2003, pp. 9–16.

[31] R. Y.–S. Tay, Q. Balzano, and N. Kuster, "Dipole configurations with strongly improved radiation efficiency for hand-held transceivers," *IEEE Trans. Antennas Propagat.*., vol. 46, no. 6, pp. 796–806, June 1998.

[32] T. Kobayashi, T. Nojima, K. Yamada, and S. Uebayashi, "Dry phantom composed of ceramics and its application to SAR estimation," *IEEE Trans. Microwave Theory Tech.*, vol. 41, no. 1, pp. 136-140, Jan. 1993.

[33] K. Ito, K. Furuya, Y. Okano, and L. Hamada, 'Development and the characteristics of a biological tissue-equivalent phantom for microwaves," (in Japanese), *Trans. IEICE*, vol. J81-B-II, no. 12, pp. 1126–1135, Dec. 1998.

[34] Y. Okano, K. Ito, and H. Kawai, "Solid phantom composed of glycerin and its application to SAR estimation," (in Japanese), *Trans. IEICE*, vol. J83-B, no. 4, pp. 534–543, Apr. 2000.

[35] Y. Koyanagi, H. Kawai, K. Ogawa, and K. Ito, "Consideration of the local SAR and radiation characteristics of a helical antenna using a cylindroid whole body phantom at 150MHz," (in Japanese), *Trans. IEICE*, vol. J85-B, no. 5, pp.664–675, May 2002.

[36] Y. Koyanagi, H. Kawai, K. Ogawa, and K. Ito, "Estimation of the local SAR in the human abdomen using a human body phantom and small antennas at 150 MHz," (in Japanese), *Trans. IEICE*, vol. J86-B, no. 7, pp. 1207–1218, July 2003.

[37] O. Kagaya, S. Watanabe, K. Wake, H. KAWAI, T. Uno, M. Takahashi, Y. Yamanaka, and K. Ito, "The dependence of the accuracy of the SAR estimation based on temperature measurement on the material and based on temperature measurement on the material and shape of phantoms," (in Japanese), in *Proc. IEICE Tech. Rep. EMCJ2000–111*, Nagoya, Japan, Dec. 2000, pp. 61–66.

[38] COST244 Working Group 3, "Proposal numerical canonical models in mobile communications," in *Proc. COST 244.*, Rome, Italy, Nov. 1994, pp. 1–7.

[39] K. Ito, H. Kawai, and K. Saito, "State of the art and future prospects of biological tissue-equivalent phantoms," (in Japanese), *Trans. IEICE*, vol. J85-B, no. 5, pp. 582–596, May 2002.

[40] T. Iyama, Y. Tarusawa, S. Uebayashi, T. Nojima, and O. Fujiwara, "Local SAR estimation system using solid phantom and fixed E-field probe," (in Japanese), *Trans. IEICE*, vol. J85-B, no. 5, pp. 631–639, May 2002.

[41] T. Schmid, O. Egger, and N. Kuster, "Automated E-field scanning system for dosimetric assessments," *IEEE Trans. Micowave Theory Tech.*, vol. 44, no. 1, pp. 105–113, Jan. 1996.

[42] T. C. Cetas, "Practical thermometry with a thermographic camera-calibration, transmittance, and emittance measurement," *Rev. Sci. Instrum.*, vol. 49, no. 2, Feb. 1978.

[43] K. S. Yee, "Numerical solution of initial boundary value problems involving Maxwell's equation in isotropic media," *IEEE Trans. Antennas Propagat.*., vol. 14, no. 3, pp. 302–207, Mar. 1966.

[44] T. Uno, Finite difference time domain method for electromagnetic field and antenna analysis, (in Japanese), Tokyo: Corona, 1998.

[45] Schmid & Partner Engineering AG web site, http://www.speag.com/.

[46] P. A. Mason, W. D. Hurt, T. J. Walters, J. A. D'Andrea, P. Gajšek, K. L. Ryan, D. A. Nelson, K. I. Smith, and J. M. Ziriax, "Effects of frequency, permittivity, and voxel size on predicted specific absorption rate values in biological tissue during electromagnetic-field exposure," *IEEE Trans. Microwave Theo. Tech.*, vol. 48, no. 11, pp. 2050-2057, Nov. 2000.

[47] J. Svigelj and N. Buris, "SAR simulations for compliance and trend analysis," in *Proc. Int. IEEE Antennas and Propagation Symp.*, vol. 2, July 2001, pp. 56–59.

[48] R. F. Harrington, Time-harmonic electromagnetic fields, ch. 2, pp. 37-94, McGraw-Hill, New York, 1961.

[49] J. A. Stratton, Electromagnetic theory, ch. 5, pp. 268-278, McGraw-Hill, New York, 1941.

[50] A. H. J. Fleming and K. H. Joyner, "Estimates of absorption of radiofrequency radiation by the embryo and fetus during pregnancy," *Health phys.*, vol. 63, no. 2, pp. 149–159, Aug. 1992.

[51] W. Kainz, D. D. Chan, J. P. Casamento, and H. I. Bassen, "Calculation of induced current densities and specific absorption rates for pregnant women exposed to hand-held metal detectors," *Phys. Med. Biol.*, vol. 48, pp. 2551–2560, Aug. 2003.

[52] C. Gabriel, "Compilation of the dielectric properties of body tissues at RF and microwave frequencies," Brooks Air Force Technical Report, AL/OE-TR-1996-0037, 1996.

[53] A. Peyman, A. A. Rezazadeh, and C. Gabriel, "Changes in the dielectric properties of rat tissue as a function of age at microwave frequencies," *Phys. Med. Biol.*, vol. 46, pp. 1617–1629, June 2001.

[54] C. K. Chou, G. W. Chen, A. W. Guy, and K. H. Luk, "Formulas for preparing phantom muscle tissue at various radiofrequencies," *Bioelectromag.*, vol. 5, no.4, pp. 435-441, 1984.

[55] J. D. Kraus, Antennas, McGraw-Hill Book Company, 1988.

[56] K. Fujimoto and J. R. James, Mobile Antenna Systems Handbook, ed. R. Mumford, Q. Balzano, T. Taga, pp. 258–264, Artech House, 1994.

[57] K. Fujimoto, A. Henderson, K. Hirasawa, and J. R. James, Small Antennas, pp. 59–70, England, Research Studies Press Ltd., distributed by John Wiley & Sons, 1993.

[58] H.H. Pennes, "Analysis of tissue and arterial blood temperatures in the resting human forearm," *J. AppL. Phys.*, vol. 1, pp. 93–122, 1948.

[59] J. A. Scott, "A finite element model of heat transport in the human eys," *Phy. Med. Biol.*, vol. 33, pp. 227–241, 1988.

[60] P. Bernardi, M. Cvagnaro, S. Pisa, and E. Piuzzi, "SAR distribution and temperature increase in an anatomical model of the human eye exposed to the field radiated by the user antenna in a wireless LAN," *IEEE Trans. Microwave Theory Tech.*, vol. 46, pp. 2074–2082, 1998.

[61] A. Taflove and M. E. Brodwin, "Computation of the electromagnetic fields and induced temperatures within a model of the mivrowave-irradiated human eys," *IEEE Trans. Microwave Theory Tech.*, vol. 23, pp. 888–896, 1975.

[62] J. Wang and O. Fujiwara, "FDTD computation of temperature rise in the human head for portable telephones," *IEEE Trans. Microwave Theory Tech.*, vol. 47, no.8, pp. 1528–1534, Aug. 1999.

Appendix 1 : How to make solid phantoms

Our laboratory has been proposed several types of solid phantoms. From now on, the making method of the solid phantom, which is realized high-water content tissue, is presented.

[Necessary tools]

Necessity tools of the making phantom are as follows;

· Precise scale

· Gas stove (Stoves with an amount of high temperature is better . The one used in this laboratory is of 4100kcal/h.)

· Pot (About 8-10 liters)

· Mold

· Spatula

· Sieve

· Mixer/ Beater

· Knife

· Plastic film

[Fabrication procedure]

Table A-1 discribes the ingredients of the brain-equivalent phantom at 300–2500 MHz. Making method of this phantom are as follows.

1. Measure the mass of each ingredient accurately.

2. Put sodium chloride, preservatives and agar in the pot filled with deionized water. Then, dissolve them thoroughly Mix.

3. Heat the compound liquid on the cooking stove strongly. Continuously stir the liquid while rubbing the bottom of the pot with spatula evenly and lightly, so that the liquid should not scorch.

4. Stop the fire immediately when the substance starts boiling (bubble boils up all over and the liquid side comes to rise). Nevertheless, note that is the agar is not sufficiently heated, it does not coagulate. A minimum 15 minutes of heat is necessary.

5. While stirring, mix in the TX-151 with the substance. To avoid lumps, sieve the TX-151 and add it little by little. Pay attention to this stage as TX-151 lumps easily. About 10 minutes later, the substance should have become viscous.

6. Now sieve ands add little by little the polyethylene powder. It is easer to mix when the stir machine is moved along the edge of the pot. At this time, take care not to make bubbles. Stir about 15 minutes but do not beat.

7. After having uniformly mixed all of the material, pours the substance slowly into a mould so that the air does not to enter. Note that the air does not enter easily when the mould is slightly inclined and substance slowly poured.

8. A plastic film has to be put after finishing pouring so that the phantom does not stick to the mould. Moreover, this prevents the foreign body from invading the phantom.

9. Leave at room temperature for one night. Meanwhile, put once the knife between the sides of the phantom and mould 3 to 5 hours later after pouring if is possible. This prevents from cracking the phantom during cooling.

10. After the phantom has coagulated, turn it out.

11. Round down the edges of the phantom and trim its shape. Cut off the top and bottom of the phantom for several cm, because the surface is usually not smooth.

12. To prevent dryness, wrap the phantom with a plastic film. It can be kept for a quite long time if at room temperature.

Table A-1 Ingredients of the brain-equivalent phantom at 300–2500 MHz.

Material	Mass [g]	Weight ratio [%]
Deionized water	3,375	82.12
Sodium chloride	23.1	0.56
Polyethylene Powder	548.1	13.33
TX-151	57.1	1.39
DASS	2.0	0.05
Agar	104.6	2.55

DASS: Dehydroacetic acid sodium salt

The volume of a completed phantom is approximately 4,000 cm^3.

Vita

Hiroki Kawai

He was born in Kimitsu-shi, Chiba, Japan, on March 31, 1977. He received the B.E. and M.E. degrees from Chiba University, Chiba, Japan, in 1999 and 2001, respectively, both in electrical engineering. Also he is expected to receive the D.E. degree from Chiba University. His main interests include analysis and design of small antennas for mobile communications, research on evaluation of the interaction between electromagnetic fields and the human body by use of numerical and experimental phantoms. He is currently working toward the D.E. degree at Chiba University. Mr. Kawai is a Member of the IEEE, the IEICE of Japan.